HEALTH MONITORING OF MACHINERY FLUIDS USING EXCITATION-EMISSION MATRIX SPECTROSCOPY AND CAVITY RING-DOWN SPECTROSCOPY

By

Hengameh Omrani

A thesis submitted to the Department of Chemistry

In conformity with the requirements for

the degree of Doctor of Philosophy

Queen's University

Kingston, Ontario, Canada

(April, 2014)

Abstract

The quality of machinery liquids plays a critical role in ensuring safe and cost-effective operation of engines. Especially in the aviation industry, there is a great need for real-time and online monitoring of the purity, lubricity and age of machinery fluids.

In this work, two optical techniques, excitation-emission matrix spectroscopy (EEMS) and cavity ring-down spectroscopy (CRDS), are used for monitoring of degradation and contamination of aero-turbine lubricants and jet fuels using optical fiber probes.

We implement EEMS combined with a modified fiber probe design to characterize lubricant quality through the characteristic fluorescence of antioxidant additives. Multi-way analysis procedures, such as parallel factor analysis, are applied to correlate spectral features to antioxidant concentration, oxidative stability, and lubricant age. The spectroscopic data are then correlated to commonly used, off-line parameters such as the induction time and the breakdown number.

It is shown that the decrease in fluorescence intensities of antioxidants coincides with the decomposition of the oil base stock. The induction times of synthetic jet turbine oil degraded at 150°C, 195°C and 215°C are found to be at about 10,000, 3,500 and 400 min respectively. Simple kinetic models are developed that are capable of describing antioxidant reactions as pseudo first-order processes.

We also demonstrate that with fluorescence detection it is possible to determine the concentration of oil contamination in jet fuel from about 10 to 1000 $ppm_{v.}$

In addition, a fiber-loop cavity ring-down spectrometer has been developed to quantitatively identify oil contamination of jet fuel by measuring optical absorption in the

UV region. CRDS is a very sensitive, path-enhanced absorption technique that may be used for trace-species measurements in gas and liquids. The absorption measurements on samples with small volumes are characterized by measuring the concentration of turbine oil in jet fuel from 100 000 ppm_v to a limit of detection of 400 ppm_v.

In summary, the obtained results permit us to specify the life time of lubrication oil and to determine the contamination of jet fuel with turbine oil qualitatively and quantitatively. In a simple optical configuration the fiber-coupled EEM and CRD methods permit *in situ* sampling of the machinery fluids.

Acknowledgement

I would like to express my special appreciation and thanks to my supervisors Professor Dr. Hans-Peter Loock and Dr. Alexander Dudelzak, who have been tremendous mentors for me. I would like to thank them for giving me the opportunity to do this research, for their support, for encouraging and allowing me to grow as a research scientist. Their advice and help on both research as well as on my career have been priceless. I would never have been able to finish my thesis without the guidance of my supervisors.

I am honored to have had Professors Dr. Diane Beauchemin and Dr. Stephen Brown as members of my dissertation committee. I would also like to acknowledge them for their meaningful comments and guidelines during my Supervisory Committee meetings.

Definitely, I would like to express my deep appreciation to various people at GasTOPS Ltd., especially Dr. Bernard MacIsaac and Mr. David Muir for giving me the opportunity to work on and finish my graduate work while employed at GasTOPS and to support me by all means.

Furthermore, I want to thank all my past and present colleagues and friends in the research groups of Dr. Hans-Peter Loock who created such a good atmosphere in the lab. and specifically, Dr. Jack A. Barnes who has helped me with building some of the experimental set up. I want to express my gratitude to Dr. Helen Wächter, and Dr. Klaus J. Bescherer-Nachtmann, John Saunders, Nicholas Andrews, Stephen Walker, Jeff Crouse, and Sogol Borjian for their friendship, support and their brilliant comments and suggestions during our scientific conversations.

Moreover, I want to express my deep gratitude to Allison M. Toms, Darrell Churchill, Dr. Bruce Hollebone, Dr. Peter Wentzell, Dr. Igor Kozin and Tom Hunter for their support with countless conversations and their insights regarding different aspects of my thesis project.

I would also like to thank the people in the general office, the people in science stores, and IT Technicians for their generous help during my studies and research process.

I would like to extend my gratitude to my uncle, Dr. Nasser Moeen Vaziri and his wife, my cousin, Sholeh Emrani for their professional and personal advice and encouragement.

Especially, I would like to thank my parents for allowing me to realize my own potential. All the support and unconditional love they have provided me over the years were the greatest gifts anyone has ever given me.

Finally, special thanks to the newest addition to my family, my husband Alireza, who loves me unconditionally and has been very supportive, patient and caring.

Statement of Originality

I hereby certify that all of the work described within this thesis is the original work of the author unless otherwise stated.

The modeling of fiber-optic fluorescence probes for strongly absorbing samples (chapter 4) was conducted with a major contribution of Dr. Hans-Peter Loock.

Any published (or unpublished) ideas and/or techniques from the work of others are fully acknowledged in accordance with the standard referencing practices.

Hengameh Omrani

April, 2014

Table of Contents

List of Figures

List of Tables

List of Schematics

List of Abbreviations

ADPA ……Alkylated Diphenylamine

AES ……...Atomic Emission Spectroscopy

AN …… Acid Number

AO …….Antioxidant

APAN ……Alkylphenyl-α-naphthylamine

API …… American Petroleum Institute

ASTM…… American Society for Testing and Materials

BDN ……. Breakdown Number

BHT……... 2,6-Di-tertiarybutyl-4-methylphenol

CBM …… Condition-Based Maintenance

CCD ……... Charge-Coupled Device

CME …….Canola Methyl Ester

CRD ……. Cavity Ring-Down

DODPA……..Dioctyldiphenylamine

DOM ……... Dissolved Organic Matter

DPA...…… Diphenylamine

DRGW...…… Denver & Rio Grande Western Railroad

EEM..……. Excitation Emission Matrix

EEMS..……...Excitation Emission Matrix Spectroscopy

EP……...Extreme Pressure

FAME...……. Fatty Acid Methyl Ester

FBG..……..Fiber Bragg Grating

FLCRDS...……. Fiber-Loop Cavity Ring-Down Spectroscopy

FME..……. Fish Methyl Ester

FTIR..……Fourier Transform Infrared

GC……..Gas Chromatography

GC-FID...……... Gas Chromatography-Flame Ionization Detector

GC-MS ……..Gas Chromatography - Mass Spectrometry

HP…….. Hindered Phenolic

ICP……. Inductivity Coupled Plasma

IR……... Infrared

ISO……. International Organization for Standardization

JOAP……..Joint Oil Analysis Program

KFT..…….. Karl Fisher Titration

LED.……...Light Emitting Diode

OEM……...Original Equipment Manufacture

OPAN..……...Octylphenyl-α-naphthylamine

PAC.……...Polycyclic Aromatic Compounds

PAH..…….. Polycyclic Aromatic Hydrocarbons

PAN..……. Phenyl-α-naphthylamine

PARAFAC……. Parallel Factor Analysis

PC.……..Particle Counting

PCA……Principal Component Analysis

PCR……Principal Component Regression

PDSC.…… Pressure Differential Scanning Calorimetry

PMT……... Photomultiplier Tube

RDE..…….. Rotary Disk Electrode

RHS……Right Hand Side

RMSEC……..Root Mean Squared Error of Calibration

RMSEP…….. Root Mean Squared Error of Prediction

RULER. …… Remaining Useful Life Evaluation Rig

SAE……Society of Automotive Engineers

SEC…… Standard Error of Calibration

SEP…….Standard Error of Prediction

SME……... Soy Methyl Ester

SFS…….Synchronous Fluorescence Spectrum

SSR…… Sum of Squares of Residuals

TAN……... Total Acid Number

TME……... Beef Methyl Ester

UV……..Ultra Violet

UV/Vis……... Ultra Violet / Visible

XRF……X-ray Fluorescence

ZDDP……. Zinc dialkyldithiophosphates

1 Chapter 1. Introduction

1.1 Motivation

Machinery fluids are essential for machine operation. Hydrocarbon-based compounds that are typically used in the formulation of machinery fluids such as engine oils, industrial lubricants, aviation and diesel fuel include aromatics, paraffinic and cycloparaffinic (naphthenic) molecules. From the perspective of lubricant oil and fuel applications, their most relevant properties include viscosity, oxidative/thermal stability for lubricants and combustion requirements for fuel[1]. Engine lubricants are mainly used to reduce friction between moving parts within the interior engine, but also serve to remove debris and heat from the moving parts of an engine. From the moment oil enters an operating machine it begins to deteriorate. In addition, the oil can become contaminated with wear metal debris, oxidation by-products and external substances such as water, fuel, dirt and/or process materials[2]. A high level of oil degradation or contamination may result in a mechanical or lubricant failure, which if left unattended, could eventually lead to extensive damage or failure of the machine. To assure maximum equipment reliability, the equipment manager must determine how well machinery fluids are performing and whether contamination, degradation or excessive wear is occurring. Oil analysis can effectively identify these failure modes. Conversely, the contamination of lubricants indicates system failure and may be used to identify the cause of the problem.

Related operating problems can be caused by the contamination of fuel. On its journey from the refinery to the fuel tank, diesel and aviation fuels spend time in storage and may be transferred many times. Each time a transfer occurs, there is a potential for contamination of the fuel. As a result of contaminants in fuel, engine and fuel system parts can become damaged. The cost for repairs and / or replacement can be extensive in terms of money and time[1, 3].

Indeed, engine failure is the primary cause for lost military aircraft. Many of these engine failures could be prevented if online sensors reported the quality of the lubricant and fuel and alerted the operator of the engine about the threat of engine failure. It may appear surprising that there exists not a single commercial analytical sensor that could reliably monitor in real time the condition of the lubricants that are used in these engines. This lack of lubricant monitoring is especially disturbing considering that it is almost always the degradation of the lubricant, and thus damages to machine's components, that lead to engine failures.

In this project, we expand the range of lubricant/fuel monitoring to encompass classes of compounds that presently can only be quantified off-line. In particular, we focus on online monitoring of the most meaningful indicators of lubricant and fuel quality, i.e. on oil in fuel, on oxidation products (ageing) in oil, on water in oil, and on glycol in oil. Optical techniques, such as absorbance and luminescence spectroscopy, are suited for rapid data collection with minimal sample pre-treatment. In addition, fluorescence spectroscopy has a high sensitivity with respect to the aromatic content of complex hydrocarbon mixtures and allows for fast data acquisition. Accurate data treatment can be carried out on fluorescence spectroscopic data at relatively low cost.

Since single wavelength excitation or emission spectra alone do not contain adequate information to differentiate hydrocarbon mixtures of similar composition, we propose that the most promising measurements are based on a fully correlated combination of UV/Vis and IR absorption and UV-induced fluorescence. More specifically, it was decided that fiber based Cavity-Ring-Down (CRD) absorption spectroscopy, and fiber-coupled Excitation Emission Matrix (EEM) spectroscopy in combination can provide the information that is needed to detect and quantify contamination and degradation products in machinery fluids.

1.2 Machinery Lubricants

In all industrial machinery systems a thin layer of lubricant oil is required between sliding surfaces to prevent metal-on-metal contact. Reliable lubrication increases the maximum life time of the machine. In fact, lubrication is one of the most important factors in machine performance. Improved operation, productivity, and lower maintenance costs are obtained with a properly managed and monitored machinery lubrication program.

The lubricant used in a machine should comply with the machinery application[2]. The efficient operation of machinery relies on the type of lubricant selected. Different types of lubricants must be employed for different parts in a machine. For example, heavy oil should be used for a manual transmission system of a car while an automatic transmission should be lubricated with a special-grade light oil. Also, wheel bearings are

packed with grease, but the engine parts are lubricated with a light-weight and easy-flowing crankcase oil[4]. In addition to minimizing friction, lubricant oils serve as coolants, corrosion protectors, and help remove contaminants and debris from the engine interior.

Industrial lubricants consist of a broad range of products that, depending on their application, have different chemical and physical properties. Due to the required lubricant performance capabilities, they may be supplied from different base stock types. The American Petroleum Institute (API) categorizes base stocks into five groups[1, 2, 4]. Group I, II and III, are derived from mineral oils and have been isolated from crude oil fractions. In contrast, group IV and V lubricant base stocks are synthesized by chemical reactions to have physical properties that meet particular requirements for a specific machinery application. The base stock for synthetic lubricants includes compounds such as poly-alpha-olefins (group IV), aliphatic diesters and polyol esters (group V). Figure 1.1 shows the typical structures of a polyol ester compound.

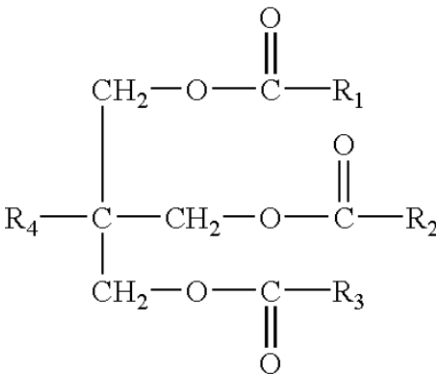

Figure 1.1 Polyol ester structure.
From reference 1

There are a few important factors that determine the required properties of lubricants for aviation application. High thermal and mechanical stability is important as the oil is subjected to high operation temperatures. Heat is the greatest challenge to the stability of aviation lubricants. In the modern gas turbine / jet engine, the lubricant temperature commonly reaches around 190°C and can, for short periods, reach temperatures of 300°C to 400°C within the bearing chambers. As a result, turbine oils must resist degradation up to these extreme temperatures and the best base oils used for this purpose are synthetic polyol esters[4,5]. Thermal stability, hydrolytic stability, low volatility and lubricity are a consequence of the presence of the ester group in these synthetic lubricants. The class of chemical compounds that contain ester functional groups are normally manufactured by an esterification reaction of alcohols with carboxylic acids upon elimination of water. For example, synthetic lubricants based on polyol esters are manufactured by the reaction of a poly-functional alcohol with mono-functional acid(s)[1].

By themselves lubricant oils, or “base stock”, rarely have all the required properties and many additives have been designed to improve their performance. Additives either enhance the properties of the base stock or by prevent changes in its composition. The base stock must be able to maintain added additives under all normal operation conditions, since it acts as the carrier for these compounds. Specialized additive packages are blended in base stocks to improve the lubricant properties such as viscosity, slipperiness, low corrosiveness, oxidation stability, and high temperature operation ability[6].

Depending on the application, there is a variety of lubricants to choose from. For all types of lubricants, viscosity is the most critical property of the lubricant, no matter the type of base stock and their blended additives or even the usage specification. Changes in viscosity affect the oil's lubricity, and any contamination and, especially, degradation of the oil that affects viscosity have a strong effect on the lubricant performance.

Lubricants age and change their composition as the machine operates due to oxidation as well as thermal and mechanical decompositions. Lubricants may then lose part of their functions, which may in turn lead to machine damage or even catastrophic failure. All commonly accepted techniques to determine lubricant oxidation require the removal of a sample of the lubricant and subsequent off-line analysis.

In this suite of projects, we attempt to develop on-line and real-time methods and protocols to monitor the contamination and degradation of aviation fuel and lubricant oils using fiber optic probes[7, 8].

1.3 Aviation Fuel

Aviation turbine fuels are used for powering jet engines. In civil commercial aviation there are currently three main grades of turbine fuel in use, *i.e.* Jet A-1, Jet A and Jet B. The first two grades are kerosene fuels and the last one is a blend of naphtha and kerosene and is known as a wide-cut fuel, but it is rarely used except in very cold climates. Jet A-1 is a kerosene grade of fuel suitable for most aircraft engines. Jet A-1 has

a flash point above 38°C (100°F) and a freezing point of -47°C. The American Society for Testing and Materials (ASTM) standard method D1655 defines the required specification for Jet A-1 as well as those of other aviation turbine fuels. Jet A is a similar kerosene type of fuel that is normally only available in the U.S.A. It has the same flash point as Jet A-1 but a higher freezing point (-40°C). Military turbine fuels; JP-4, JP-5 and JP-8 also are kerosene fuels, but contain specific additive packages to meet military requirements. Similar to lubricant oils, fuel needs the addition of additives to obtain special or improved qualities. Jet fuel is typically blended with antioxidants, metal deactivators, fuel system icing inhibitors and corrosion inhibitors.[1, 3, 9]

Fuel contamination is a notable factor in accidents caused by engine fuel starvation. According to a review by the Federal Aviation Administration between 1977 to 1980, fuel contamination was the leading cause for 381 out of 1230 engine power loss accidents. Moreover, from 1999 to 2004, 8.3% of total aviation accidents were caused by fuel contamination. Contamination has a direct impact on the service life and performance of engines. Besides decreasing engine life, contaminants can be corrosive and abrasive to the fuel system and engine components, and can further cause inefficiencies or failures in filters and separators by plugging them. It is not feasible to completely prevent fuel contamination during transport and storage, and unfortunately, in some situations, the result could be catastrophic[10, 11]. Particulate matter, water, biofuels, lubricants, surfactants and wax are the most common fuel contaminants. The presence of contaminants in fuel causes a change in the physical properties of fuel or may lead to starving the engine by plugging the nozzles.

Currently, there are a small number of standard test methods[12, 13, 14, 15] that are used to identify and measure contaminants in aviation fuel. In this thesis, optical techniques, such as fiber-coupled Excitation Emission Matrix Spectroscopy (EEMS) and Fiber-Loop Cavity Ring Down (FLCRDS), are applied to monitor the contamination of fuel with lubricant oil and biofuel known as Fatty Acid Methyl Esters (FAME).

1.4 Optical Techniques

Analytical spectroscopy uses the interaction of light with a sample to determine its composition and / or concentration. Referring to the nature of the interaction between the radiation energy and the material, optical techniques can be classified into emission, absorption and scattering spectroscopies.

1.4.1 Emission / Fluorescence Spectroscopy

When an ultraviolet or visible photon collides with a molecule, it can be absorbed and cause promoting of an electron. The excitation of the molecule from ground state to an excited state can be reversed in different ways. The excited molecule can relax back to the ground state either through the emission of light or by radiation-less transitions. Vibrational relaxation within an electronic state, internal conversion between states of the same multiplicity and intersystem crossing between states of different multiplicity are

cases of radiationless decay. If the excited molecule relaxes to the ground energy level by emitting a photon, the transition is called fluorescence, if the upper and lower state have the same spin, or phosphorescence if a "forbidden" change of spin occurs[16]. Figure 1.2 presents the different pathways a molecule can undergo once a photon is absorbed, in an energy level (Jablonski) diagram.

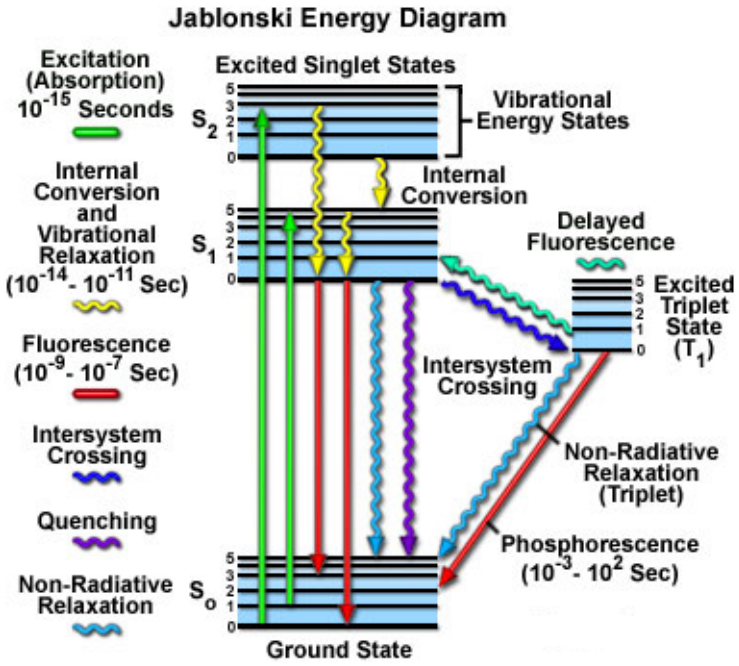

Figure 1.2 Jablonski diagram.
From. http://www.olympusmicro.com/primer/java/jablonski/jabintro/

Fluorescence spectroscopy, which provides either the emission or the excitation spectrum of the analyte, is a very sensitive technique allowing for single photon/single molecule detection in some cases. Conventionally, the fluorescence spectra can be collected at one or more excitation wavelengths and the excitation spectra can be monitored in a given fluorescence wavelength window. Single line fluorescence spectroscopy is a simple, fast and sensitive method but there are many fluorophores with

very similar emission spectra. Therefore distinguishing similar species in a sample requires the examination of all details of the fluorescence spectra[17]. To obtain such detailed information, one would have to record the fluorescence spectra at many different excitation wavelengths. In this case, for either mode at a fixed wavelength, the spectrum of the other mode would be collected. The emission intensity as a function of both excitation and emission wavelengths can then be represented by a three-dimensional response feature, which can be visualized as topographical map[18].

1.4.2 Excitation – Emission Matrix Spectroscopy

Excitation Emission Matrix Spectroscopy (EEMS) has been used as a powerful method for complex mixture analysis for the last few decades. EEMS is typically generated by scanning over the complete emission spectrum for each excitation wavelength[17,19] (x-axis=excitation wavelength, y-axis=emission wavelength, z-axis=emission intensity, Figure 1.3).

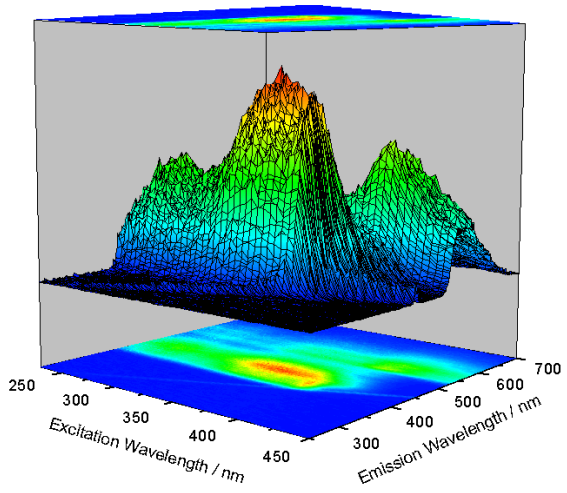

Figure 1.3 EEMS 3-D diagram.
3-D diagram and contour representation of the excitation-emission spectrum of operated jet turbine oil.

The representation of the whole three-dimensional intensity matrix realises the full potential of the fluorescence technique in its basic format. Cross sections of this three dimensional matrix at each fixed excitation and / or emission wavelengths are, respectively, the single-line emission and excitation spectra, whereas a diagonal cut at a fixed wavelength *difference* between excitation and emission wavelengths corresponds to the synchronous fluorescence spectrum (SFS). For quantitative analysis and rapid visual discrimination between fluorescence fingerprints, a contour representation of the topographic features of the excitation emission matrix is most effective. The advantage of the EEM technique is its ability to deconstruct the broad, overlapped bands characteristic of a single-line excited fluorescence spectrum into recognizable patterns, which can then be used as indicators for sample composition.

Possibly the first demonstration of fluorescence EEM was by Schachter and Haenni who developed a device in 1964, which was able to record the excitation and emission wavelengths and emission intensity simultaneously, with the excitation

wavelengths on the vertical scale and emission wavelength on the horizontal scale of a cathode ray oscilloscope graticule[18]. With this setup, a plane fluorograph was obtained with excitation and emission wavelength axes, which consists of a raster of diagonal lines. Those lines produce a characteristic pattern of contour spots - ideally one for each maximum. The dimensions of each individual spot were proportional to the width of the corresponding spectral peak and, for each spot, the coordinates of the centroid point are the related excitation and emission wavelengths of fluorescence maxima[18].

According to Rho and Stuart's literature review[17] on EEMS progress, Freegrand et al. continued the work of Schachter and Haenni and collected the fluorescence spectra at different excitation wavelengths. The contours of equal fluorescence intensity were plotted against excitation and emission wavenumbers to construct a contour map. Later in 1972, Rho and Stuart developed an experimental setup for recording all fluorescence spectra parameters on a X-Y recorder[17]. In order to identify an unknown compound by its fluorescence excitation and emission spectra, Miller and Faulkner, in 1976, created a computer file searching procedure for comparisons of the most obvious spectral features in EEM spectra such as the total number of peaks, peak locations, full width at half maxima and relative intensities. They used a mini computer interfaced to a spectrofluorometer for interpretation of the acquired spectra[20]. In an attempt to scan the fluorescence spectra and display the excitation emission contour plot at higher speed, Johnson et al. used a silicon intensified target vidicon detector to measure all wavelengths, both excitation and emission, of the polychromatic radiation of the sample cuvette simultaneously[21]. Finally, in 1978, Stuart and Rho attached an electronic circuit to a spectrofluorometer to automatically change the excitation wavelength after each scan

of the entire emission spectrum to create an EEM spectrum. They set the excitation monochromator at the lower end of the excitation wavelength range and the emission monochromator was set to scan the entire region. After the first emission scan, the excitation monochromator was adjusted to increase the excitation wavelength by increments of 1 or 2 nm. A subsequent fluorescence spectrum was scanned again and this step repeated to collect the entire EEM spectrum automatically. While the two monochromators scan over their respective wavelengths, the wavelength position potentiometers transmit the information to the X-Y recorder. They also quantized the detector output at separate levels of intensity and plotted them. Eventually all the points on the emission excitation plot were covered and all of the isointensity points appeared to join together to form a contour line[17]. The method just described became common for EEMS data collection in most of the later studies.

Excitation-emission matrix spectroscopy has been widely used in different areas of research, for example in water quality control, food industry, medical studies, characterization of alcoholic drinks, classification of oils and discrimination of fuel. Natural waters such as oceans, lakes, rivers, etc., can become contaminated with hydrocarbon pollutants from different sources. EEMS is known as a successful method for the determination of hydrocarbons and pesticides in water[22, 23]. Yuan et al. found EEMS a useful method to identify the sources of water entering rivers and oceans[24]. Characterization of Dissolved Organic Matter (DOM), one of the greatest cycled reservoirs of organic matter on earth and aquatic ecosystems, and its source identification have been investigated using EEMS[25, 26, 27]. The study of the fluorescence fingerprints of endogenous and exogenous molecules in tissues and cells has become common to

distinguish normal from diseased tissues[28]. Steetohul used EEMS to discriminate different types of tea[29]. As polyphenols and flavonoids in tea are fluorescent compounds and unique properties of tea are related to them, their collected excitation emission signature in a variety of tea samples was used as a measure of tea quality. EEMS also has been used for distinguishing between commercial samples of distilled drinks[30, 31] and for assessing wine quality and clustering wine samples from different regions[32]. 3-dimensional fluorescence spectroscopy / EEMS has been applied in medicine to identify and quantify the presence of drugs in human urine[33, 34].

The adulteration of diesel fuel and an estimate of the amount of adulterant present in diesel fuel was investigated by EEMS[35]. Excitation emission matrix measurements were also used for the determination of relative kerosene fraction (in % v/v) in diesel fuel by Divya et al.[36]. Sikorsha et al. studied the differences between EEM signatures of edible oils and the relative changes of their fluorescent characteristics in response to temperature increase and photo-oxidation[37]. The degradation of transformer oils (a derivative of petroleum crude) and the characterization of oil samples (crude oil, heavy and light fuel oil, lubricant oil) has also been monitored by collecting excitation-emission spectra. By examining EEM spectra it is even possible to match compounds in a spill to those of different sources[38, 39]. In section 2.4, the application of EEM as detection and characterization tool for petroleum products is discussed in detail. It should be noticed that all above--mentioned EEM studies were subjected to different multivariate data analysis methods to interpret the obtained EEM data precisely.

1.4.3 Multi-way Data Analysis

Analytical methods can provide data in different dimensionalities according to the capability of the instrument used. If the analytical method or instrument provides a single signal per sample, the collected datum is a single number and is identified as a zero-order tensor. Other data structures can accordingly also be classified as tensors: scalar / zero-order, vector / first-order, matrix / second-order, cube / third-order tensors, etc. (Figure 1.4).

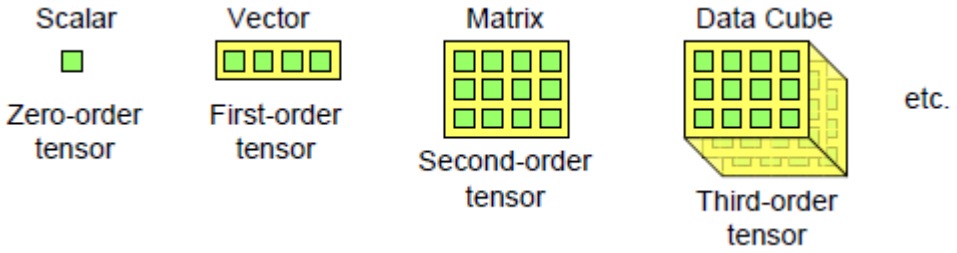

Figure 1.4 Types of data structures.
From reference 40.

The data analysis / interpretation methods also are known using the same terminology; first-order calibration means a vector of length *n* is measured for each sample. Second-order analytical methods are more powerful than zero-order and first-order, because of the so-called "second-order advantage"[40]. The term second-order advantage illustrates the capability of accurate analysis even in the presence of an existing feature (e.g. fluorescent feature due to an unaccounted fluorophore) in the data that is not included in the calibration model[41, 42]. A second-order multivariate algorithm such as parallel factor analysis (PARAFAC) can be applied for data analysis when dealing with broadband, overlapping spectra or when there are unexpected signals that have not been taken into account in the calibration step[43, 44, 45, 46]. Principal component

regression (PCR) is another multivariate calibration technique that has been applied to a wide range of spectroscopic data for the determination of individual analytes within mixtures.

1.4.3.1 Parallel Factor Analysis (PARAFAC)

Parallel Factor Analysis is a multi-way data analysis method that has been widely used to interpret the matrixes collected by EEMS. Fluorescence EEMs collected for several samples give rise to three-way data, i.e. the signal data may be arranged in a cube with axes: excitation wavelength, emission wavelength and sample number. With three-dimensional data structures, the analyte signal can be separated mathematically from the background signal. The Parallel factor analysis (PARAFAC) model can then be used to decompose the collected excitation emission matrices into the spectral profiles of individual component spectra. In some cases, each of these PARAFAC components corresponds to a chemical compound, and the method may then even be used to quantify the concentration of compounds in a mixture.

For a pure analyte, an EEM is a bilinear matrix which can be described as a scaled outer product of two column vectors: one, the excitation spectrum of the analyte at each fluorescence wavelength, and the other, the emission profile of that analyte at a single excitation wavelength[47].

The PARAFAC model, which is increasingly used for analysis of fluorescence EEMs, is a generalization of principal component analysis (PCA) to a *n*-way data set $\mathbf{X}$[48].

An appropriate data set should include spectra from either mixtures or pure compounds and also enough spectra from unknown samples that may even contain a few undesired / unknown interferences. In the present case, a three-way data cube, **X** (of dimension $I \times J \times K$) is decomposed into components. Each component consists of three loading vectors (a, b, c). When x_{ijk} (fluorescence intensity) denotes the element in position i,j,k in the data cube **X**, then the structural model of PARAFAC is expressed as follows:

$$x_{ijk} = \sum_{f=1}^{F} a_{if} b_{jf} c_{kf} + e_{ijk} \qquad (1.1)$$

Here F is a user adjustable parameter that equals to the number of components ("factors") in the model. The emission profile of a factor can be the desired fluorescence of an analyte, the fluorescence of an interference, or part of the instrumental background (i.e. due to Raman or Rayleigh scattering). In the absence of instrumental artifacts and interferences, the number of components, F, is identical to the number of fluorophores. The elements of three loading vectors a_{if}, b_{jf}, c_{kf} together with the residual error, e_{ijk}, determine the fluorescence intensity, x_{ijk},. Here, a_{if} is the concentration of fluorophore f in the i-th sample, b_{jf} is the relative absorption of fluorophore f at wavelength λ_j^{ex} and c_{kf} is the relative emission of this fluorophore, f, at wavelength λ_k^{em}. The indices stand for the sample, $i = 1, \ldots, I$, the excitation wavelengths λ_j^{ex}, $j=1, \ldots, J$ and the emission wavelengths λ_k^{em}, $k=1, \ldots, K$. Figure 1.5 represents the model for two fluorophores[44].

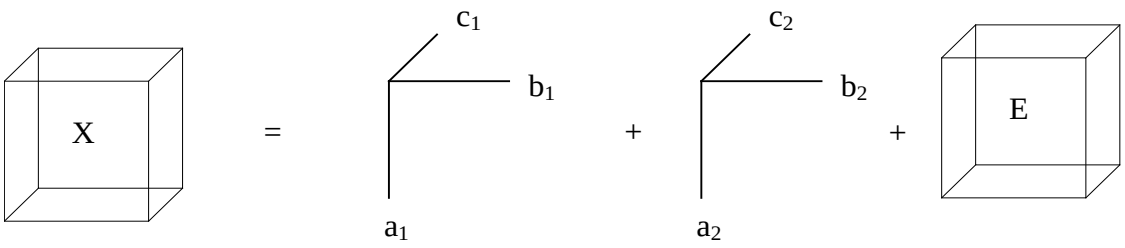

Figure 1.5 PARAFAC scheme showing data cube X, the decomposition to two components and residual E.

PARAFAC can be applied as a powerful data analysis method for deconstruction of highly overlapped spectra in EEMs collected from a mixture of similar compounds. The method also removes background noise and estimates the number of emitting components in a set of samples. Thus, PARAFAC is first applied to a set of known or standard samples to build a calibration model. In the second step PARAFAC simultaneously decomposes the standard and unknown spectra using the already determined calibration model. Therefore the EEM fluorescence signal from the unknown sample can be distinguished from any overlapping and uncalibrated interferences which will form part of the residual, **E**.

There are a few points that should be taken into consideration when using PARAFAC to interpret the multi-way data.

First, the model is only useful if the number of factors is appropriate. If the chosen number of component, *F,* is less than the actual number of distinguishable species in the sample, the error associated with the PARAFAC decomposition is large. The component's excitation and emission profiles, which are extracted from the PARAFAC model, will no longer correspond to the compound spectra and therefore any calibration based on a wrong assumption will not be accurate. Picking a value for *F* that is greater

than the number of fluorescent analytes, forces the PARAFAC model to count all systematic instrumental errors or non-fluorescence signals. As result the extracted excitation and emission profiles from the collected data are not physically meaningful and again the calibration model would not be accurate.

Second, sometimes it is possible that the mathematical component could be a non-pure chemical fluorophore, i.e. that two or more chemical compounds contribute to a common fluorescence feature. This is expected when the concentrations of these compounds are strongly correlated, because of, e.g., a common source.

Third, as was mentioned before, PARAFAC is capable of completing quantitative analysis of unknown samples which may consist of additional compounds other than those that are included in the calibration data set. This advantage is the result of simultaneous decomposition of the standard and unknown samples by the PARAFAC model. In this way PARAFAC is able to analyze the entire spectrum of unknown samples as well as a calibration set [49].

Choosing the appropriate number of factors / components is the first step for constructing a PARAFAC model. This decision can be made based on the calculation of core consistency and residual for each selected value of component numbers. PARAFAC can be considered as a special case of the Tucker3 model with an applied restriction. In Tucker3, the interactions between components and parameters and also interactions between components themselves (**G** in Equation (1.3)) are counted while in PARAFAC the last term is ignored. The three-way Tucker3 model with (P, Q, R) components is defined as:

$$x_{ijk} = \sum_{p=1}^{P}\sum_{q=1}^{Q}\sum_{r=1}^{R} a_{ip} b_{jq} c_{kr} g_{pqr} + e_{ijk} \qquad (1.2)$$

or

$$X = \left(A \otimes B \otimes C\right) \otimes G + E \qquad (1.3)$$

For the PARAFAC model the core array, *G*, would be equal to one (unity matrix), (Figure 1.6).

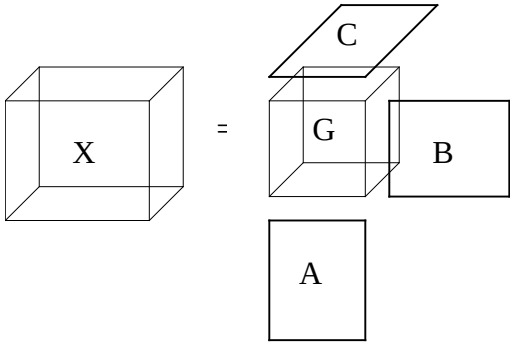

Figure 1.6 Data decomposition shematic by Tucker 3.

Therefore, the core consistency measurements will help choose a correct number of components[50]. If the calculated core consistency percentage (explained below) is close to 100, the chosen value of *F* is accurate. Another parameter, which should be considered for picking a correct number of components, is the residual. The residual is defined as the differences between the true / real value and the predicted one by the model for each variable. In other words, the residual represents missing values, so the smaller the residual (closer to zero) the more accurate is the model.

When applying the PARAFAC model to a calibration data set or the combination of the calibration and test sets, one (several) of the extracted components may reflect the

analyte (several analytes) of interest. There is a linear correlation between the calculated score of each component and the concentration of related analyte in each sample. Therefore, the analyte concentration in the test samples can be determined based on a calibration model. The following is the procedure of a general second-order calibration to construct a PARAFAC model:

- The correct number of components is estimated by calculating core consistency and residual to build the calibration PARAFAC model.
- From the extracted excitation and emission profiles the component of interest is identified.
- The scores of the identified component are scaled using sample concentrations of calibration set. The scaling factor determined from calibration data set can be applied directly to the test and prediction data set to provide estimates of the related concentrations.

As mentioned above, some compounds may be present in unknown samples and be detected and resolved by PARAFAC, whilst not being included in the calibration set. Consequently, additional PARAFAC components are required to resolve unknown interferences. While dealing with such a situation, one approach is to combine both the calibration and prediction data set and fit a new PARAFAC model. The new model contains as many components as required based on the new calculation on core consistency and residuals. It should be considered that the accuracy of the model also depends strongly on the size of the data set; the more information is provided, the more reliable is the fit. It is particularly important that many spectra contain contributions from all PARAFAC components, since any lack of a component will produce a “missing

value" flag. The refitting function may therefore by less accurate and the standard error associated with the fit may then be large.

In an ideal case the decomposition of a complicated EEM spectra using PARAFAC estimates the excitation and emission spectra and concentrations of many chemical analytes. Thus, the PARAFAC model can be considered as a mathematical "separation" method applied to EEM data and to identify specific analytes and to provide quantitative analysis, such as regression and classification.

1.4.3.2 Principal Component Analysis and Regression (PCA/PCR)

There are other multivariate calibration methods, which can be used for analysis of excitation-emission matrices instead of the PARAFAC model. Principal component regression (PCR) is one of the most common multivariate calibration techniques employed in chemistry due to its capacity to deal with highly co-linear data by reducing the dimensionality of the original data set[41, 42, 46]. Principal component analysis (PCA) is a technique that transforms the data space to a lower dimension than the original data space while retaining the maximum amount of variance in the new space. PCA is a precise technique in chemometrics for dimensionality reduction of a data set. It is especially useful in the analysis of data that is of second or higher order. PCA is also able to determine the rank (minimum number of dimensions into which the data set can be organized with the smallest residual) of the data set and thereby helps develop

multidimensional linear models. Figure 1.7 describes the application of PCA to two-way, i.e. bivariate, data.

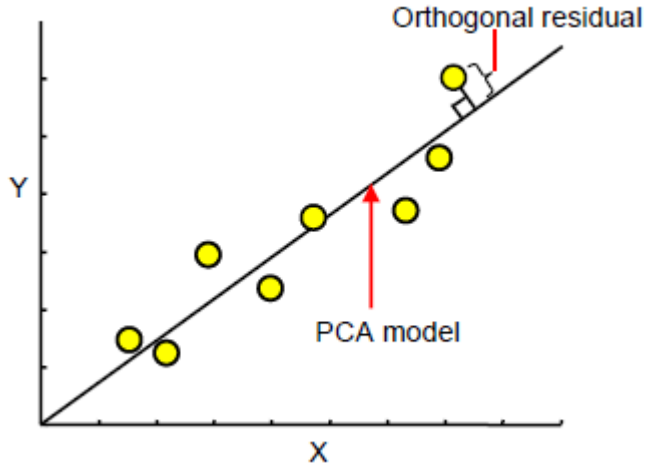

Figure 1.7 A geometric view of orthogonal projection in two dimensions.
From reference 40.

In this Figure the data points (x, y) are plotted in two-dimensional space. PCA may be used to construct a straight-line model through the points. This sounds like traditional regression but there are some differences between these two methods. The conventional "least-squares" regression method is built based on minimizing the sum of squared residuals in the vertical direction, *y*, while PCA considers minimizing the sum of squared residuals in the direction orthogonal to the fit line (Figure 1.7). The direction of the greatest variance in the data is considered by the PCA model. This means that if the sum of squares accounted by the model is subtracted from the total sum of squares, the residual sum of squares would be minimized.

In PCA, a projection of the experimental data points is obtained using a unit vector in the direction of the highest variance. The vector, $\mathbf{v}_1$, is called the first eigenvector, and is also known as the first principal component or the first loading vector.

The new value of experimental data in PCA is the projected point along this vector and is called the score for that point, (Figure 1.8),

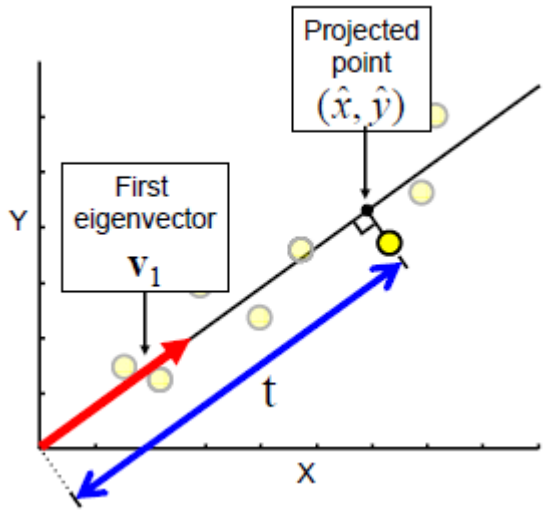

Figure 1.8 A geometric view of first eigenvector of PCA in two dimensions. From reference 40.

and is calculated as:

$$t = [x\,y]v_1 \tag{1.4}$$

PCA can generate additional eigenvectors, $\mathbf{v}_2$, $\mathbf{v}_3$, $\mathbf{v}_4$, …, $\mathbf{v}_n$, where n is the rank of the original data matrix. The second eigenvector should be orthogonal to the first one and describes the highest level of remaining variance that is not accounted for by the first eigenvector, Figure 1.9.

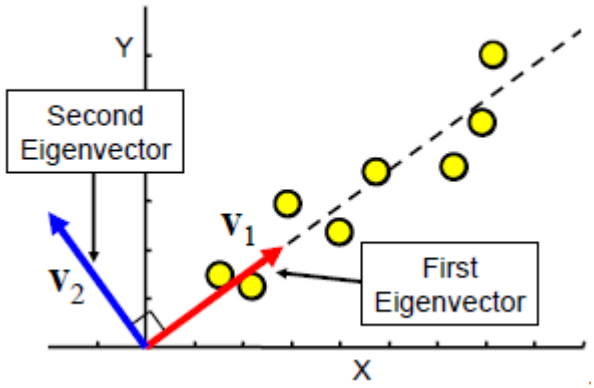

Figure 1.9 A geometric view of first and second eigenvector of PCA in two dimensions. From reference 40.

For higher dimensional data the third eigenvector is orthogonal to the first and second ones and should account for most of the remaining variance, which has not been accounted for by the first and second eigenvectors, and so on.

In conclusion PCA is a method that creates a new orthogonal coordinate system for data based on a simple rotation of the original coordinates while the smallest number of axes (dimensions) account for the largest amount of variance in the original data set (Figure 1.10).

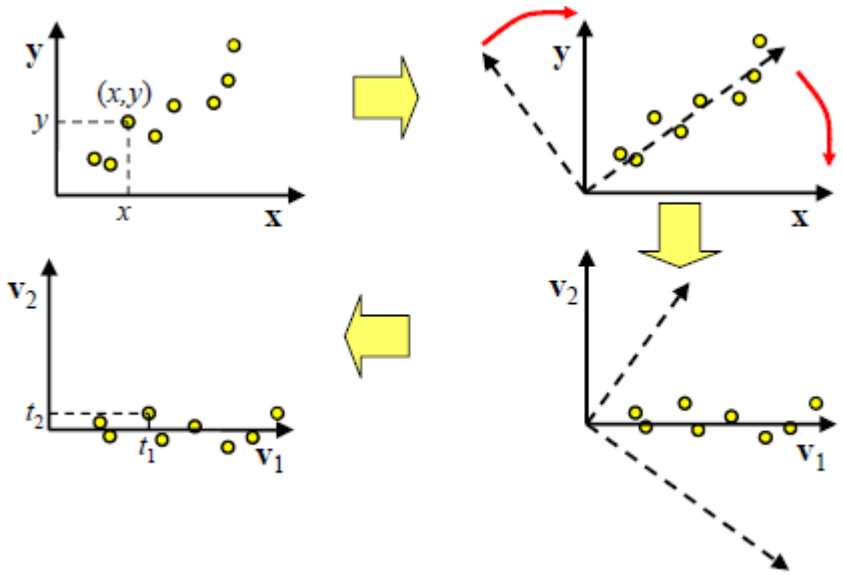

Figure 1.10 A geometric view of PCA in two dimensions.
From reference 40.

After applying PCA, the obtained new axes directions are defined by eigenvectors and the coordinates of each data point are given by the calculated scores. Figure 1.10, represents a geometric view of PCA in two dimensions. For a bivariate data set, **D**, the mathematical form employed in PCA model is shown in Equation (1.5).

$$\begin{bmatrix} x_1 & y_1 \\ x_2 & y_2 \\ . & . \\ . & . \\ . & . \\ x_m & y_m \end{bmatrix} = \begin{bmatrix} t_{11} & t_{12} \\ t_{21} & t_{22} \\ . & . \\ . & . \\ . & . \\ t_{m1} & t_{m2} \end{bmatrix} \begin{bmatrix} l_{11} & l_{12} \\ l_{21} & l_{22} \end{bmatrix} \qquad (1.5)$$

$$\mathbf{D = TL}$$

Where:

D = $m \times n$ data matrix (n: wavelengths/channels/dimension of measurement space, m: samples)

T = $m \times n$ matrix called the score matrix

L = $m \times n$ matrix called the loading (eigenvector) matrix

The score or the coordinate in the new system for each point is given by the rows of matrix **T**. The rows of the matrix **L** define the coordinate of each eigenvector in the original coordinate system. By presenting data in a new coordination that is defined based on the variance of the data, it is possible to reduce the dimensionality of the original data from n to p. This reduction can be done by creating new matrixes of **L** and **T**, which contain only the first p eigenvectors and their associate scores. In this way, the maximum amount of data variance (information) is retained when we discard the eigenvectors. In other words, a new set of variables provided by PCA can be used instead of the original data for analysis purposes. These new variables are called latent variables and just part of the information they carry would be good enough to describe the whole set of data of the signals whereas the rest mainly describes the noise.

According to the above, reducing variables mathematically means choosing the first p columns of matrix **T** and creating a new data set (linearly related to the original data set). To find an appropriate value for p (number of components), it is useful to monitor the residual while changing the value of p. If the residual does not become smaller with increasing number of components, p would be the correct value to choose for the number of components. Practically, one may program this algorithm by calculating the sum of squares of residuals (SSR). For a model with p number of components the sum of squared residuals is defined as:

$$SSR_p = \sum_{i=p+1}^{n} t_i \qquad (1.6)$$

The final decision for the value of the correct number of components can be made with the help of a Scree plot, i.e. a plot of log (SSR) against the number of components[41, 46]. This is illustrated in Figure 1.11 for a data set originally with dimension number of 10.

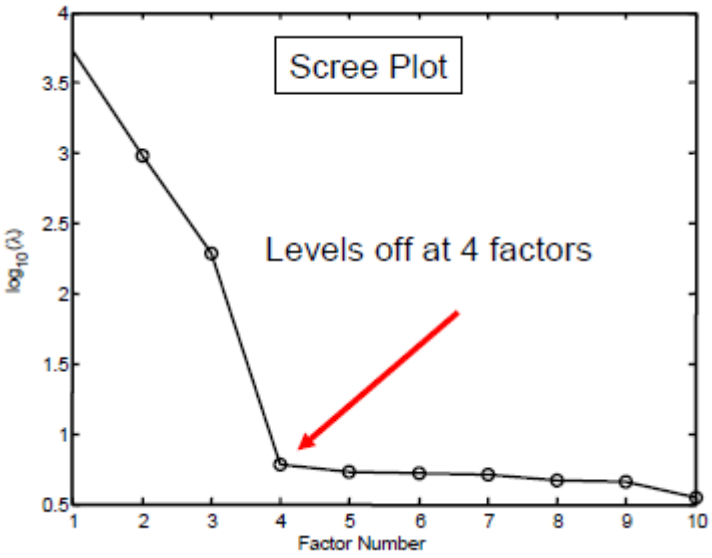

Figure 1.11 Scree plot.
From reference 40.

A logarithmic plot is used to shrink down the wide range of values on the vertical axis. Figure 1.11 indicates that the appropriate number for the related data set would be four since the residuals no longer decrease much when further increasing *p*.

After creating a new reduced data matrix with dimension of $m \times p$ instead of original $m \times n$ data set, the principal component regression can be applied to build a calibration model. To predict some variable, *y*, from a measurement vector, the regression vector, *b*, should be determined using a set of calibration samples, X. Then the determined regression vector can be used to predict *y* for unknown samples (Figure 1.12).

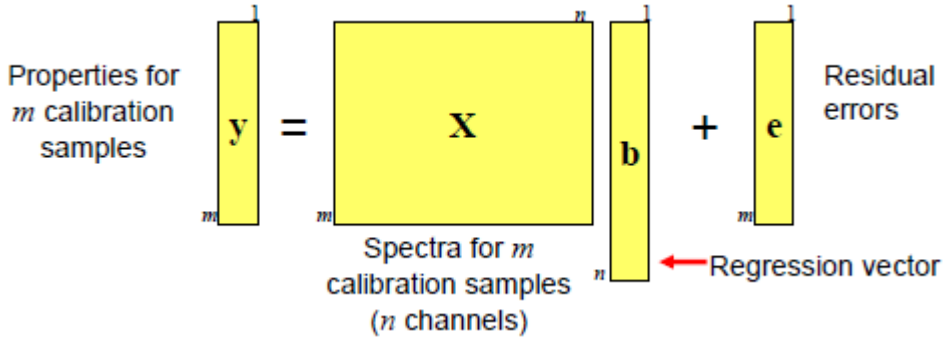

Figure 1.12 Determination of regression vector from the original data set.
From reference 40.

The regression vector is calculated as:

$$\mathbf{b} = \left(\mathbf{X}^{\mathbf{T}}\,\mathbf{X}\right)^{-1}\mathbf{X}^{\mathbf{T}}y \qquad (1.7)$$

When the PCA method is applied to the original data set (calibration and test) and the truncated score matrix $\tilde{\mathbf{T}}_k$ (k<< n, k is the number of components) is created, the PCR analysis will be much easier (Figure 1.13).

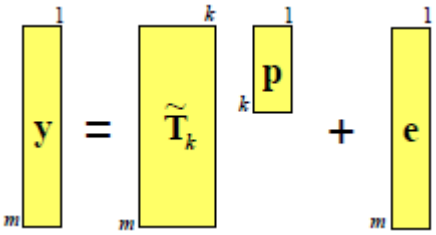

Figure 1.13 Determination of regression vector from the reduced data set.
From reference 40.

And the regression vector would be determined as:

$$\mathbf{p} = \left(\mathbf{T}^{\mathbf{T}}\mathbf{T}\right)^{-1}\mathbf{T}^{\mathbf{T}}y \qquad (1.8)$$

When the regression vector is determined, a method is required to measure the predictability of the alternative model. To confirm the stability to the model, the original data can be split into two parts as calibration (=training) and prediction (=validation) data sets. The calibration data set will be used to build a model whereas the prediction data set will be used to optimize and assess the predictive abilities of the model. In other words, the prediction data set is used to compare and choose the best model by assessing its predictive ability (Figure 1.14).

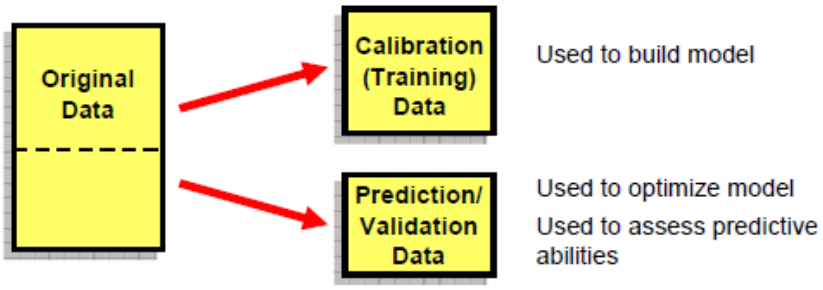

Figure 1.14 Splitting of original data set to calibration and prediction sets.
From reference 40.

The calibration and prediction set are not required to have the same size and samples for the two groups should be picked randomly to avoid systematic errors. To evaluate the model, one may calculate the root mean squared error of calibration (RMSEC) and prediction (RMSEP), which simply can be called the standard error of calibration (SEC) and prediction (SEP) respectively. Typically, RMSEC provides overly optimistic estimates of a calibration model's predictive ability.

$$RMSEC = \sqrt{\frac{\sum_{i=1}^{N_{cal}} (y_i - \hat{y}_i)^2}{N_{cal} - k}} \quad (1.9)$$

Where:

y_i is the true measured value of the property for sample *i*

$\hat{y}_i$ is the predicted value of the property for sample *i*

N_{cal} is the number of calibration samples

k is the correction of degrees of freedom, equals to the number of components

$$RMSEP = \sqrt{\frac{\sum_{i=1}^{N_{pred}} (y_i - \hat{y}_i)^2}{N_{pred}}} \quad (1.10)$$

RMSEP uses the same definitions except that the summation is over the number of prediction samples, N_{pred}. In this way, no degrees of freedom are lost, since none of these measurements were used in building the model.

1.4.4 Cavity Ring-Down Spectroscopy

Absorption spectroscopy is employed as an analytical chemistry tool to determine the presence and to quantify the amount of a particular substance in a sample. This

optical technique is simple, comparably inexpensive and applicable to many chemical compounds since most are capable of absorbing UV and visible light.

When the light passes through the sample some of the photons are absorbed by the analyte and the resultant intensity of the incident beam decreases. This is in accordance with the Beer-Lambert law:

$$A = \log \frac{I_0}{I} = \varepsilon C d = \alpha d \qquad (1.11)$$

As seen from Beer-Lambert law the absorbance, *A*, is directly proportional to the concentration, *C*, of the light-absorbing species, the extinction coefficient, ε, and the absorption path length, *d*,[16]. The absorption coefficient α is then given by εC.

By modifying the absorption spectrometer, it is possible to increase its sensitivity. These modifications are most useful if the dimensions of the spectrometer and the sample volume stay unchanged. When the absorption of a species in a sample is weak due to low concentrations or a low extinction coefficient, absorbance may be increased simply by increasing the sample path length. However, increasing the absorption length, *d*, may become unfeasible if the length becomes too great, or the sample volume is limited.

One solution to create a very long optical path whilst maintaining a compact sample volume is to use a multi-pass technique. The first multi-pass cell was invented in 1942 by John U. White[51], and is now known as the White cell. Other examples of multi-pass cells include Herriot cells[52] and astigmatic cells[53]. Multi-pass methods only became practical with the advent of laser as light sources since they remain collimated, intense and coherent beams over the entire length of a "folded" absorption path[54].

Cavity ring-down spectroscopy (CRDS), a sensitive absorption technique for quantitative measurements of analytes in the sample, was applied by O'Keefe and Deacon in 1988[55] to measure the optical absorption of a strongly forbidden electronic transition of molecular oxygen in the visible region of the spectrum. CRDS is a cavity enhanced, multi-pass absorption technique, which can be performed with either pulsed or continuous wave light sources[55]. In a typical CRD setup, as shown in Figure 1.15, light is coupled into an optical cavity, which is made from two highly reflective mirrors (reflectivities from 99% to 99.9999%). The fraction of light that is trapped into the cavity is reflected back and forth between two mirrors and at each reflection, a portion of light leaks out of the cavity and is detected (Figure 1.15). In CRDS, the absolute amount of absorbed light is not measured, but the temporal decay of the intensity in the optical cavity is recorded.

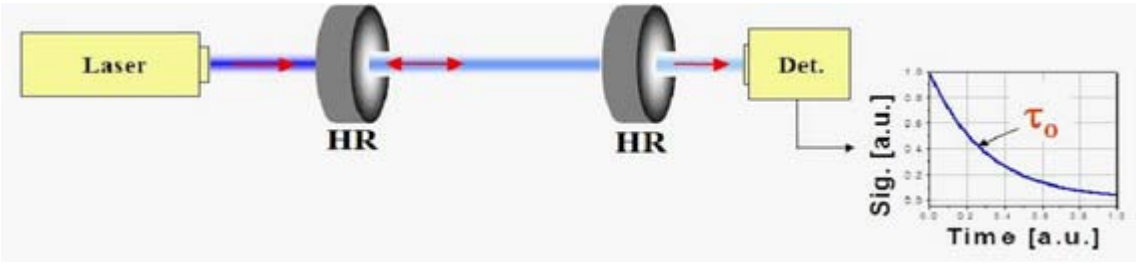

Figure 1.15 Cavity ring-down experimental setup.
From http://www.engr.colostate.edu/lpdl/research/CRDS/CRDS.html

The lifetime of the photon trapped in the cavity is directly related to the optical loss in the cavity, i.e. to the reflectivities of the mirrors, as well as absorption and scattering of the light in the cavity. This lifetime is called ring-down time and it is equal to the time at which the light intensity inside the cavity decreases to 1/e of its initial value. The ring-down time, τ, is independent of intensity fluctuation of the light source

or the efficiency of the detector and only depends on the total loss of intensity within the optical cavity [56]. Equation (1.12) expresses the ring-down time as a function of the round trip time of the cavity, t_{RT}, and the transmission per round trip, T_{rt}.

$$\tau = \frac{t_{RT}}{-\ln T_{rt}} \qquad (1.12)$$

The losses inside the cavity, i.e. losses at the mirrors and by absorption and scattering by the sample within the cavity, define the transmission per round trip T_{rt}.

The optical cavity was originally made from two identical mirrors and used almost exclusively with gaseous samples. In the last decade CRDS was used on other types of cavities made from e.g. fiber optic waveguides[57]. To build a fiber cavity, a strand of either single-mode or multimode fiber optic cable can be used where the end facets of it are reflective coated[58] or held in front of each other / connected to form a loop[56]. Also Fiber Bragg Gratings (FBGs) can be used to trap the light in the fiber cavity[59].

Using CRDS for liquid samples instead of gas samples is straightforward. While one could fill the entire cavity with the liquid sample[60] or place a sample cuvette into part of the cavity[61, 62], the roundtrip losses tend to be much higher and the sensitivity is consequently reduced.

In the next section, 1.4.5, we present another simple approach to apply cavity ring-down absorption spectroscopy on liquid samples. Fiber-Loop Cavity Ring-Down Spectroscopy (FLCRDS) uses a fiber-loop cavity, is simple and inexpensive, and is quite suitable for online designs.

1.4.5 Fiber-Loop Cavity Ring-Down Spectroscopy

An optical cavity can also be obtained using optical fibers. For example the ends of a strand of multimode fiber can be connected to form a ring cavity[56, 63, 64] (Figure 1.16).

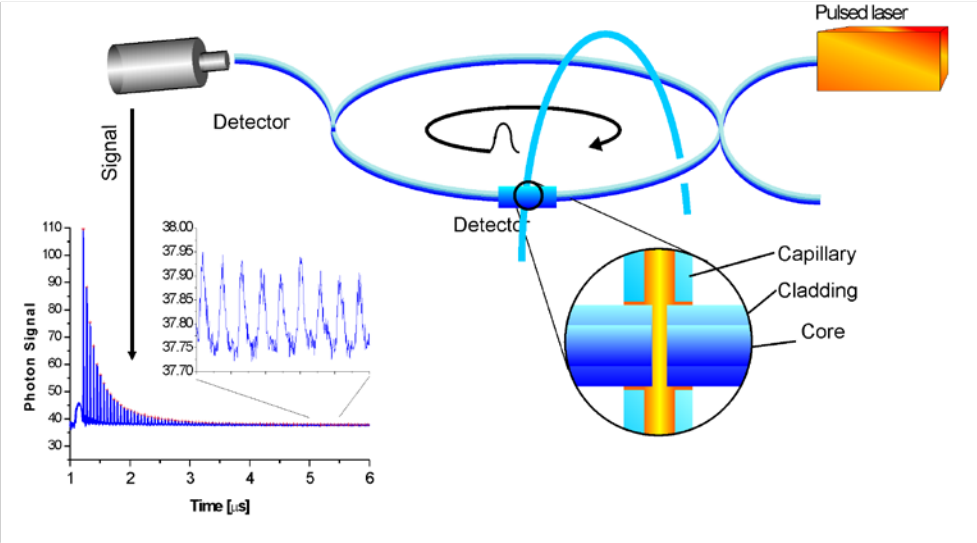

Figure 1.16 Fiber-loop cavity ring-down experimental setup.

The cavity amplifies the response of *any* sensor element that is included in the loop and reacts on an external stimulus. The sensor element responds by changing its light transmission. It could be an absorption cell (trivially, just a small gap between the ends of the fiber strand), which holds a liquid sample and allows interaction of the light with the sample. Fiber-loop cavities are broadband and the round trip loss over the entire transmission range of the fiber material is low. Nevertheless the roundtrip loss is always higher than what can be achieved by a well aligned optical cavity containing two highly reflective mirrors. The calculation of the ring-down time in fiber-loop cavity ring-down spectroscopy (FLRDS) is similar to CRDS, (Equation (1.12)), however the round trip

time is defined differently with respect to the cavity length. In CRDS the related length of one round trip is twice the length of cavity, *l*,:

$$t_{RT(CRDS)} = \frac{2l}{c_0} \tag{1.13}$$

c_0 is the speed of light in vacuum.

In FLRDS a ring-cavity is used, so the length of cavity equals the length of the loop. Since the speed of light, depends on the refractive index of the fiber medium, *n*, the round trip time for a fiber-loop cavity with length of *L* is expressed as:

$$t_{RT(FLCRDS)} = \frac{nL}{c_0} \tag{1.14}$$

Using Equations (1.12) and (1.14), the ring-down time in a fiber cavity can be given as:

$$\tau = \frac{nL}{c_0(-\ln T_{rt})} = \frac{nL}{c_0(-\ln T_{sensor} + \alpha_f L)} \tag{1.15}$$

Where T_{sensor} is the optical transmission of the sensor element and α_f is the absorption coefficient of the fiber. The losses across the sensor element are attributable to the combination of the absorption of light by the sample and losses from coupling through the sensor element. For example, if a gap between two fiber ends acts as a sensing element and the sample is introduced into it, the loss term is given by:

$$-\ln T_{sensor} = -\ln T_{gap} + \varepsilon Cd \tag{1.16}$$

Here, the term $-ln\ T_{gap,}$ describes the coupling losses across the gap between the two fiber ends and εCd is the Beer-Lambert law term (Equation (1.11)) that expresses the absorption effect of the sample. So, for the transparent blank sample containing no absorbing analyte;

$$\tau_0 = \frac{nL}{c_0\left(-\ln T_{gap} + \alpha_f L\right)} \tag{1.17}$$

Finally the concentration of an analyte can be calculated by the relative ring-down time as:

$$\tau = \frac{nL}{c_0\left(-\ln T_{gap} + \varepsilon Cd + \alpha_f L\right)} \tag{1.18}$$

$$\varepsilon Cd = \frac{nL}{c_0}\left(\frac{1}{\tau} - \frac{1}{\tau_0}\right) = \frac{t_{RT}}{\tau} - \frac{t_{RT}}{\tau_0}$$

The light that is coupled to a fiber can be guided in the core within the acceptance cone, as well as the cladding of the fiber when the incident ray angle may be bigger than acceptance angle. The decay rate in the fiber core and cladding is different. Loses in the fiber cladding modes are much higher than in the core modes and so the decay rate is larger. Since, in a multimode fiber core, many modes are excited simultaneously, the

intensity decay would not be a single exponential function and multimode decay with ring–down time and amplitude a_i can be expressed as:

$$I_{(t)} = \sum_{i}^{N} a_i \exp(\frac{-t}{\tau_i}) \qquad (1.19)$$

In practice these several thousand modes have quite similar decay rates and a fit with a single exponential function is possible.

2 Chapter 2. Oil Analysis and Monitoring

2.1 General Overview and Historical Perspective

As was explained in the previous chapter, for healthy machinery operation one requires up-to-date knowledge of the lubricant condition. An oil analysis program helps configure a reliable machinery maintenance schedule while preventing unnecessary early maintenance, or, worse, machine damage from a belated overhaul. Oil analysis comprises two closely related objectives:

- To check the quality of the lubricant in order to ensure that it is in good condition.
- To inform the operator of the condition of the machinery components.

The results of the oil analysis define the time when machine maintenance is required. For example, it can identify the need for partial or complete oil change or even recommend that the lubricant remains in service for a longer time. Most importantly, the early detection of oil degradation and contamination allows for a timely service that may prevent costly machinery failure and unsafe operation.

The analyses of both in-service oil and used-oil are very important indicators of machinery condition, while new oil is analysed as a reference. Here, “in-service oil” refers to oil that is analysed while in the machinery and “used oil” refers to oil that is discarded after an oil change. Most industries currently use off-site analysis in dedicated laboratories that use the American Society for Testing and Materials (ASTM) standard methods to analyze all oil samples - new oil, in-service oil and used oil. However, on-site oil analysis is getting popular due to its lower cost and faster turn-around-time, avoiding

sample transportation to the lab. In addition, a real-time monitoring system using in-line sensors is becoming a high priority for machinery operators. Regardless of whether the analysis is conducted off-line or online, multiple oil analysis strategies are needed to meet all the requirements of oil condition monitoring.

Denver, Rio Grand and Western Railway (DRGW) was the primary developer of machinery oil analysis starting in the early 1940s. The DRGW oil analysis program began with spectrographic tests for wear metal debris detection in order to monitor the health of their, then new, locomotive diesel engines. With the transition from steam to diesel engines, the initial oil analysis program became popular as a reliable engine monitoring method. The analytical procedures by the DRGW program were continuously improved to develop condition-based maintenance (CBM). Oil analysis program became predominant in most of the railway industries during 1980s. In 1955, the United States military became interested in the oil analysis program and in 1962 the US Air Force started to implement its own oil analysis program to identify mechanical problems in aircraft engines. The three divisions of the US military - army, air force and navy - designed a program known as the Joint Oil Analysis Program (JOAP) in 1975 to consolidate the operation and management of the individual service programs. Besides the machine operators, the machine suppliers ("Original Equipment Manufacturers, OEMs") also adopted the oil analysis program to support the testing of their products. Since the 1960s, the JAOP has been used by many OEMs and most industrial and commercial equipment users to minimize the cost and labour associated with machinery maintenance.[2]

In order to identify the needs for machinery oil analysis, it is essential to first review the machinery lubrication performance, machinery failure modes, lubricity testing, and the interpretation of test data.

In chapter 1, the types and functions of lubricating oils were briefly introduced. A reliable lubricant should be capable of operating under stress conditions and over a wide range of temperatures. The properties required for the performance of lubricants in each application are determined from a series of standard test methods as implemented by the ASTM, the International Organization for Standardization (ISO), the Society of Automotive Engineers (SAE), and others[65, 66, 67, 68].

2.2 Lubricant Failure Modes

2.2.1 Lubricant Appearance Change

When lubricants age or become contaminated their appearance often changes. Changes in oil color, odor, consistency and viscosity are noticeable symptoms of changes in oil condition. Observing these changes is the first step in determining the machinery fluid condition. For example, when an oil sample has a milky or emulsified appearance, it could mean that oil is contaminated with water, or alternatively, when the oil is degraded and oxidized, its colour turns to a brownish hue due to the presence of oxidation products.[2]

2.2.2 Contamination Related Failure Modes

Lubricant contamination is one of the main reasons that lead to machinery failure. Contaminants speed up oil degradation, deplete additives, and may change the viscosity. Frequent oil analysis should be applied to ensure that a lubricant is free of contamination. Water, glycol, fuel, particulates, and dirt are the most harmful contaminants to oil.

Water usually finds its way into the lubricating system during equipment cleaning, from exposure to the environment – especially humid air –, or from leaking coolant. Water decreases the lubrication ability of the oil while increasing the rate of oxidation processes. For example, the polyol-ester base stock, which is used in aviation lubricants, breaks down in the presence of water into alcohols and carboxylic acids, in a reversal of its manufacturing process. Antifreezes that contain ethylene glycol are used for protection from cold temperature freeze-up and are sometimes found in the lubricant system as a contaminant. Glycol may then react with the oil base stock or with additives and, as a result, the oil composition changes and the viscosity typically increases. Oil dilution with fuel from over-fuelling, broken or worn fuel injectors or leaking fuel / oil heat exchangers lowers the lubricant oil viscosity and its flash-point.

2.2.3 Degradation Related Lubricant Failure Modes

Lubricants age during machinery operation at high temperatures while exposed to oxygen. In the presence of some contaminants, the rate of degradation increases significantly. Of course, the reaction of atmospheric oxygen with lubricants is an

undesirable process. Oxidation is one of the major causes of the lubricant oil degradation and can be influenced by several factors such as high engine temperature, the rate of air circulation, water contamination and metallic wear debris, concentration and efficiency of antioxidants and other additives as well as the type of hydrocarbon-based lubricant base stock itself[4]. Different types of oils experience different degradation mechanisms but in general, aging is caused by the formation and the propagation of radicals in the fluid. Free radicals can be the products of the reaction between oil constituents (base stock or additives) and oxygen, but can also be produced by thermolysis at high temperatures. Since this thesis focuses mostly on aviation lubricants, the degradation process of synthetic oils will be explained in more detail below.

2.2.3.1 Degradation of Synthetic Ester Lubricant Oil

As was explained in the introduction, lubricant oils used in industrial machinery such as gas turbine engines, e.g. aircraft engines, are synthetic oils composed of esters. Oil oxidation leads to the formation of acidic compounds that are typically characterized by the so-called Acid Number (AN) which may be obtained according to ASTM guidelines[69, 70].

Also, the so-called breakdown number is used in case of ester base stock lubricant oils such as the synthetic polyol esters commonly used as aviation and aerospace lubricants. The resulting polyol ester degradation products can be observed as IR

absorption features at 3595 cm^{-1} to 3500 cm^{-1} and 3325 cm^{-1} to 3150 cm^{-1} and are quoted, respectively, as ester based-stock breakdown number I and breakdown number II[71].

The presence of antioxidant additives delays the oxidation of base fluid by intercepting the oxidation process and forming stable radical reaction products that do not react further. Antioxidants sacrificially protect the oil molecules and are gradually consumed during this process. Once the antioxidants are depleted, the oxidation of the base stock becomes a chain reaction (this reaction is sometimes described in the literature as autocatalytic[4]) as long as oxygen is diffused into the liquid at high temperature. Eventually the oil breaks down and machinery failure is imminent. In summary, the useful lifetime of the lubricant corresponds to the duration of the depletion of antioxidants, since the oxidation of lubricant oil begins once the antioxidants are consumed[6].

Current monitoring methods determine the quantity and identity of the base stock oxidation by-products, while the lubricant stays largely unharmed in the presence of antioxidants. In contrast, in this study, we focus on the antioxidants' performance and not on the changes of base stock composition.

The degradation and oxidation of all types of lubricants including synthetic base stock proceeds by autocatalytic reactions described by well-established radical mechanisms[1, 72]. Oxidation processes of hydrocarbons in lubricant oils are divided into low (30-120°C) and high (>120°C) temperature phases. Oxidation in the low temperature phase consists of four stages:[73]

1. Induction of the radical chain reaction
2. Propagation of the radical chain reaction

3. Chain branching

4. Termination of radical chain reaction

In the presence of oxygen, the induction of the radical chain reaction (1) is catalysed by traces of transition metal ions, and is called initiation stage, (Reaction 2.1).

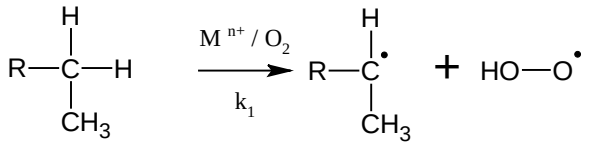

Reaction 2.1

The rate of the initiation reaction is slow and the reaction produces alkyl radicals. In this step, oxygen attacks the hydrocarbon molecules and abstracts the most labile hydrogen atom. The reactivity of the attacked site decreases in the following order: benzylic > allylic > tertiary alkyl > secondary alkyl > primary alkyl hydrogens[4] and is governed by the stability of the radical product. The produced radicals irreversibly react with oxygen and the lubricant to form peroxy radicals and hydroperoxides in step (2). This step is known as propagation,

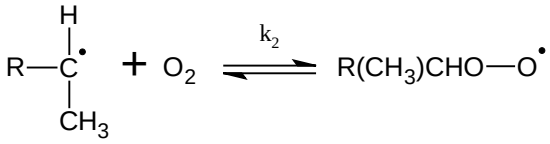

Reaction 2.2

The reaction rate of alkyl radicals with oxygen is dependent on the substituents bound to the carbon atom, the radical center. For example, iso-paraffins are oxidized 10 times faster than n-paraffins.

In the chain propagation process (2), the peroxy-radicals abstract hydrogen from another hydrocarbon molecule thereby creating a hydroperoxide and an alkyl radical.

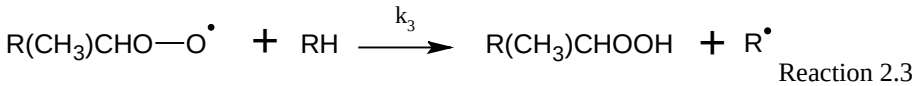

Reaction 2.3

The new alkyl radical can react again with oxygen according to reaction 2.2. Since the rate of reaction 2.3 is slower than reaction 2.2, it is the rate-determining step in the chain propagation mechanism. Peroxy radicals have a comparatively high stability and low reactivity so their concentration is often higher than that of other radicals. Alternatively, peroxy-radicals may abstract hydrogen via an intermolecular propagation reaction, reaction 2.4.[4, 74]

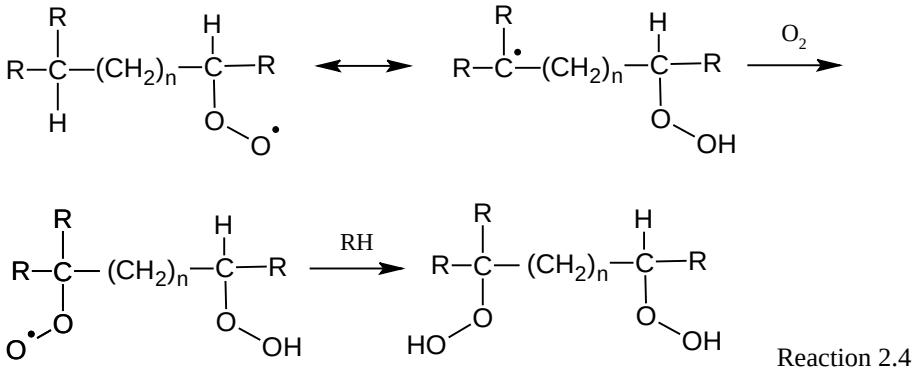

Reaction 2.4

The next stage (3) is chain branching which starts with the thermal cleavage of hydroperoxides to alkoxy and hydroxyl radicals[75].

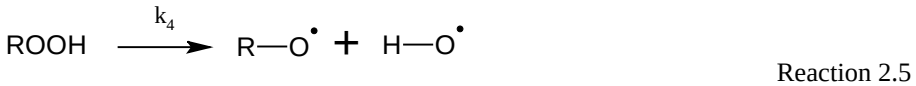

Reaction 2.5

Reaction 2.5 has a high activation energy and plays an important role in hydrocarbon degradation at high temperatures[5]. Since the hydroxyl- and alkoxy-radicals are quite reactive, they attack lubricant molecules to gain hydrogen atoms through non-selective reactions as shown below[4, 6] ;

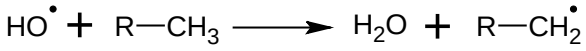

Reaction 2.6

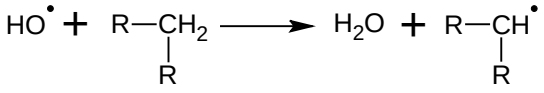

Reaction 2.7

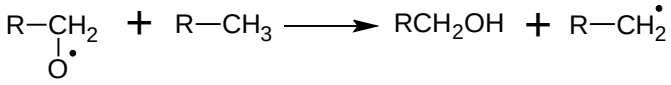

Reaction 2.8

Aldehydes and ketones may be the final products in this stage as shown schematically in reactions 2.9 and 2.10[6, 76].

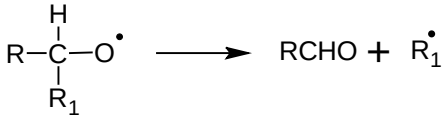

Reaction 2.9

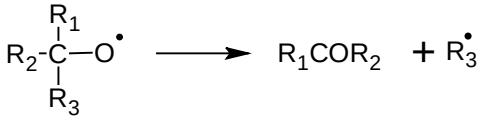

Reaction 2.10

The increase of free radical concentration is a result of hydroperoxide production and its subsequent decomposition. The produced radicals initiate new chain reactions as explained above. Hydroperoxides may also decompose via a bimolecular mechanism, shown in reaction 2.11 as an advanced state of oxidation[77].

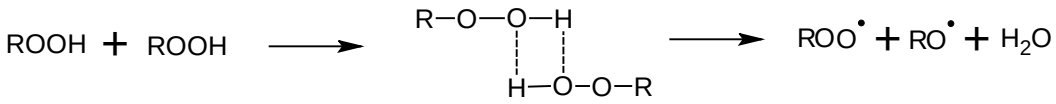

Reaction 2.11

Termination of the radical chain reaction (4) is the last stage of the lubricant degradation process. During this step, the radicals either self-terminate (reactions 2.12 and 2.13) or are scavenged by radical scavengers / oxidation inhibitors.

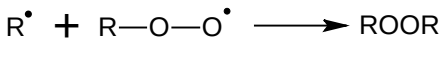

Reaction 2.12

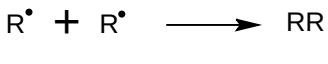

Reaction 2.13

Aldehydes and ketones formed in the previous stages are quite reactive at elevated temperatures and may produce polymers and heavy molecules in the presence of acids, such as nitric and sulfuric acids.

At high temperatures, above 120°C, initiation and propagation steps are similar to those at lower-temperatures, 30-120°. Oxidation products of the first and second degradation stages are the same, i.e. mostly hydroperoxide compounds. The dissociation of hydroperoxides is very important and is the rate determining process at high

temperatures. This leads to an increase of hydroxyl radicals that non-selectively abstract hydrogen atoms. Carboxylic acids, one of the principal oxidation products at high temperature, are formed through the following reactions[4, 6, 78].

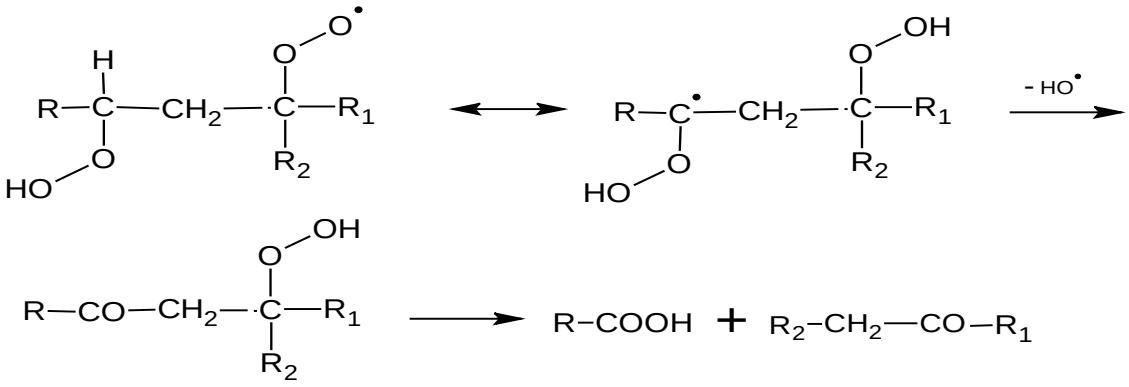

Reaction 2.14

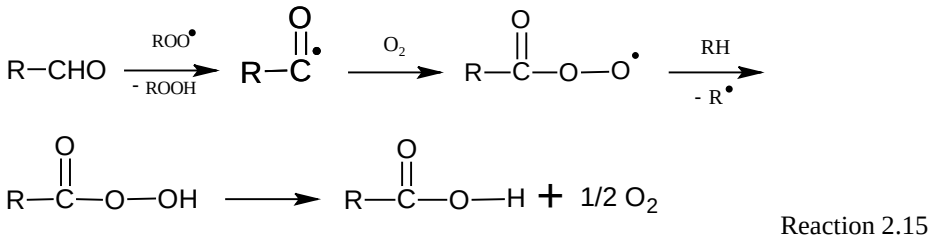

Reaction 2.15

Similar to the low temperature reactions, at high temperatures the termination reactions also proceed to high molecular weight products. At temperatures above 120°C, peroxy radicals can interact with each other in a non-terminating process (reaction 2.16) to produce alkoxy radicals which can contribute to subsequent chain branching reactions.

Reaction 2.16

The rate of polymerisation is increased in the presence of metals such as iron which results in a precipitating sludge that is no longer soluble in the hydrocarbon oil. This causes thickening of the oil and increases the viscosity of the lubricant.

As was previously mentioned, the radicals produced during oxidation can be captured by inhibitors. Oxidation inhibitors interrupt the radical chain reactions by either reacting with the active radicals or by decomposing the hydroperoxydes. Oxidation inhibitors are classified based on their mode of action and will be explained in next section, 2.2.4.

2.2.4 Influence of Additives

Lubricants are strengthened with a mix of additives that are used to protect the oil and increase the useable oil life time. Lubricant and oil suppliers blend base stock with additive packages to meet the particular performance requirements. To comply with the equipment requirements and protect moving parts, lubricant additives are usually supplied as performance packages and blended in base stock. The performance package contains many classes of additives[1, 2]:

- stabilizer or deposit control agents contain oxidation inhibitors, dispersants and detergents.
- film-forming agents contain friction modifiers, antiwear additives, rust and corrosion inhibitors

- polymeric additives contain viscosity modifiers, pour point depressants and foam inhibitors

Additives, which minimize the amount of deposit formation, control and delay oxidative decomposition of lubricants, keeping the insoluble contaminants dispersed in the lubricant and protecting metal surfaces from attack by acidic oxidation by-products. This class of agents plays a significant role in the development of the lubricant's stability and functions by preventing lubricant composition reversal. Since stabilizing agents, specifically antioxidant additives, protect oil from the primary processes of degradation and oxidation, it is essential to study the depletion mechanisms of these additives. As long as antioxidants are present, the lubricant likely operates properly and safely. As soon as antioxidants are consumed, the lubricant base stock is left unprotected and starts to degrade during engine operation. For effective oil analysis and additive depletion-monitoring programs, specific knowledge of the contents of the additives is required. The main group of antioxidants including oil-soluble organic and organometallic additives, are classified as[4, 6]:

- Sulfur compounds
- Sulfur-nitrogen compounds
- Phosphorus compounds
- Sulfur-phosphorus compounds
- Aromatic amine compounds
- Hindered phenolic (HP) compounds
- Organo-copper compounds
- Boron compounds

Sulfur and sulfur-nitrogen compounds were the first types of antioxidants used by lubricant industry. Dibenzyl sulfide and dixylyl disulfide are two examples of aromatic sulphide additives. Alkyl and aryl phosphites such as tributyl phosphite and triphenyl phosphite are used in some petroleum based oils as antioxidants. For high-efficiency performance, phosphites may be mixed with aminic antioxidants to produce synergistic effects. Sulfur-phosphorus compounds are well known as powerful antioxidants for the protection of hydrocarbons. These compounds are very effective in a wide variety of base stock due to containing both elements in a single molecule. Zinc salts of dithiophosphoric acids (ZDDP) are oxidation inhibitors that show good anti-wear properties and protect metal surfaces against oxidation products. Another type of antioxidants used extensively in industrial and automotive lubricants are hindered phenols, e.g., 2,6-di-tertiarybutyl-4-methylphenol (BHT) and 2,2-methylenebis (4-methyl-6-tert-butylphenol). Amine derivatives such as alkylated diphenylamines (ADPAs) and alkylphenyl-α-naphthylamines (APANs) are the most important classes of amine antioxidants for various industrial lubricants and engine oils, specifically in synthetic-base aviation oils. Sample structures of antioxidants mentioned above are illustrated in Figure 2.1.[1]

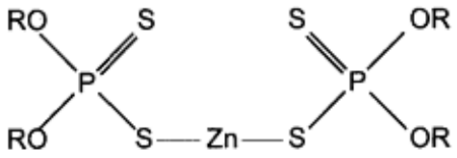

where R is typically $C_3 - C_8$

zinc dialkyldithiophosphate

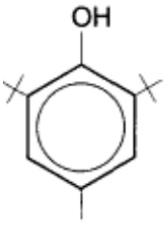

2, 6 - ditertiarybutyl - 4 - methylphenol (BHT)

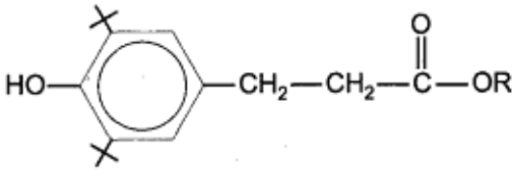

where R is $C_8 - C_{16}$

long-chain esters of substituted hydroxybenzenepropionic acid

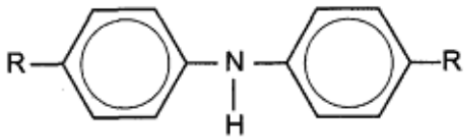

where R is $C_4 - C_9$

dialkyldiphenylamine

Figure 2.1 The structure of some common turbine oil antioxidants.
From reference 1.

2.2.4.1 Inhibition of Oxidative Degradation of Lubricants

Oxidation of base stock oil proceeds in a free radical process (Schematic 2.1). This radical chain oxidation reaction can be inhibited by interrupting the chain propagation and branching stages.

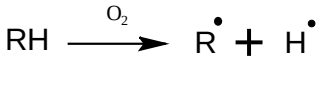

Initiation

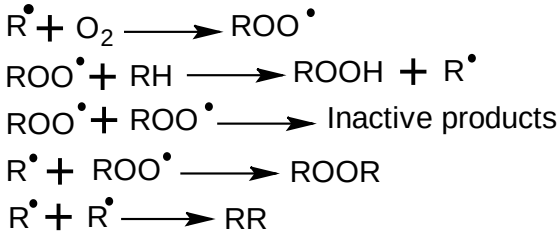

chain propagation

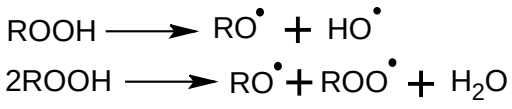

chain branching

Schematic 2.1 A summary of stages one to three of lubricant oxidation process; Initiation, chain propagation and chain branching stages

Antioxidant additives are classified according to their function in preventing lubricant degradation, in three groups[1, 6]:

- Radical scavengers
- Hydroperoxide decomposers
- Synergistic mixtures of radical scavengers and hydroperoxide decomposers

Radical scavengers are also called “primary antioxidants”. For an antioxidant compound to be efficient, radicals, such as alkoxy or alkyl peroxy radicals must abstract hydrogen atoms faster from the antioxidant compound than from the base

hydrocarbons[79]. Hindered phenols and aromatic amines act as radical scavengers by donating a hydrogen atom to the radical molecules (Schematic 2.2).

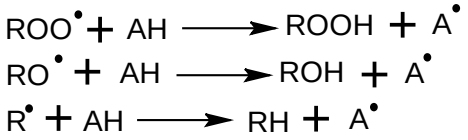

Schematic 2.2 Oxidation inhibition by radical scavengers (AH).

As is shown in Schematic 2.1 and Schematic 2.2, the propagation steps of the oxidation processes are interrupted by antioxidants. The produced antioxidant radical, $A^{\bullet}$, is typically stabilised through resonance and will not attack lubricant molecules though abstraction of a hydrogen atom. However, the antioxidant radical may react with another radical to produce a stable or non-reactive compound.

Peroxide decomposers are known as “secondary antioxidants”. They function by converting hydroperoxides into non-radical and less reactive products. Accordingly, peroxide decomposers interrupt the degradation process by preventing the chain propagation reaction[80]. Organosulphur, organophosphorus antioxidants and also additives containing both sulphur and phosphorus elements such as ZDDPs are used widely as secondary antioxidants. Reaction 2.17 presents an example of the hydroperoxide decomposition mechanism[1].

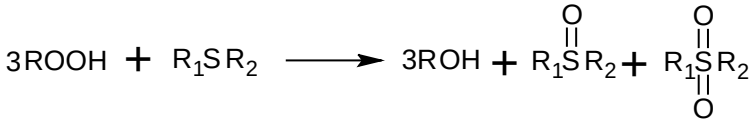

Reaction 2.17

Sometimes the efficiency of an antioxidant can be increased, if it is combined with another type of oxidative inhibitor. Hence, the presence of two different radical scavengers in a lubricant improves protection compared to either one alone. This type of additive function is known as synergistic mechanism. Synergism may occur between a primary radical scavenger, and a secondary hydroperoxide decomposer as well[81]. The mechanism in Schematic 2.3 shows synergism between aminic and phenolic antioxidants[4].

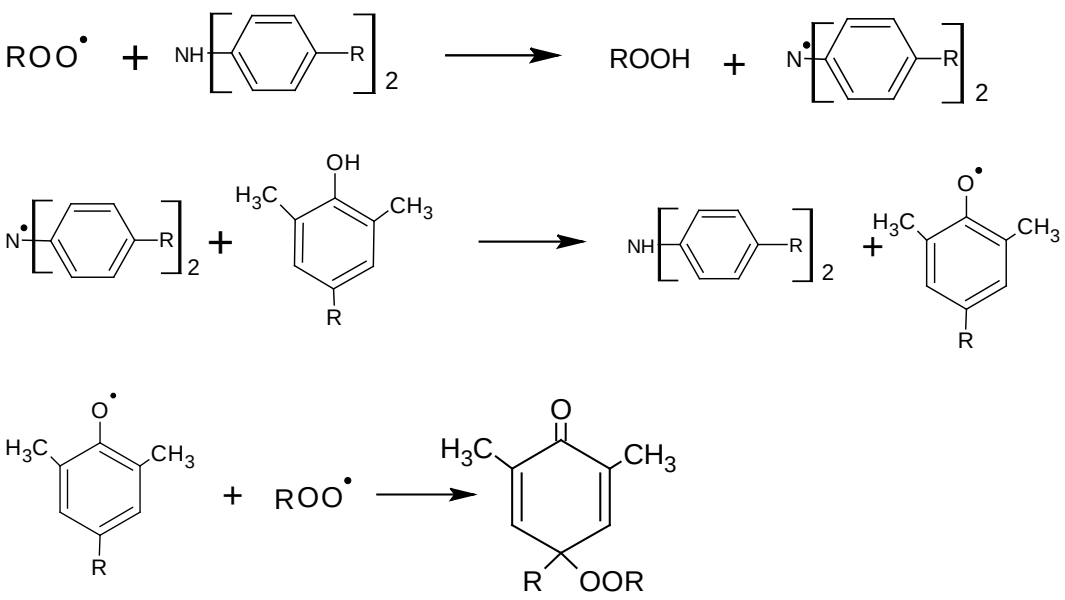

Schematic 2.3 Synergistic mechanism between aminic and phenolic antioxidants.

Hindered amine compounds are the most common antioxidants blended with ester-based turbine oils. Phenyl-α-naphthylamine, PAN, octylphenyl-α-naphthylamine, OPAN, and dioctyldiphenylamine, DODPA, are examples of antioxidants widely used in aviation engine oil[1, 2]. Usually two or more antioxidants are used in turbine lubricants because of the synergistic effect. Due to the oxidation and thermal stability required for aviation engine oils, such as jet turbine oil, combinations of oligomeric and monomeric

amine antioxidants are used in antioxidant packages. Another way to increase the efficiency of antioxidants is to use monomeric antioxidants that polymerize during the radical scavenging process to form oligomers with antioxidant properties. This greatly increases the antioxidants' effectiveness as oligomers provide additional antioxidant capabilities.

The antioxidancy function of aromatic amines begins with the donation of a hydrogen atom to the free radicals and the formation of stable aminyl radical. The reaction pathway that the aminyl radical follows changes depending on the temperature[4, 82]. Schematic 2.4 presents the inhibition mechanism by ADPA at high temperature (>120°C). The inhibition mechanism studied for another aromatic amine antioxidant, PAN, will be discussed in detail in chapter 3.

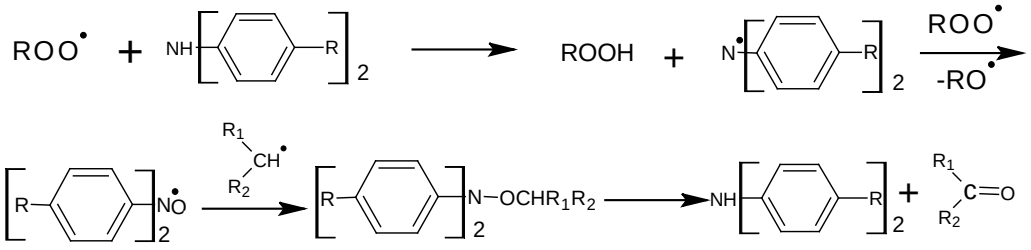

Schematic 2.4 Inhibition mechanism by ADPA at temperature above 120ºC.

2.3 Condition Monitoring Test Methods

Oil lubricants are complex and expensive products that require a routine condition monitoring program to ensure their reliable performance. To increase the usable lifetime of a lubricant, periodic sampling and testing is essential. Moreover, cost-effective

equipment operation relies on good lubricant performance. Finally, the cost of machinery maintenance can be reduced if lubricant failure is detected early. An oil analysis program must therefore detect and quantify the early onset of lubricant performance failure that may eventually result in loss of equipment function. Oil analysis tests generally are classified into two categories:

- Tests to monitor contamination such as water, dirt, fuel, glycol
- Tests to monitor oil degradation

Oil analysis techniques for monitoring contamination and degradation include infrared (IR) spectroscopy[71, 83], particle counting (PC), elemental metal analysis (using e.g. atomic emission and absorption spectroscopies), X-ray fluorescence (XRF), viscosity measurements, and gas chromatography (GC), which may be coupled to mass spectrometry (GC-MS). Test methods such as "oxidation induction time of lubricating oils" measurements by Pressure Differential Scanning Calorimetry (PDSC) and Remaining Useful Life Evaluation Rig (RULER) can be part of oil analysis program. The above techniques are applied either off-line, in-line or in online sensors[1, 2].

ASTM has developed a set of test methods to determine the condition of in-service fluids. The ASTM E2412 test method describes the infrared parameters associated with oil failure modes, contamination and degradation. Different machinery oils have different IR spectra and hence one must use different IR absorption windows to measure the concentration of a particular contaminant or oil-degradation indicator[71]. The next few paragraphs describe IR analysis methods that can be used as lubricant condition indicators for different types of oils.

Water, which is the most common lubricant contaminant, strongly absorbs at most of the wavelengths in the electromagnetic radiation. In petroleum engine oil, the most useful absorption window to detect water lies between 3600 - 3150 cm^{-1}. The O-H bond stretch vibration can be detected easily in petroleum base oils that have no significant absorption features in that region, as seen in Figure 2.2.

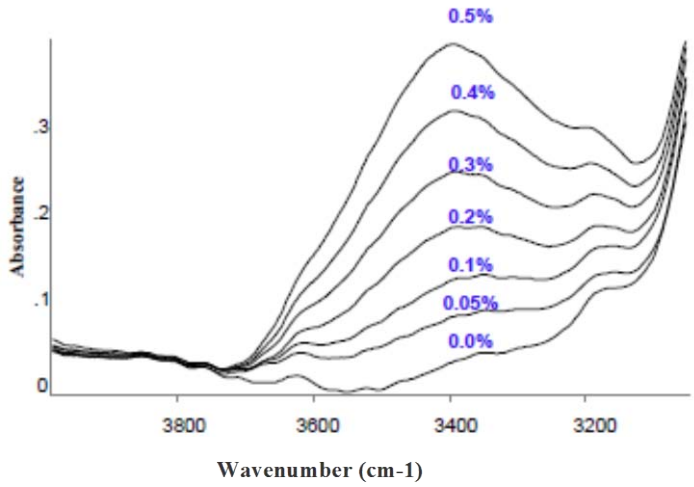

Figure 2.2 IR response to water contamination in crankcase, petroleum, oil.
The percentages represent water concentration. From reference 2.

As is shown in Figure 2.3, the range of 3700 - 3595 cm^{-1} can be used to detect water contamination in polyol ester base stock. This area corresponds to free hydroxyl groups and does not interfere with other IR absorption features of the polyol ester base stock in the 3400 cm^{-1} region.

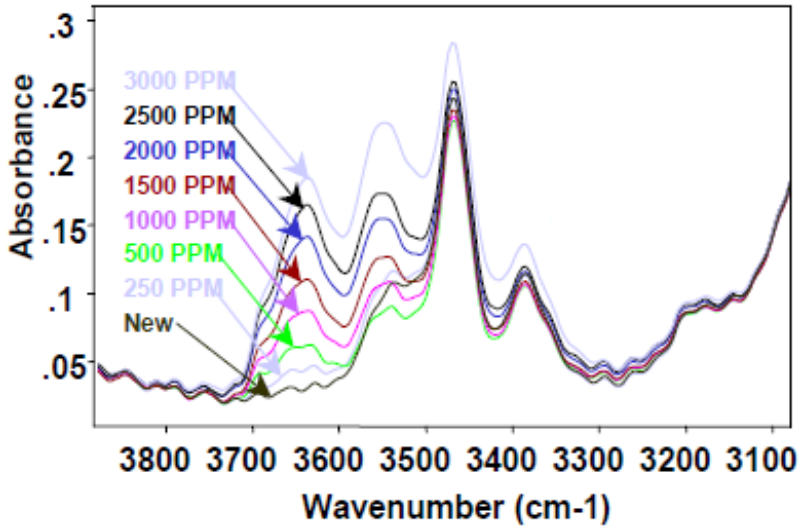

Figure 2.3 IR response to water contamination of polyol ester turbine oil.
Mil 23699 lubricant with different water concentration. From reference 4.

However, the water detection regions are different for petroleum crankcase oils, synthetic ester oils, as well as industrial hydraulic oils. The IR response of water in hydraulic oils that contain extreme pressure (EP) additives and emulsifier additives, is characterized by a constant baseline shift (from 3400 to 3250 cm^{-1}), as is shown in Figure 2.4.

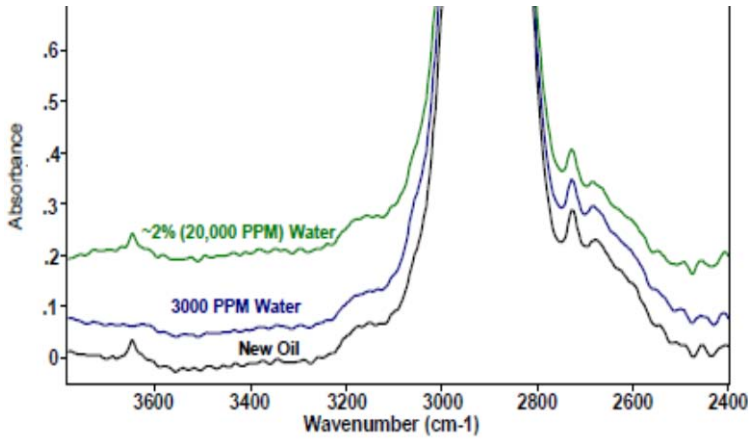

Figure 2.4 Water contamination measurements in EP fluids.
From reference 2.

The ASTM E2412 test method describes the regions in the IR spectrum corresponding to the absorption features of fuel and glycol contamination in engine oils. Diesel and jet fuels, JP5/JP8, contain additives with aromatic structures that produce characteristic contaminant marker bands in the IR spectrum of engine oil. The strongest signal, which is used as an indicator for contamination of oil with fuel, is the peak between 815 – 805 cm^{-1}, (Figure 2.5). The figure also demonstrates that there is a clear need for an improved detection method.

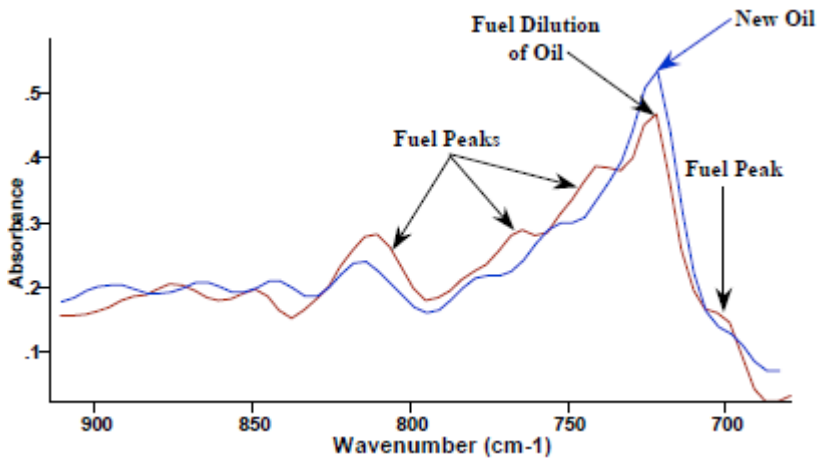

Figure 2.5 IR spectum of fuel in engine oil.
From reference 2.

In cold environments, antifreeze that consists of ethylene glycol is used for protection against system freeze-up and breakage. As a universal chemical solvent, glycol is harmful to the lubrication system and may lead to accelerating oxidation and thickening of the oil. The strongest IR absorbance bands in glycol are from the O-H stretch and C-O stretch doublet, which overlap with the absorbance of water and other organic compounds, respectively. To avoid these overlap regions, the glycol

concentration is measured though absorption at the characteristic peak in the region of 1100 to 1020 cm^{-1}, as shown in Figure 2.6.

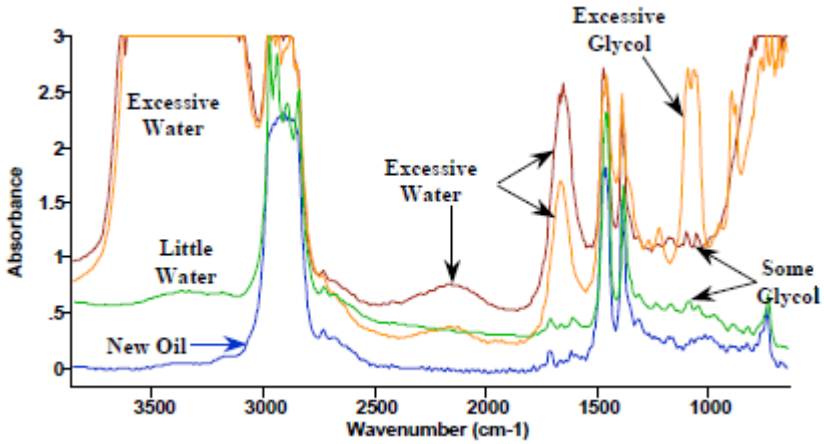

Figure 2.6 Glycol contamination measurement in diesel engine oils.
From reference 2.

IR analysis can also be used to determine the degradation level of oil. In petroleum oils, oxidation by-products are measured in the range of 1800 – 1670 cm^{-1}. This is the carbonyl region of the spectrum and it is characteristic for aldehydes, ketones and carboxylic acids. In ester base stocks, there are two IR regions that can be used to measure oxidation by-products, 3595 – 3500 cm^{-1} and 3330 – 3150 cm^{-1}. These regions indicate breakdown compounds containing hydroxyl groups, such as alcohols and carboxylic acid groups, and are known as breakdown area I and breakdown area II respectively. These regions are shown in Figure 2.7.

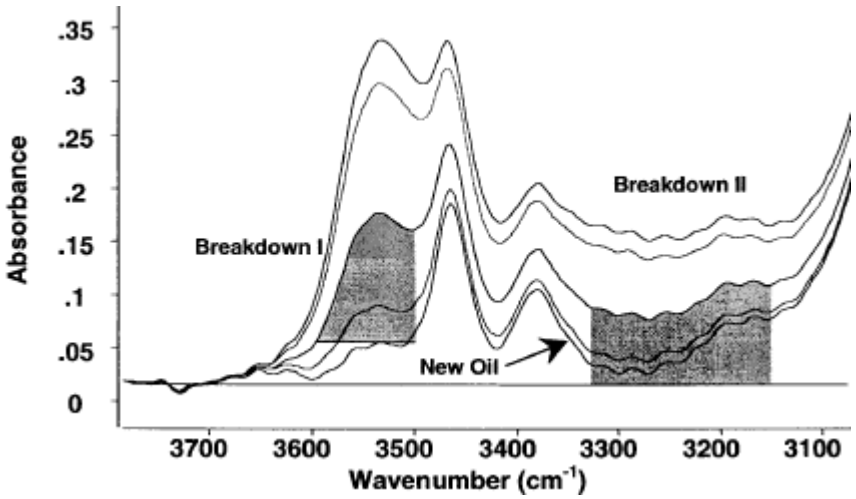

Figure 2.7 Area of interest for breakdown by-products in polyol ester oils.
From reference 69.

Metal contamination from machinery wear is one of the causes of failure for lubrication systems. Elemental spectroscopy such as Atomic Emission Spectroscopy (AES) is an effective technique for measuring the metallic content in lubricant oils[84, 85] . AES determines the wear metal elemental composition from a calibration curve to convert the emission intensity to the element concentration. The two most common excitation source used in atomic emission spectroscopy for oil analysis are the Rotating Disk Electrode (RDE)[85] and the Inductively Coupled Plasma (ICP)[84].

Another method to monitor wear metal contamination in oil is through X-Ray Fluorescence (XRF) spectroscopy. This technique has been applied in portable and benchtop analysers and also for filter debris analysis[86].

Determining the viscosity of the oil before usage and in operation is very important since changes in viscosity are directly related to an oil failure mode. There is a set of ASTM test methods developed for viscosity analysis of different lubricants in different operating temperature conditions[87, 88, 89, 90, 91] . For example, ASTM D445-06 is a test method to determine the lubricant viscosity by measuring the time taken for a given

volume of the oil to flow through a calibrated capillary viscometer under well-defined conditions e.g. gravity and controlled temperature.

Additional test methods were developed to meet specific machinery monitoring requirements and to collect complementary data with great accuracy and high reproducibility. Gas chromatography, coupled with Fourier Transformer Infrared (FTIR) or mass spectrometric detectors, is widely used to detect unexpected hydrocarbon components and specific contaminants in both new and in-service machinery fluids[92, 93]. According to ASTM instructions, gas chromatography is a perfect tool to determine the concentrations of diesel fuel and traces of glycol in motor oils. The Glycol Based Antifreeze test[94], Karl Fisher Titration (KFT)[95] and Antioxidant Condition by RULER[96, 97] are three other examples of supplemental tests. The first technique measures the glycol concentration in petroleum engine oils calorimetrically then the glycol is extracted and oxidized. In the KFT test method, the Karl Fischer reagent is used to detect water contamination through potentiometric titration of, typically, hydraulic and steam turbine oils. The Antioxidant Condition by RULER test is used to determine the remaining useful life of machinery lubricants. The RULER is an instrument that utilizes voltammetric measurements and quantifies the relative concentrations of antioxidants in oil. The collected data can then be used to calculate the depletion rate of antioxidants in the oil and to estimate the remaining useful life of the oil.

Of some importance in this thesis is the Rancimat method, which determines the oxidation stability and useful lifetime of the oil[98]. Rancimat is the name of the instrument and also of the technique that is used to measure the induction time or oxidation stability index of oil. Details of the Rancimat method and device will be explained in the next

chapter. Briefly, in this method, the induction period of oil is measured as an indicator for oxidation stability. During the measurement, an oil sample in a sealed vessel is heated while exposed to flowing air. This treatment results in oxidation of the oil molecules, and the formation of oxidation products including volatile organic acids. These compounds are transported into a container containing distilled water where the conductivity is recorded in real-time. Once the antioxidants fail to protect the oil, volatile organic acids are formed and are transferred into the water. The onset of oil oxidation can be detected as a sharp increase in the water conductance. The time that passes from the beginning of the experiment to the appearance of these oxidation products is known as the induction time[99].

In summary, the presence of abrasive particles, solid or liquid contamination and any breakdown in the oil is likely to change its lubricity. Unfortunately, lubricity of a material is not a physical observable property and therefore cannot be directly measured. Instead, as discussed above, various parameters have been tested and knowledge has been created to quantify the lubricants' performance. Such parameters include chemical composition of lubricants, records of the machine's performance over the lubricant's lifetime, comparison of FTIR absorption spectra of different lubricants over their lifetimes vs. concentrations of various contaminants, and so on. Most of these parameters are either impractical for the implementation in regular real-time, online monitoring of lubricant condition, or not selective enough to identify and quantify changes and, eventually lubricity. In short, there seems to be no identified integrated parameter that could be representatively used for comprehensive characterization of a lubricant state and its dynamics.

Viscosity should be a good parameter to characterize lubricity quantitatively. In general, lubricating oils function properly as long as their viscosity is stable and stays within the boundaries governed by the operating temperatures of the machine. It is then reasonable to use changes in viscosity as an indicator of changes in the lubricant condition. However, the industry paradigm is such that the market does not wish to implement direct viscosity-measurements sensors. The most probable reasons for this could be:

- Viscosity is not a clearly defined physical variable that could be uniquely and reproducibly applied in different cases; aside from different (and related) definitions for kinematic, dynamic and bulk viscosity, the value obtained for the viscosity measurement also somewhat depends on the measurement techniques. In addition, viscosity strongly depends on the fluids' working condition, fluid type, and temperature.
- Viscosity, regardless of the definition, is an integrated parameter. It does not reveal any details on the physical or chemical processes that are responsible for the lubricity changes. Basically, it does not characterize what kind of changes happen to molecular species in the lubricant.
- Existing online viscosity meters are not sensitive enough to detect viscosity changes due to potentially worrisome oil degradation and distinguish them from those introduced, for example, by temperature changes.

Understanding the underlying causes of changes in the machinery lubricant health is essential to confidently detect lubricant damage at an early stage. This requires obtaining chemical analytical information. Arguably, the best tool to obtain analytical

information in real-time is spectroscopy. This study focuses on using fluorescence spectroscopic signatures as representative indicators of changes in the structure and composition of lubricating oils, as well as the oxidation breakdown effects on molecular structures of oxidation inhibitors. To obtain accurate and quantitative information, and to be immune to interfering signals, Excitation Emission Matrix Spectroscopy (EEMS) was selected as a measurement technique. This technique has been specifically proposed with the purpose of increasing selectivity of the real-time analytical sensing.

Our studies aim at enabling developments of commercial sensors for the real-time machinery oil condition monitoring. There are a few types of real-time / online sensors currently available on the market to deal with the oil contamination and degradation issues. The majority of those are based on measuring changes in the oil electrical properties such as impedance (SmartMon, Impact Technologies), which cannot provide chemical analytical information on complex, multi-component substances. Recently, spectroscopic sensors such as miniature Electron Spin Resonance (ESR, Micro-ESR Oil Analyzer, Active Spectrum) and compact Infra-Red (IR) direct absorption (R-Oil condition sensor, Comline Elektronik Elektrotechnik GmbH) spectrometers have been introduced into R&D on the real-time oil condition monitoring. Those methods are not yet sensitive and selective enough to quantitatively characterize transformation processes in machinery liquids in real time. In addition many devices measure quantities that are only weakly correlated to the lubricity and useful lifetime of the oil. None has achieved a large market penetration.

2.4 Excitation Emission Matrix Spectroscopy as an Oil Tracking Tool

Fluorescence techniques have been used for the detection of oil spills in natural environments since at least the 1980s[100]. The fact that the chemical complexity of oil and petroleum products leads to broad fluorescence spectra without a fine-structure (at single wavelength excitation) is the main reason for using EEMS for oil spill determination. The fluorescence of the natural Dissolved Organic Matter (DOM) interferes with the detection of oil pollution in water and soil when using single line excitation fluorescence spectroscopy, while EEMS would be able to resolve the two fluorophore groups [101]. In addition three dimensional EEM fingerprints allow for an objective comparison of fluorescence spectra of spill samples with those from suspected sources[102].

Environmental damage related to oil spills is becoming a major concern that accompanies the vastly increased volumes of oil moved across the globe. Many polycyclic aromatic hydrocarbons (PAHs), which occur in oil and petroleum products have been identified as carcinogenic and mutagenic compounds. EEMS has been used as a successful tracking tool for PAHs pollutants and their sources[103, 104] as well as determining the oil type[102]. Yu et al. used three dimensional (3D) fluorescence spectroscopy to analyze commercial oil samples of five oil types (heavy diesel, crude oil, diesel, gasoline, and lubricant)[105]. Using EEMS lets them classify and distinguish all five oil types in weathered samples. EEMS has also been utilized to identify organic compounds and spilled oil in seawater[106, 49]. Bugden et al. have evaluated the effectiveness of chemical dispersants on oil spilled in seawater via the EEM fingerprint of the dispersed oil[107]. The presence of PAHs in natural water has also been identified

with 3D fluorescence technique using solvents such as methanol and dichloromethane[108, 39]. Dudelzak et al. applied EEMS directly to sea water samples, with no sample pre-treatment, for the investigation of oil pollution[101].

Unfortunately, accidental oil spills in marine and other natural environments occur frequently. EEMS was shown as a suitable method for oil characterization as it assists in determining the oil source[39]. In this oil matching study, PARAFAC analysis was applied to the EEMs collected from samples of different oil types and also to the EEMs of individual PAHs commonly present in different oils. PARAFAC components were characterized as a single PAH or as a mixture of a few and a reference library was constructed for comparison. Later, Alostaz et al. used a similar process to identify petroleum products (natural gas condensate, gasoline, diesel, flare pit residue and heavy crude oil) as environmental contaminants[109].

Recently, crude oil degradation in the water column was investigated using EEMS together with UV-vis absorption spectroscopy, Gas Chromatography - Flame Ionization Detector (GC-FID) and GC-MS[110]. The collected EEM spectra and PARAFAC results could be used to track the changes of PAHs present in Mocondo crude oil during laboratory degradation. The degradation process was completed at a low temperature of 30 ºC, while the oil was diluted and dispersed in the water, similar to actual environmental conditions.

Regarding the oil degradation study, most previous works utilized IR spectroscopy to track the changes in the concentration of carboxylic acids[111] , sludge and deposits[112] as oxidation products or to monitor the aminic antioxidant depletion[113]. In the following chapter, chapter 3, oil degradation at high temperature, mimicking engine

conditions, is presented as well as direct fluorescence measurements of neat oil. To avoid fluorescence quenching and inner filter effects, one may use diluted oil samples for fluorescence spectroscopy and EEMS. Instead, we use a bifurcated fiber probe to limit the effect of inner filter on the collected fluorescence intensity and thereby avoid sample dilution and preparation. While fluorescence quenching may still be present, the fluorescence signal in this “front face” configuration was experimentally found to be more than adequate for our analysis. A thorough theoretical analysis of the fiber probe in its different configurations is presented in chapter 4.

3 Chapter 3. Studies on Oil Degradation[*]

3.1 General Overview of the Experimental Work

The ultimate goal of the work is a robust sensor system that contains a probe submersed permanently in the lubricant oil sump and a continuous read-out system.

In this study, we use fluorescence excitation emission matrix (EEM) spectroscopy to characterize antioxidant performance as a polyol ester based aviation lubricant oil is degraded by oxidation at elevated temperatures.

Fortunately, synthetic lubricant oils, such as the polyol ester base stock used in this study, but also silicone oils, do not exhibit strong fluorescence when excited in the 220-450 nm region, whereas the polycyclic aromatic compounds (PACs) that are added as antioxidants show fluorescence. As will be shown, their fluorescence signatures can be correlated to the established lubricant assessment methods such as breakdown number (BDN) measurements and the Rancimat procedure.

To investigate aviation lubricant oil deterioration, a laboratory bench simulation test has been developed. The lubricant oil was heated to temperatures that are typical in an aircraft turbine engine (150-220° C). We also collected oil samples that had been degraded during aircraft engine operation. All lab and field samples were studied using fiber-coupled EEMS followed by chemometric data analysis using the parallel factor (PARAFAC) method.

[*] [Omrani, H.; Dudelzak, A. E.; Hollebone, B. P.; Loock, H.-P., Assessment of the oxidative stability of lubricant oil using fiber-coupled fluorescence excitation–emission matrix spectroscopy. *Analytica Chimica Acta* 2014, *811*, 1-12.] http://www.sciencedirect.com/science/article/pii/S0003267013013275.

3.2 Experimental Set-up / Materials and Methods

3.2.1 Chemometric Analysis / PARAFAC

As was discussed in chapter 1, EEM spectra contain quantitative analytical information which is multivariate in nature. Chemometric techniques are typically used for such multivariate data treatment. Parallel Factor Analysis (PARAFAC) is a multi-way chemometrics model which can also be applied to interpret the EEM data[44, 114]. PARAFAC is less robust but has the advantage that the components' EEM signatures can sometimes be related to chemical constituents, especially when a small number of distinct species contribute to a composite EEM spectrum as is the case in this study. Stacking 2-dimensional EEM spectra from a series of samples creates a data cube that can be mathematically decomposed into a set of trilinear components and then modeled by PARAFAC in a matrix equation;

$$X_{ijk} = \sum_{f=1}^{F} A_{if} B_{jf} C_{kf} + E_{ijk} \qquad (3.1)$$

where X is the fluorescence intensity of sample k at the excitation wavelength i and the emission wavelength j. F is the number of unique spectral profiles ("components") found in the data cube. The columns of the A, B, and C matrices are the estimates of the pure excitation, emission, and concentration profiles, respectively, and E_{ijk} is the residual error matrix when the model has been fitted to the collected data[115]. Here, we performed a multivariate analysis of the 21 EEM spectra from jet turbine oil

which was oxidized in the lab as well as 56 EEM spectra of field samples and 30 samples of aged silicone-oil/PAN mixtures. The PARAFAC model has been used to analyze the data and was implemented with *Matlab* software (version 7.10.0) using the N-way toolbox [116] and DOMFluor toolbox[117] .

3.2.2 Sample Preparation and Fluorescence Spectroscopy

Commercially available jet turbine oil (NYCO, jet turbine oil, MIL-PRF-23699 F Class STD) was examined for the oil degradation studies. The oil is based on polyol ester base stock and has a viscosity of 5 cSt at 100ºC. Fresh and used oil samples were analysed. Some of the lubricant samples were degraded in-house using a 1L round bottom flask in a heated silicone oil bath. Additional samples were supplied by GasTOPS and have been obtained at oil change times from the main rotor engine (BCA Engine Turbo Shaft T58-GE) of a Sikorsky Sea King helicopter.

The degradation of lubricant oil was studied by heating 800 ml of oil at 195°C for 66 hours in a simple apparatus consisting of a round bottom flask containing jet turbine oil and a thermostatically controlled silicone oil bath. The oil was subjected to an air flow, bubbled, of 1.0 L/min. 21 samples, of 30 ml each, were taken according to a logarithmic time scale plan.

The EEM spectra were measured using a spectrofluorometer (Varian, Cary Eclipse) in “scan mode”. The voltage of the inbuilt photomultiplier tube (PMT, high performance R928 photomultiplier, 185 nm to 900 nm) fluorescence detector was set to

850 V. A total of 46 scans were obtained at excitation wavelengths ranging from 230 to 450 nm with 5 nm increment, each consisting of 550 emission wavelengths from 250 to 700 nm with 1 nm increment. The bandwidths were 5 nm for both excitation and emission, and the scan rate was set at 21 nm s^{-1}, which resulted in 20 minutes of data acquisition time for each two-dimensional EEM spectrum. The sample preparation and analysis were then repeated for fresh oil samples heated to 150 °C and 215 °C.

In preliminary experiments, the fluorescence light from two different cuvettes was collected at a 90̊ angle to the excitation from a xenon lamp. A bifurcated fiber bundle capable of collecting fluorescence signal at close angle to the excitation light, was designed and prepared. Briefly, 6 fibers (400/440 μm) were used to illuminate the sample and fluorescence was collected using 13 identical fibers, Figure 3.1.

Scattering contributions were eliminated from all EEM spectra by manually discarding the measurements for which $\lambda_{exc} = \lambda_{em} \pm 7$ nm.

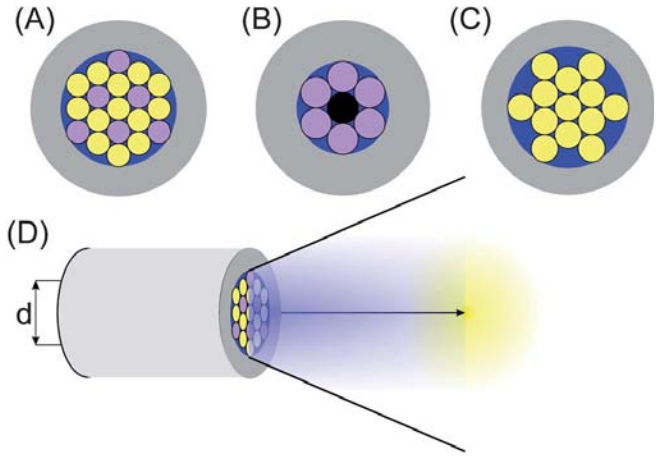

Figure 3.1 Sketch of the bifurcated fiber bundle used for EEM experiments.
Top row: (A) fiber end immersed in sample, light is guided into the sample through 6 fiber ends (purple) and is collected by 13 fiber ends (yellow). (B) Fiber bundle in front of the light source. (C) Fiber bundle in front of the detector. Each fiber has a 400 μm core and a 440 μm cladding and the diameter of the fiber bundle (shown in (D)) is about d = 2.2 mm.

3.2.3 Characterization of the Fiber Optic Probe

Lubricant oil can become opaque after a few hours of operation near 200 °C. The inner filter effect, *i.e.* absorption of excitation light and re-absorption of fluorescence, can then severely restrict the dynamic range of the spectroscopic measurements. For opaque samples front-face fluorescence detection is the most appropriate detection configuration[118].

To characterize the influence of inner filter effects, fresh lubricant oil (MIL-PRF-23699) was analysed either neat or dissolved in hexane (0.1%, 1000 ppm_v). The samples were placed in either a 10×10 mm cuvette or in a 10×1 mm cuvette and fluorescence was collected at right angles, resulting in Figure 3.2.

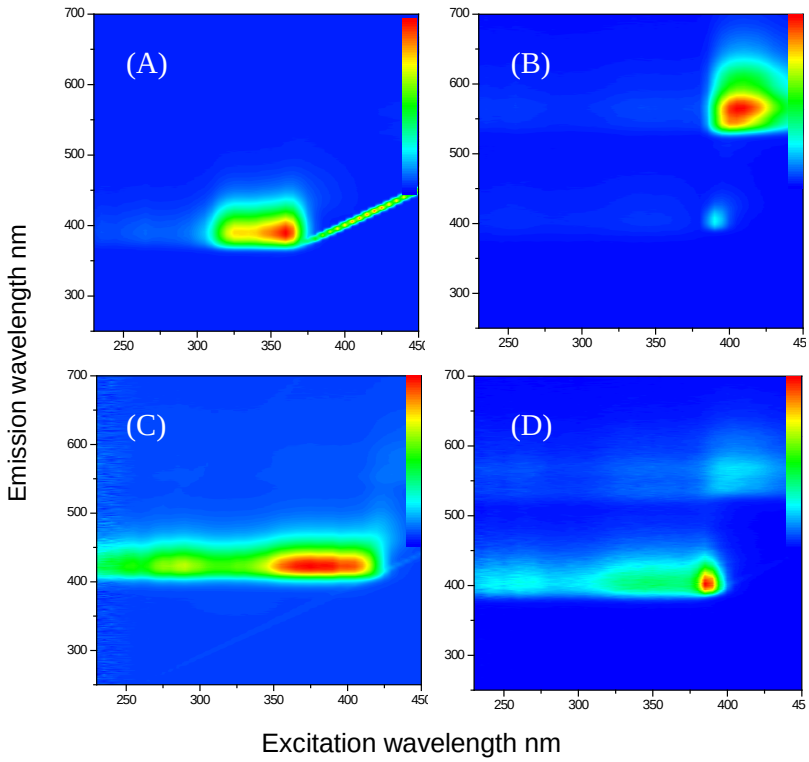

Figure 3.2 EEM spectra of jet turbine lubricant.
(A) fresh lubricant oil diluted in hexane, (B) neat oil in 10×10 mm cuvette, (C) neat oil in 10×1 mm cuvette, and (D) neat oil collected with bifurcated fiber probe.

The spectra show two fluorescence EEM features, *i.e.* one emission peak at 400 nm associated with excitation around 360 nm and a second emission feature around 560 nm associated with excitation near 420 nm. The first feature is observable in diluted oil and in neat oil when the emission path is reduced to one millimeter, but is only faintly observable in the neat sample when using a 10×10 mm cuvette. We attribute this observation to the re-absorption of the 400 nm emission by the neat oil.

On the other hand, a previously undetected and broad fluorescence band around $420^{exc}/560^{em}$ nm is apparent only in the neat oil. It is caused by a weaker absorption at 420 nm and fluoresces in a wavelength range at which the oil is largely transparent. Since the $420^{exc}/560^{em}$ nm absorption and emission is rather weak, this fluorescence feature is not visible in cuvettes with reduced emission path length and in the diluted sample.

In chapter 3.3.1 we identify the fluorescence feature at $360^{exc}/400^{em}$ as arising from the antioxidant phenyl-α-naphtylamine (PAN) and the feature at $420^{exc}/560^{em}$ as another - as yet unidentified - antioxidant additive (possibly PAN-oligomers)

To address the problem of re-absorption of the fluorescence (secondary absorption) we propose to collect the fluorescence at angles close to the excitation direction, *i.e.* near normal incidence. As mentioned before, a strong absorption feature then causes fluorescence at short penetration depths and the - presumably strong - fluorescence will interact only over this limited path within the sample. A weak absorption feature causes the sample to fluoresce in a much larger excitation volume and the fluorescence will interact with the sample over a much longer re-absorption path. In the special, but common case of monotonously decaying absorption from the UV to visible wavelength, counter-propagating fluorescence detection is expected to approximately compensate for re-absorption. The theory behind this will be explained in detail in chapter 4 as well as fluorescence intensity calculations and the comparison of experimental measurements.

To permit in-line detection, we designed a bifurcated fiber bundle for collecting all weak and strong fluorescence light from the sample while the end of the probe is immersed in the sample material. The spectrofluorometer was coupled to a bifurcated optical fiber bundle, which contains 19 multimode fibers (core / cladding diameters: 400/440 μm, CeramOptec); 6 of these fibers were used to deliver excitation light from the xenon lamp to the sample and 13 fibers collected and guided the fluorescence emission from the sample to the dispersion element and the photomultiplier detector. Figure 3.3. shows a picture of the spectrofluorometer coupled to the fibre bundle.

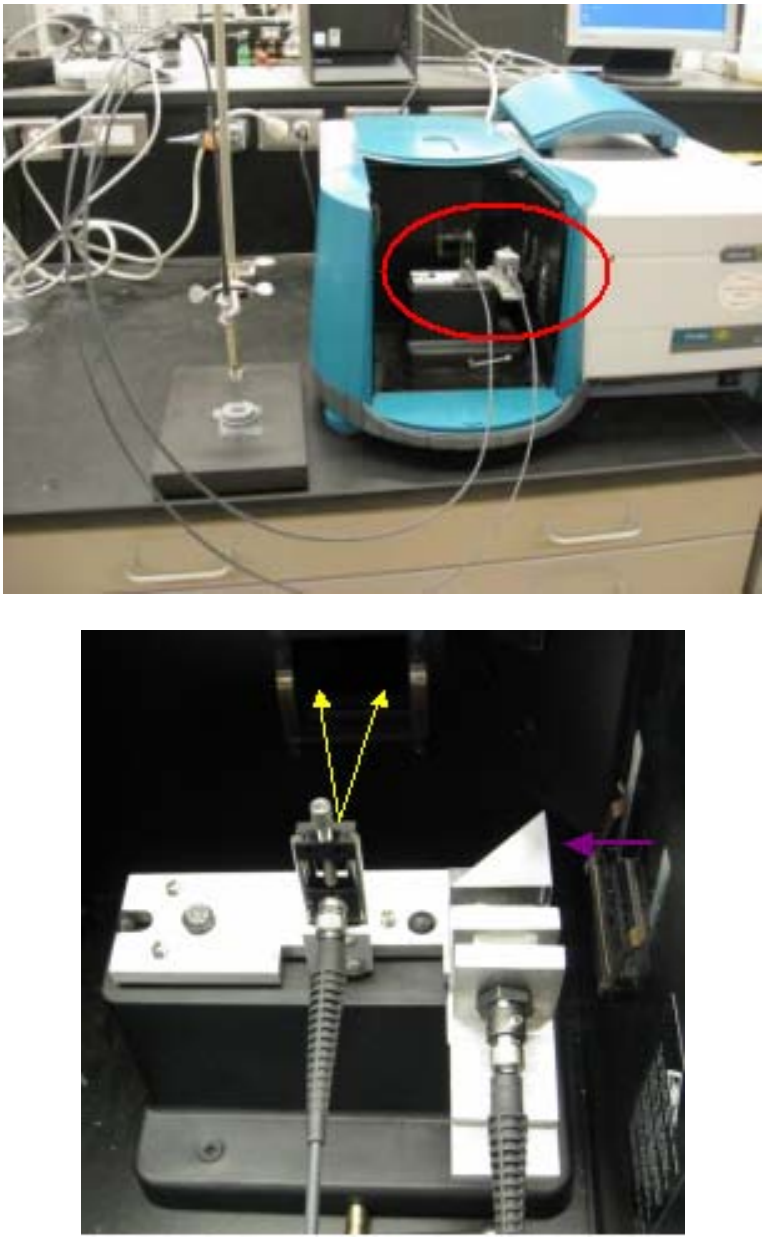

Figure 3.3 Varian spectrofluorometer.
(Top) Varian spectrofluorometer is equipped with fiber bundle. (Bottom) The incident light from the source, a xenon lamp, is directed to the probe end holding six fiber ends, excitation fibers, and guided to the sample through theses fibers. The produced emission light is guided to the detector through the rest 13 fibers which are held together by the third probe end.

While true in-line detection (submersing the fiber bundle in the heated oil) was feasible, we also required independent measurements of the breakdown number by FTIR spectroscopy and therefore had to withdraw samples. The heating processes, withdrawing

samples and collecting EEMs of each sample were conducted at 150° C, 195° C and 215° C. Figure 3.4 shows a photograph of the samples taken at different time intervals after heating in 195°C.

Figure 3.4 Photo of samples taken at different times when oil was heated to 195° C.
From left: fresh turbine oil, and samples taken at the same intervals as described in Figure 3.6.

3.2.4 Detection of the Formation of Volatile Acids Using the Rancimat Method

The Rancimat experiments were performed at elevated temperatures (150° C, 195° C, 205° C, and 215° C) on jet turbine oil. The Rancimat instrument (892, *Metrohm*) contains two heating blocks, which can be heated independently, and each has four channels, Figure 3.5. Before each experiment, all parts were cleaned carefully to avoid any contamination from previous experiments. For each temperature, the vessel containing 5 ml oil was immersed into the heating block once the temperature of the block became stable. The air stream (adjusted to 10 L h^{-1}) was first bubbling through the oil and then through a container containing 60 mL distilled water. The conductivity of the distilled water was continuously recorded. To assure reproducibility, the experiments were carried out simultaneously either in four channels in the same block (4 × 1), or in

two channels in each of the two blocks (2 × 2). The differences between conductivity-time curves that were obtained at identical temperatures were found to be negligible.

Figure 3.5 Rancimat instrument (892, *Metrohm*).

3.3 Experimental Results

3.3.1 PARAFAC Analysis on EEM Signatures of Jet Turbine Oil Samples Degraded in the Lab

Figure 3.6 shows 20 out of the total 21 fluorescence EEM spectra taken at different time intervals from the oil sample artificially degraded at 195° C. A continuous evolution of the EEM spectrum is apparent and may be described by a rapid decrease of the initially strong peak at $370^{exc}/400^{em}$ nm, an increase and decay of the feature at $400^{exc}/450^{em}$ nm and a more gradual decay of a weaker feature at $420^{exc}/580^{em}$ nm. All 21 EEM spectra can be fitted well using only 3 PARAFAC components (Table 3.1).

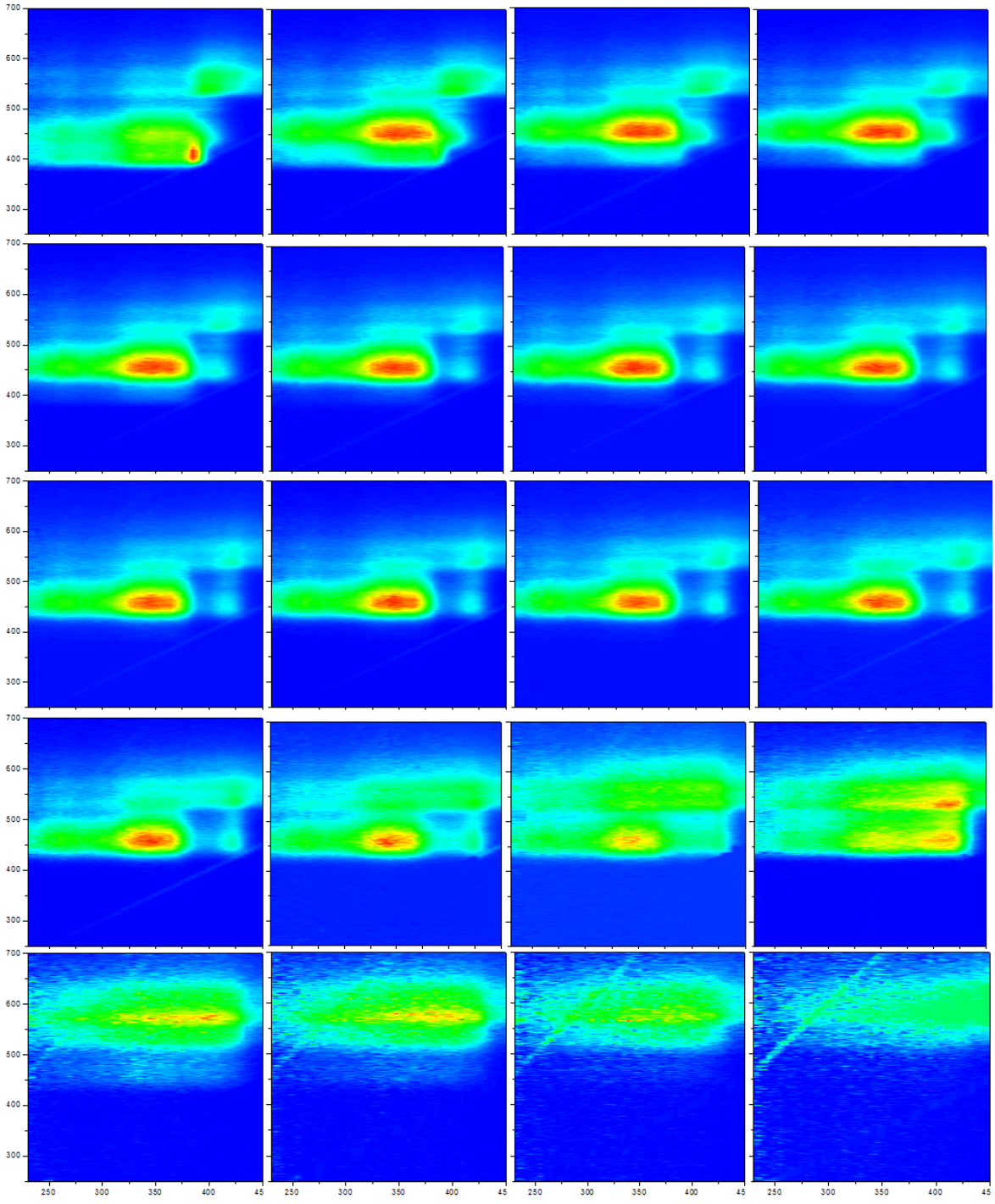

Figure 3.6 EEM signatures of heated oil samples taken at different times, from left to right.
First row: 10, 20, 30 and 40 min. Second row: 50, 75, 90 and 105 min. Third row: 120, 135, 155 and 180 min. Forth row: 240, 360, 510 and 690 min. Fifth row: 1440, 2160, 2880 and 3960 min.

CORCONDIA/RELFIT	1Component	2Components	3 Components	4 Components
Aged oil in lab	100%/80.7%	99.6%/91.8%	92.9%/98.3%	54%/98.6%
Field samples	100%/85.5%	96.7%/91.2%	89.4%/98.3%	13.2%/97.8%
Si-oil/Pan	100%/83%	99.4%/98.2%	85.8%/98.4%	96.3%/99.0%

Table 3.1 PARAFAC diagnostic parameters to assess the quality of the fit.
Core consistency diagnostic (CORCONDIA) and the percentage of explained fit variation (RELFIT)[50].

The EEM spectra of the three components are shown in Figure 3.7 and their integrated excitation and emission spectra are shown in Figure 3.8.

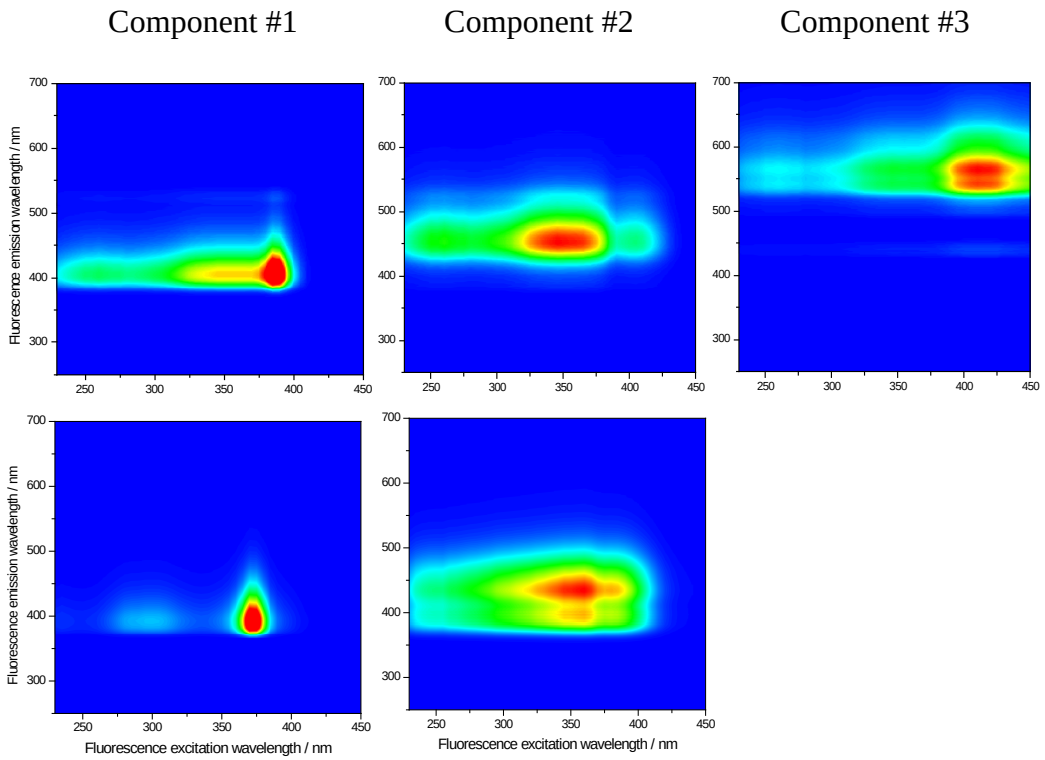

Figure 3.7 EEM spectra of PARAFAC components.
Top row: EEM spectra of the three components associated with the PARAFAC decomposition of the spectra of 21 jet turbine oil samples that were aged at 195°C in the lab (shown in Figure 3.6). The PARAFAC component spectra were then applied to the field-aged sample EEM spectra. Bottom row: PARAFAC components 1 and 2 obtained by analysis of the spectra of PAN in silicone oil at 195° C in the lab see Figure 3.13.

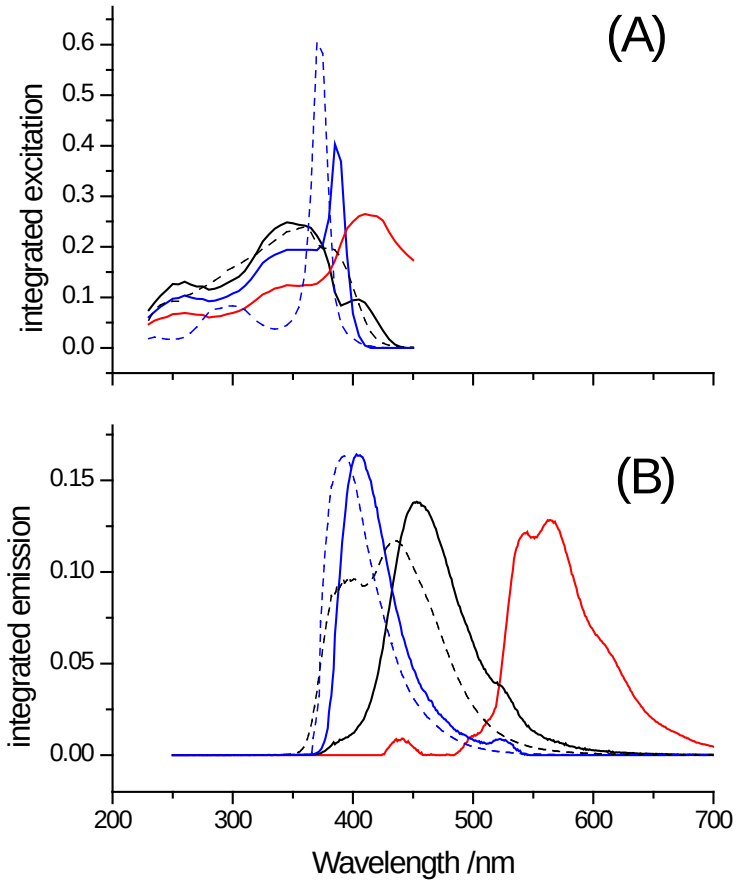

Figure 3.8 Excitation and emission profiles of PARAFAC components.
(A) Excitation and (B) associated emission spectra of the three components from PARAFAC analysis (blue: component 1, black: component 2 and red: component 3). The solid lines are obtained from the PARAFAC analysis of the combined lab-aged samples and field-aged samples, whereas the dashed lines were obtained by analysis of the aged samples of a PAN mixture in silicone oil.

Figure 3.9 presents the change of the PARAFAC scores as the jet turbine oil is aged at three different temperatures. It is apparent that the scores of component 1 decreases with time while component 2, presumably related to the primary oxidization products, increases.

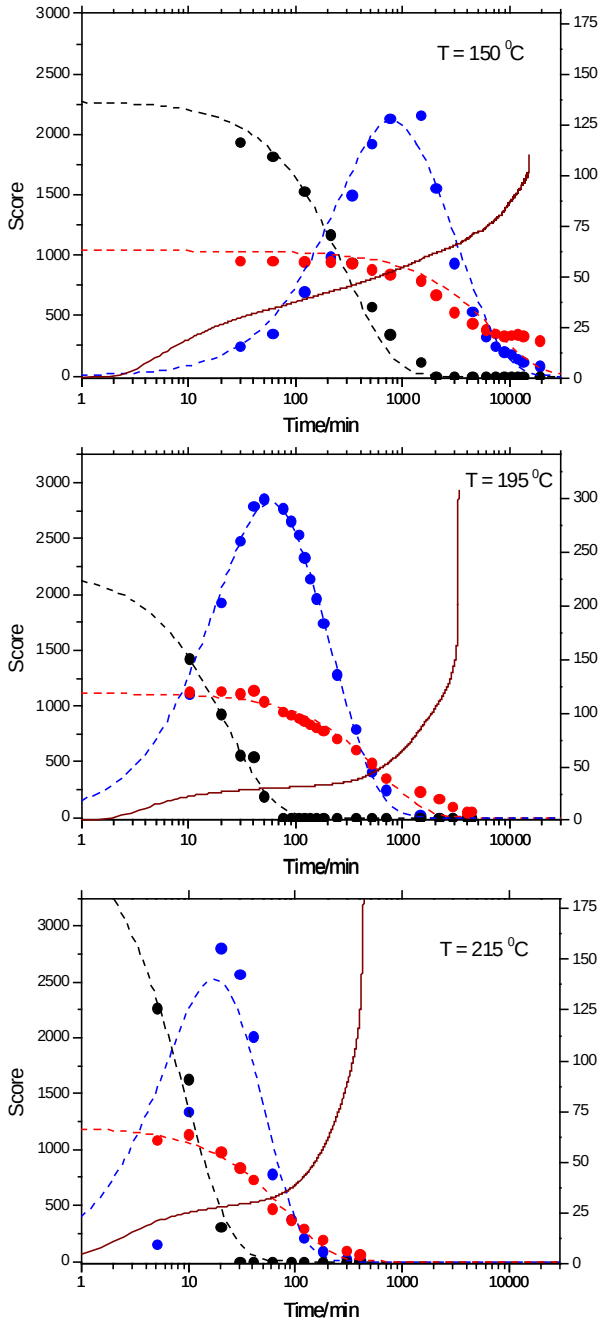

Figure 3.9 Time evolution of the three PARAFAC components and corresponding Rancimat data.
Time evolution of the three PARAFAC components (black: component 1; blue: component 2 and red: component 3) at three different temperatures as indicated. The dashed lines are obtained by fitting the data to the kinetic models describe in section 3.4.2 and the solid brown line corresponds to the conductivity obtained independently using the Rancimat apparatus.

At about the same time that this primary reaction product decomposes, we also observe the decay of the third EEM component, which previously had not experienced a

significant intensity change. The main fluorescence features of fresh oil can therefore be attributed to a sum of components 1 and 3. The experiments were repeated at 150° C, 195° C and 215° C and a separate PARAFAC analysis was carried out for each of the three data sets. The respective PARAFAC components at T = 150° C, and 215° C were found to be very similar to those shown for T = 195° C in Figure 3.7 and Figure 3.8.

As is discussed in section 3.3.3, we can attribute the three PARAFAC components to fluorescent antioxidants, where component 1 and 3 correspond to primary antioxidants that are used complementarily, while component 2 can be identified as a reaction product of component 1, which itself is not stable to oxidation.[1] To test this hypothesis, we attempted a mass spectrometric analysis, GC-MS, of fresh and degraded samples, but in the rather complex mixture present in commercial lubricant, we were not able to identify any of the more common antioxidants (listed in chapter 2.2.4), conclusively. Instead, we rely on fluorescence analysis to identify component 1 as phenyl-α-naphtylamine (PAN) and component 2 as the PAN dimer. Further confirmation of our hypothesis is obtained in a series of experiments on PAN-containing silicone oil (section 3.3.3 and 3.4.1).

One may suspect that the decrease in detected fluorescence intensity for all three components is caused by the greatly reduced attenuation length in the opaque ("black") used oil samples (see Figure 3.4), instead of the decrease in fluorophore concentration[118]. We therefore used the method of "standard additions" [16] and spiked a fresh oil sample and a heated oil sample (3960 min of heating at 195° C) with 2000 and 4000 ppm_v of the

[1] We were not able to identify component 3 as a single lubricant additive, but considering the similarity of the EEM component spectrum to that of PAN and PAN_2 it is plausible that component 3 is in fact a mixture of PAN oligomers with different masses. This speculation is also supported by the fact that the fluorescence emission peak (the red line in Figure 3.8B) shows multiple maxima and shoulders.

antioxidant PAN. In Figure 3.10 the respective increases in PARAFAC scores of component 1 are shown. In both cases, we observe an increase of the score - by 0.21±0.05 scores/ppm$_v$ for the fresh oil and 0.28±0.05 scores/ppm$_v$ for the heated oil. This is indicative that the reduced attenuation length does not influence the decrease in the PARAFAC scores, which is observed upon heating the oil. The decrease of detected fluorescence is indeed due to a decreasing fluorophore concentration. The spiking experiment also lets us estimate the concentration of PAN in fresh oil as 0.6% to 0.8%.

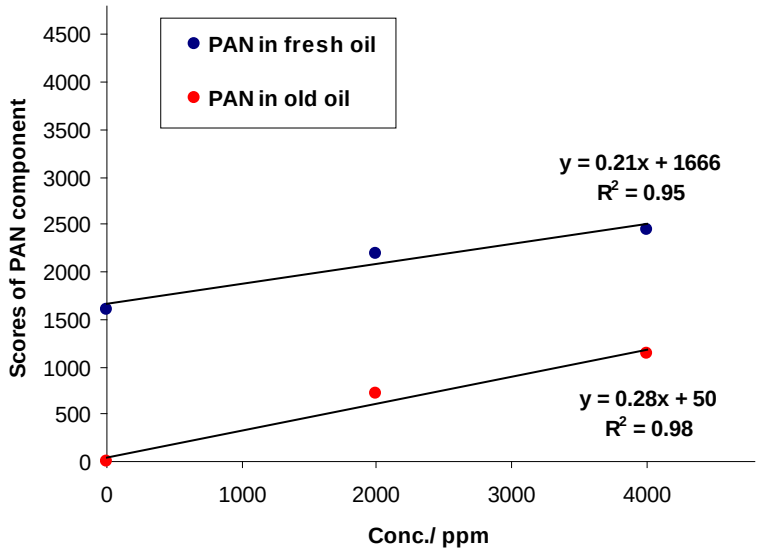

Figure 3.10 Linear correlation between PAN component scores and related spiked concentration in fresh and degraded oil samples.

3.3.2 PARAFAC Analysis of Jet Turbine Oil Samples Aged in Jet Engines

Several jet turbine lubricant oil samples, collected at oil change time with different, and somewhat ill-specified, hours of operation were examined by EEM

spectroscopy and interpreted using PARAFAC analysis. Only the lab samples from the previous section 3.3.1 were used in the calibration set, while all the field samples were placed in the prediction set. To determine the breakdown numbers, FTIR measurements from 3595 cm^{-1} to 3500 cm^{-1} were completed on all lab and field samples according to the ASTM protocol[71]. Determination of the breakdown number I (BDN) was performed at GasTOPS' laboratory.

Inspection of the EEM signatures and the calculation of core consistency and residual signal showed that a three-component model again provides the best fit to the field samples. The PARAFAC analysis also shows that the relative scores of the three components change with time (Figure 3.11), however in contrast to Figure 3.9 the correlation is rather weak.

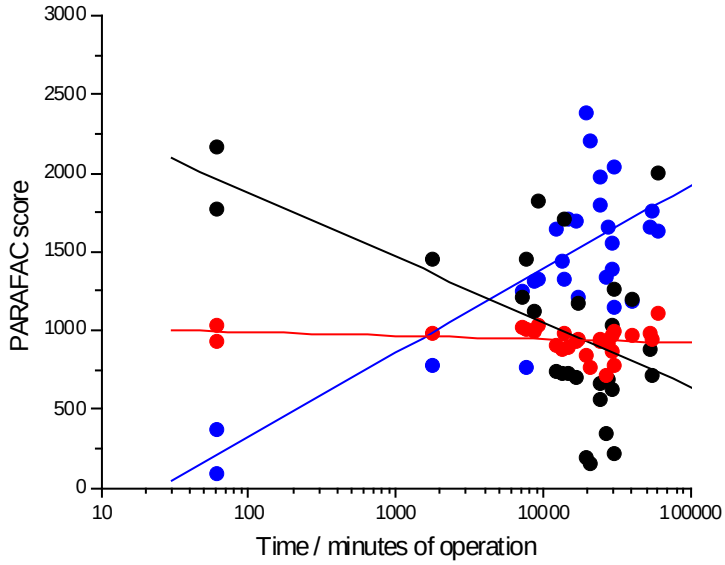

Figure 3.11 Time evolution of the three PARAFAC components of the jet turbine oil when operated in an engine.
Black: component 1; blue: component 2 and red: component 3. The lubricant was collected at a time that corresponded to the oil change interval. The lines are linear fits to help guide the eye.

This was expected, since most samples were taken after a predetermined oil change time interval, when the lubricant had still retained much of its function. The lubricants have therefore aged a similar and short amount of time in the engine. Of course, engine oil that was oxidized for a specified period of time was not continuously operated at high temperature for the entire time, i.e. the “time of operation” is not identical to the time that the lubricant was exposed to high temperature. Also, it is notable that the scatter associated with the measurement of the scores is comparable to the change during the aging process. However, a weak correlation is apparent: component 1 decreases with time while component 2 increases. Component 3 has remained largely unchanged with PARAFAC scores between 600 and 1200, which is also shown in Figure 3.12 below. This figure is discussed in section 3.3.4 below.

The time evolution of the components in the field samples (Figure 3.11) is therefore consistent with the behaviour of the lab samples shown in Figure 3.9. The weakness of the correlation of PARAFAC scores to time of operation may simply indicate that the lubricant of the aircraft engine was changed before a significant chemical change in the lubricant had occurred - as one would hope.

Future work will use the kinetic model described in section 3.4.2 below together with the ratio of the PARAFAC components to identify a lubricity metric that can be used to derive the oxidative stability of the field samples.

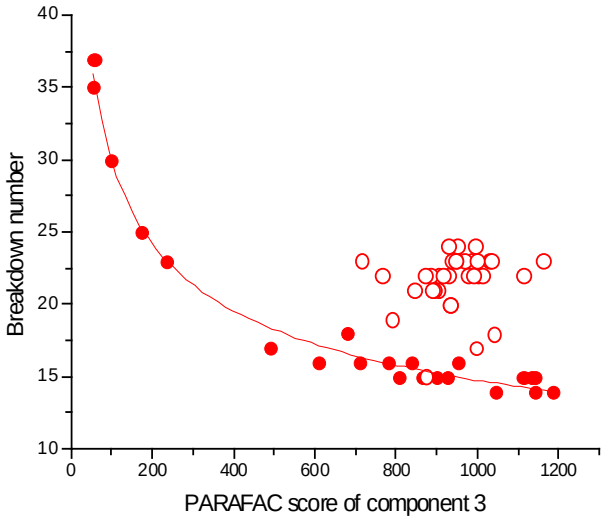

Figure 3.12 The PARAFAC score of component 3 correlates well (R^2 = 0.98) with the independently measured breakdown number.
Solid circles represent this correlation when the oil is aged in the lab under controlled conditions, but the correlation is worse when including the respective measurements of field samples (empty circles). The solid line is a fit to the simple function BDN = 123×(score)$^{-0.3}$ and is meant to be a guide to the eye. The lab samples with high BDN and low PARAFAC score correspond to those which have aged for the longest time.

3.3.3 PARAFAC Analysis of Silicone Oil Base Stock Containing PAN Degraded in Lab

To test whether the fluorescence associated with component 1 could be attributed to phenyl-α-naphtylamine (PAN), we prepared a synthetic "lubricant" consisting of silicone (Si-) oil and 3.29 mmol/L or 623 ppm_v PAN solutions. The Si-oil / PAN mixture was heated to 195 $^{\circ}$C and 30 samples were withdrawn at different times. The EEM spectra of the Si-oil / PAN mixtures (Figure 3.13) can be described as a linear combination of only two component spectra (Figure 3.7 (B) and Figure 3.8 (B)), which change in intensity as the mixture is heated (Figure 3.9). The PARAFAC analysis was not improved when more components were added, leading us to believe that component 1

can be attributed to PAN, and component 2 is produced in the reaction of PAN with oxygen (Figure 3.14). Similar to the jet turbine oil described in the previous sections, we did not observe fluorescence of the base stock.

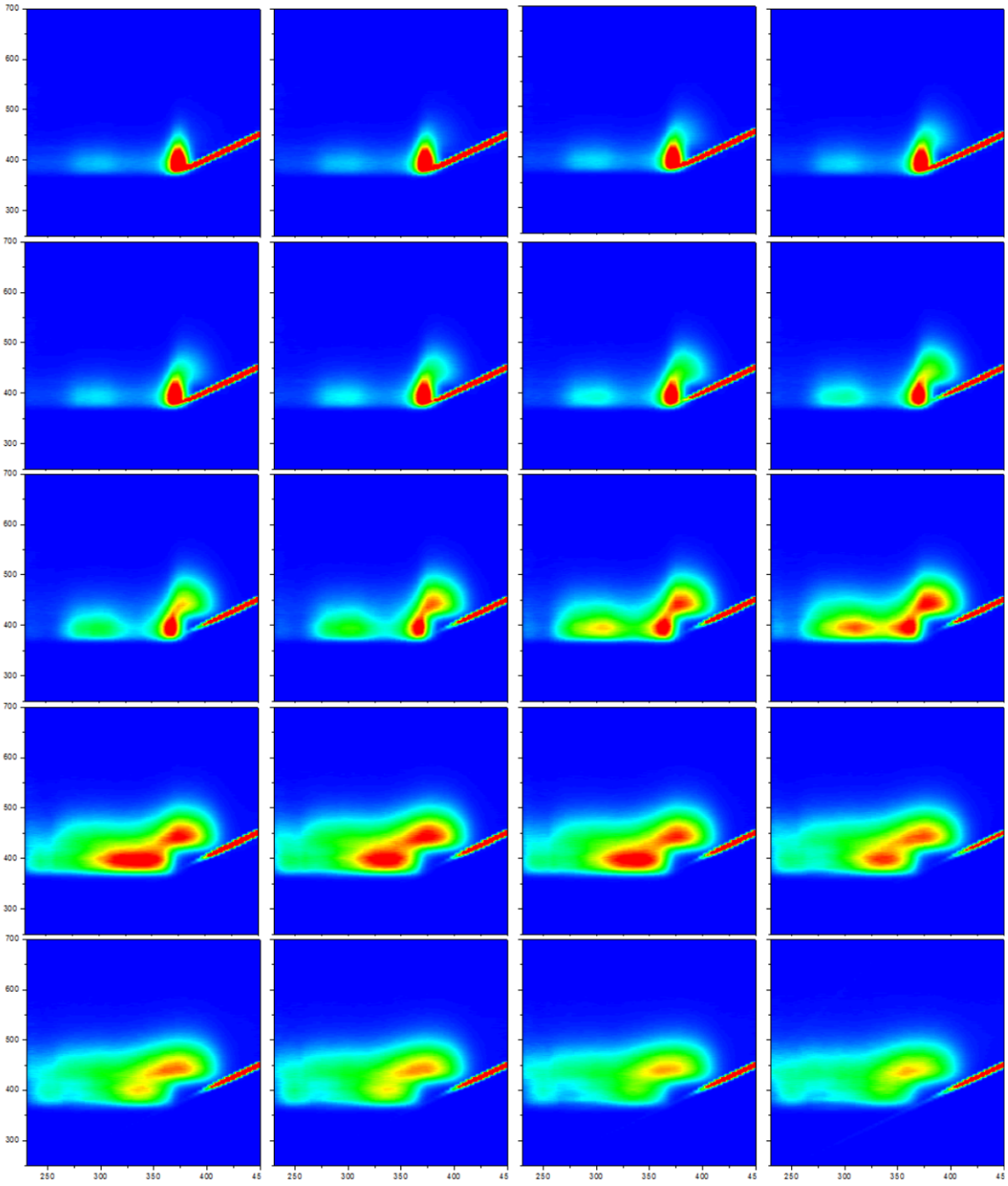

Figure 3.13 20 out of the 30 EEM spectra of silicone oil and PAN (3.29 mmol/L or 623 ppm_v) mixtures taken after different heating times.
From left to right: First row - non heated, 50, 120 and 155 min. Second row: 180, 240, 360 and 540 min. Third row: 810, 1330, 1800 and 2775 min. Forth row: 5775, 7695, 9015 and 11415 min. Fifth row: 13035, 14295, 16275 and 31695 min.

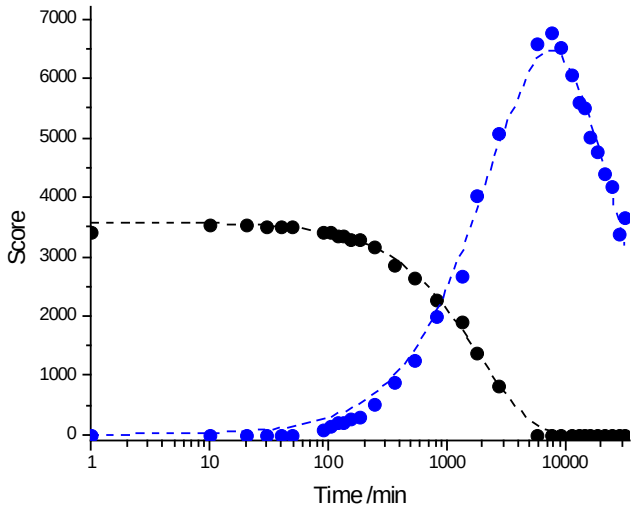

Figure 3.14 Time evolution of the two PARAFAC components of the mixture of PAN in silicone oil. The solid circles are the experimental data (black: component 1; blue: component 2) and the dashed lines are obtained by fitting the data to the kinetic models described in section 3.4.2.

In contrast to the experiments on jet turbine oil the silicone oil base stock did not noticeably degrade or change colour. Since the detected fluorescence of both PARAFAC components nevertheless decreases, this decrease of fluorescence cannot be solely caused by inner filter effects, i.e. by absorption of excitation or fluorescence light. This lends further credibility to the correlation of decreased fluorescence with antioxidant concentration.

3.3.4 Correlation of PARAFAC Analysis to Breakdown Numbers

As mentioned above, we identified the component EEM spectra using the lab-heated samples (Figure 3.7) and then applied this calibration model to, both, the field samples and the lab samples, so that the same component spectra from lab samples were

used on both data sets. Figure 3.12 illustrates the correlation of the scores of the third component of the oil that was aged in the lab and the breakdown number together with a simple, empirical non-linear fit function. Note that in this graph the age of the samples increases towards lower PARAFAC scores and higher breakdown numbers. It is apparent that the breakdown number of the calibration set could be predicted well using the fit equation in the caption of Figure 3.12. While the samples that were aged in the lab show a monotonous trend and a strong correlation, the field samples do not follow this same correlation and show clustering. This indicates that they are approximately at the same, low, degradation level – as would be expected from the discussion in section 3.3.2. We note that all field samples exhibit a breakdown number, BDN, that is higher than may be expected from their time in the engine and from the PARAFAC component analysis. Since BDN are obtained by detecting oxidation products through their respective IR absorption, the samples probably show contamination with very old lubricant that may have accumulated in the engine over a prolonged time.

3.3.5 PCA / PCR analysis of jet turbine oil samples aged in jet engines and correlation of analysis to breakdown numbers

Principal component regression (PCR) is another multi-way calibration method that has been used to analyze the EEMS data collected from field samples. To complete PCR analysis and to build the regression vector, the previously measured breakdown numbers were used as oil degradation indicator. As previously was explained in chapter

1, Principal Component Analysis (PCA) was primarily applied to minimize the calibration data set dimensions and simplify the process of model building.

Since the collected EEM data is arranged in a 3D-matrix, the data cube has to be first "unfolded" so that we can apply PCA[43, 119]. The unfolding process is actually the re-arrangement of the data cube in a 2D-matrix by spreading one of the spectral modes (mode "c" in Figure 3.15).

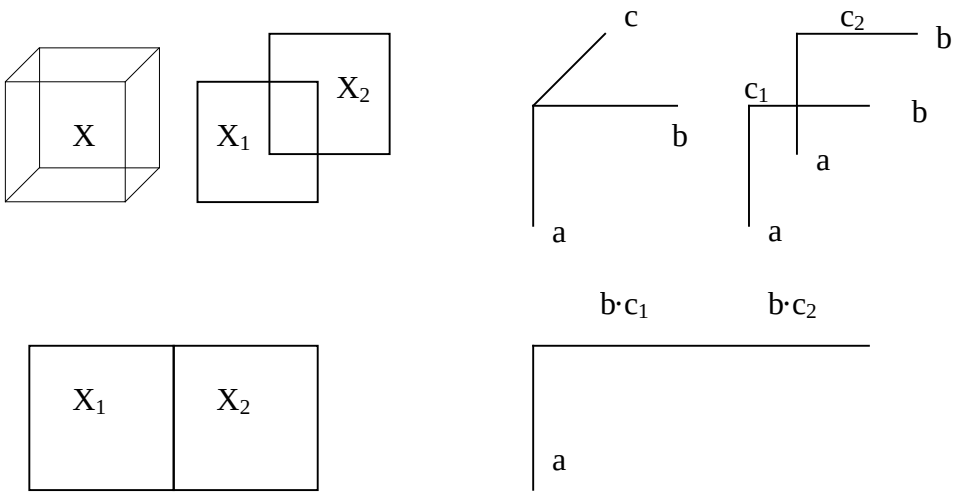

Figure 3.15 Unfolding data cube process and transferring it to 2D-matrix

The calibration data set was satisfactorily compressed using a total of 14 principal components. The predicted values of breakdown number for all oil samples using PCR analysis are presented in Figure 3.16 This calibration model can now be used to determine the relative breakdown number of unknown oil samples. While the model efficiency was compatible with previous studies on lubricant quality indicators[120], the inconsistency of the aged oil samples was a barrier towards more effective analysis and accurate results. Since, usually, there is no control and little knowledge about the history

of the field samples, the model would be severely restricted in its predictive power. This is manifested in the low variance, R^2= 0.77, for the correlation of true and predicted BDN, Figure 3.16.

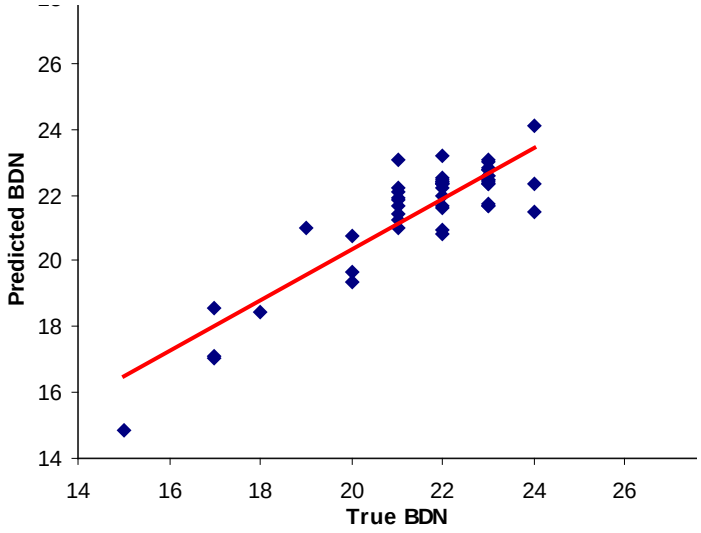

Figure 3.16 PCR model for prediction of breakdown number of oil

3.4 Discussion

3.4.1 Chemistry of Lubricant Oxidation

As lubricants degrade, their physical properties such as viscosity, hydrophobicity, and homogeneity change. These changes lead to increased friction and wear. This degradation is mainly due to chemical breakdown, which may be categorized as thermal (non-oxidative) degradation and oxidative degradation. Thermal degradation occurs solely as a result of heat and mechanical forces, whereas oxidative degradation occurs in

the presence of the oxygen in air, and becomes significant when combined with heat and metal surfaces. The free radicals that are formed in the initial oxidation steps include alkyl, alkoxy and peroxy radicals. They further react with hydrocarbon molecules in the oil resulting in a chain reaction[1, 4] (see section 2.2.3.1). As end products, one frequently finds carboxylic acids, long-chain, and short-chain hydrocarbons. Since the oxidation of oil propagates by free radical attacks against the base stock's compounds, radical scavengers can act as antioxidant additives. They interrupt the radical chain mechanism by donating hydrogen atoms to the hydrocarbon radicals and form stable radicals through resonance. Typically, blended polyol ester engine lubricants contain 1-3% additives that are primarily antiwear and antioxidant additives. Antioxidant additives added to polyol ester base stock are usually aromatic compounds such as phenyl-α-naphthylamine (PAN or PNA) or diphenylamine (DPA), as well as their derivatives such as octylphenyl-α-naphthylamine (OPAN) and dioctyldiphenylamine (DODPA)[4].

In the jet turbine lubricant used in this study, one of these two antioxidants can be identified as PAN; as is apparent in the first panel of Figure 3.13, the fluorescence of PAN in silicone oil shows a strong EEM feature at 370^{exc} / 400^{em} nm, which is also consistent with the EEM spectrum Liu et al. obtained in 2012[121]. In addition, the EEM spectra of components 1 obtained from jet turbine oil and from mixing PAN into silicone oil (Figure 3.7) are very similar to the EEM spectrum of the fresh Si-oil/PAN mixture (Figure 3.13). The second fluorescent additive is more difficult to identify. For example, DPA exhibits fluorescence excitation and emission at shorter wavelengths than observed for PARAFAC component 3. This was confirmed, here, by recording the fluorescence EEM spectra of DPA in silicone oil (320^{exc}/340^{em} nm; spectrum not shown). DODPA and

DPA are expected to have similar fluorescence signatures, whereas OPAN should not exhibit a stronger oxidative resistance compared to PAN. The mass spectrum (GC-MS, Agilent Technologies) of fresh jet turbine oil was also inconclusive, so that we cannot speculate on the identity of PARAFAC component 3.

On the other hand, PARAFAC component 2 is straightforward to identify as the PAN-dimer. When oxidizing silicone oil which contains PAN as its only antioxidant, the observed changes in the fluorescence EEM spectra are presumably due to the reaction of PAN with oxygen, rather than base stock radicals. It is known that PAN radicals form a dimer, which can further act as an antioxidant (Schematic 3.1)[4].

In the following, we designate unreacted phenyl-α-naphthylamine as PANH, the radical product as $PAN^{\bullet}$ and the dimer as PAN_2.

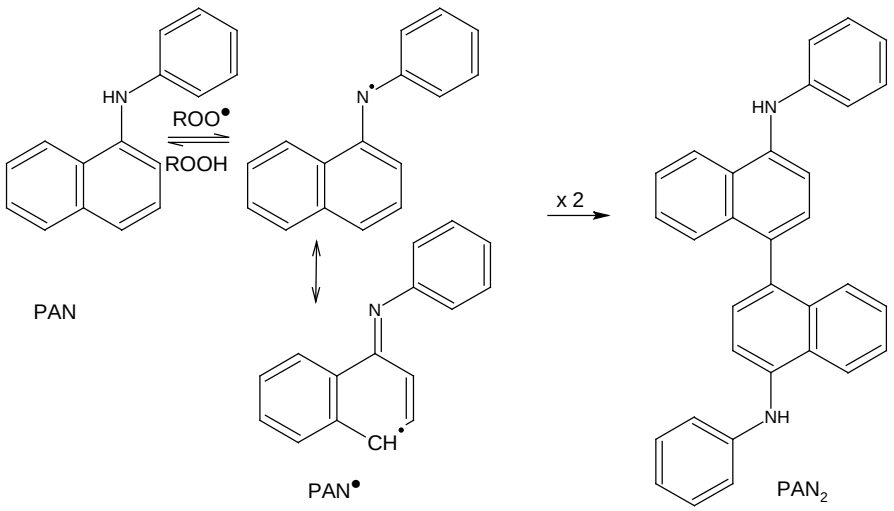

Schematic 3.1 Reaction of PANH with radicals and formation of the PAN-dimer

Our experimental results are consistent with the following simple model: PANH molecules are responsible for the strong fluorescence feature of component 1, which is

apparent in fresh oil and, of course, in the mixture of PANH in silicone oil. The primary radical oxidation products (or oxygen) react with PANH to produce its dimer, PAN_2, which we expect to exhibit absorption and fluorescence emission at slightly longer wavelengths than PAN. This was indeed observed for component 2. Once both PANH and PAN_2 have been removed, oxidation modifies the remaining compounds which have higher oxidation stability. One of these is the unidentified antioxidant, AO, which was identified as PARAFAC component 3. Apparently, the final oxidation products no longer strongly fluoresce and the PARAFAC scores of all three components decay eventually. Only when the antioxidants AO, PANH and PAN_2 have been depleted, the base stock will be oxidized.

Mass spectrometric analysis (ESI Quadrupole Time of Flight Mass Spectrometer, AB Sciex Qstar XL) is consistent with this model and, indeed, revealed that silicone oil containing initially just PANH (molecular weight=219.2812 amu) as an antioxidant produced a product with a mass to charge ratio of 437.2 amu after 31700 min of oxidation at 195° C, in a process that is consistent with the formation of the PAN_2 dimer (molecular weight=436.5464 amu). (Figure 3.17 and Figure 3.18). Note that different resonant structures of the radical form of $PAN^{\bullet}$ may produce a PAN_2 dimer with an identical mass but possibly different EEM signatures. Our EEM spectra are consistent with a dominant isomer of PAN_2 (or a mixture of isomers with very similar EEM spectra), but we cannot be sure about the identity of this isomer.

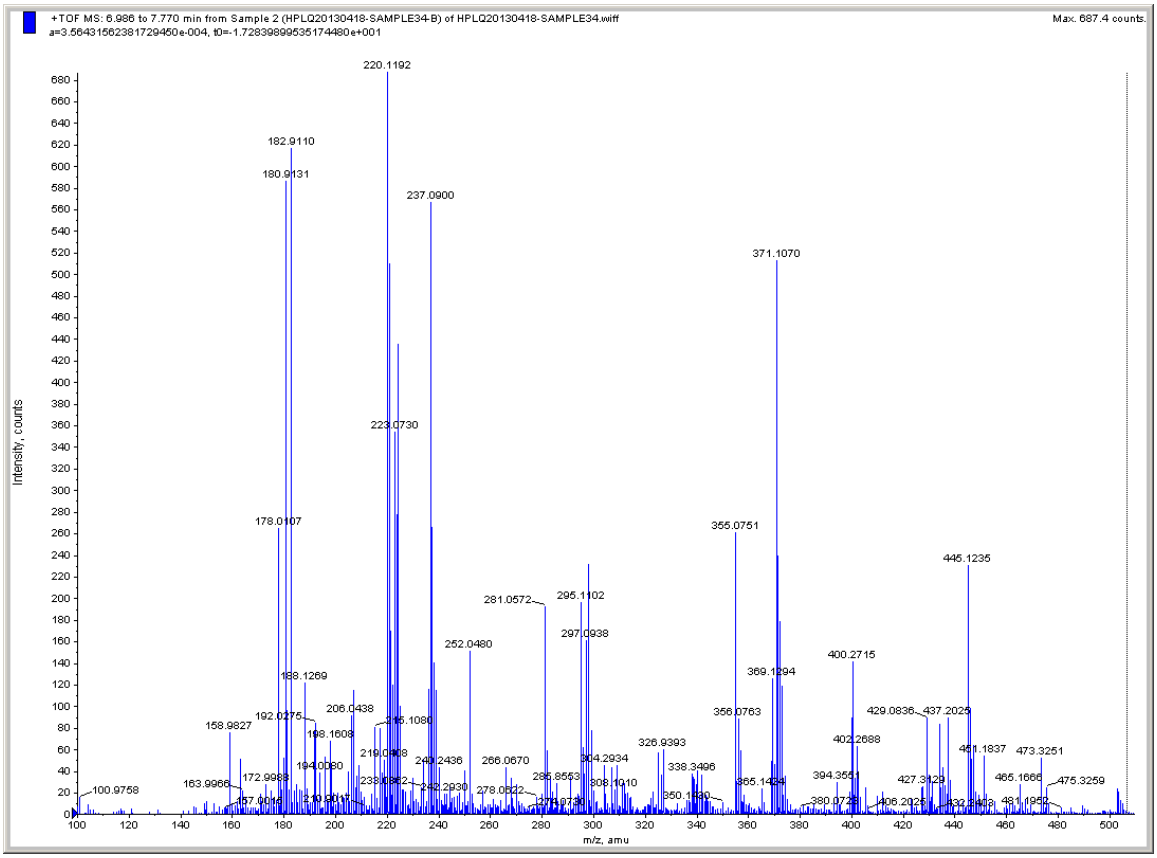

Figure 3.17 Mass spectrum corresponding to the mixture of PANH in silicone oil (non heated).
The signal with the mass to charge ratio of 220.1192 amu is related to the molecular ion of PANH. No attempt was made to assign the many other peaks to lubricant constituents.

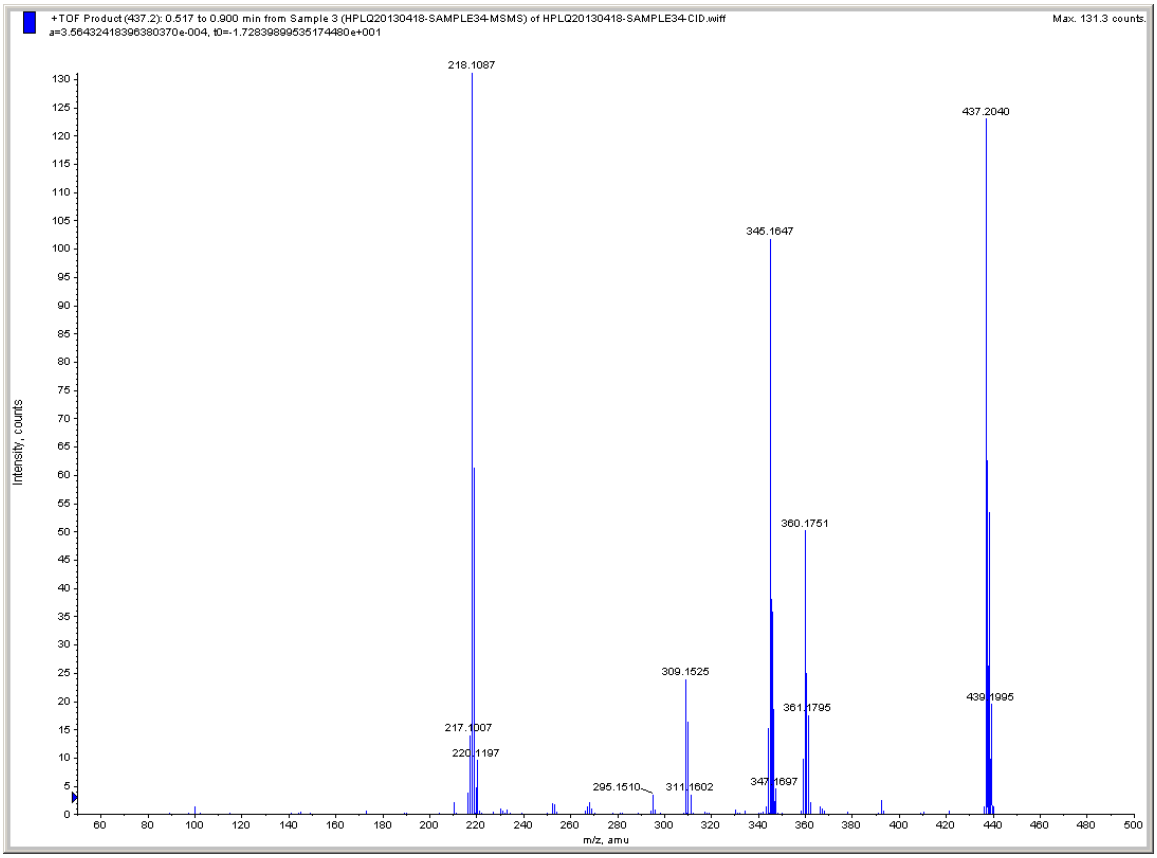

Figure 3.18 Mass spectrum corresponding to the mixture of PANH in silicone oil (heated).
The signal with the mass to charge ratio of 437.30 amu is related to the molecular ion of PAN_2. The third strongest feature at 345.1647 amu is consistent with the loss of C_6H_5NH by the PAN_2 dimer, whereas the feature at 360.17corresponds to the loss of a phenyl group (C_6H_5) by the PAN_2 dimer (or an addition of naphtylamine to the PAN radical). The weak feature at 309.15 amu is consistent with an addition of aniline to the PAN radical.

In addition, we can associate the decrease in fluorescence, e.g. the depletion of antioxidants, with the onset of base oil oxidation. Figure 3.9 shows that the conductivity of the water capturing the volatile reaction products of the lubricant oil oxidation rises as the fluorescence of components 1, 2, and 3 has diminished.

In combination, these results permit us to specify the time at which the antioxidant additives are no longer capable of inhibiting oxidation of the base oil. In our case of forced and accelerated oxidation at high temperatures, this point arrived at about 10,000 min, 3,500 min and 400 min when oil was heated to 150° C, 195° C, and 215° C, respectively. Most importantly, this breakdown point can be obtained using a simple in-line fiber probe. A possible sensor design based on either an EEM spectrometer or a variety of monochromatic light sources is discussed in session 6.2.1.

When comparing the time evolution of the EEM spectra of field samples and lab samples, it was found that the field samples had consistently high PARAFAC scores of component 3, whereas an FTIR analysis showed a much higher degree of oxidation. In the light of the above discussion, we note that (a) the oil change intervals are set such that the oil has sufficient lubricity, and antioxidants are therefore not depleted, (b) mixing of small amounts of strongly oxidized oil (engine sludge) having a very high BDN with less oxidized oil will show a strong oxidation signature in the FTIR spectrum (high BDN), though may still be rich in antioxidants. Since it is more important to know the antioxidant level and therefore the oxidation resistance of the base-oil than to know the level of contamination of heavily oxidized species, we submit that the fluorescence EEM signatures are more reliable indicators for oil lubricity than conventionally obtained breakdown numbers.

3.4.2 Kinetic Model

We consider a greatly simplified model for the reaction of inhibitors PANH and AO with organic radicals, ($R^{\bullet}$, $RO^{\bullet}$, and the peroxy-radicals $ROO^{\bullet}$) that are formed either by oxidation or pyrolysis[75].

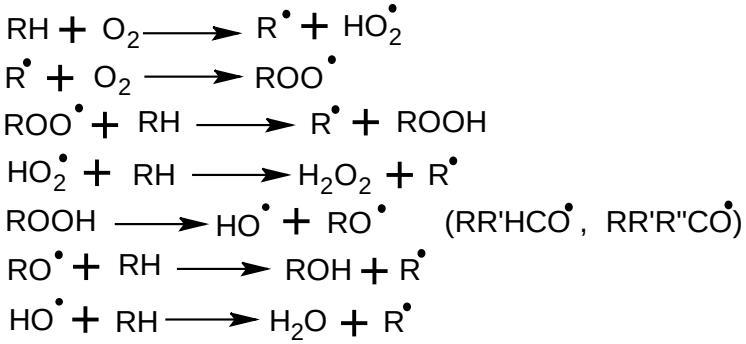

The oxyradical $RO^{\bullet}$ can be primary, secondary, or tertiary depending on the position of the initial *CH* bond cleavage. Secondary and tertiary oxyradicals have then the potential to further decompose into aldehydes and ketones respectively.

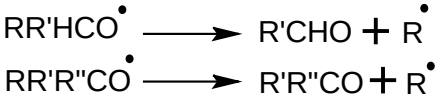

In the absence of inhibitors or antioxidants, the oxidation proceeds to give volatile organic acids *RCOOH*, which can be detected by conductivity measurements after solvation in water.

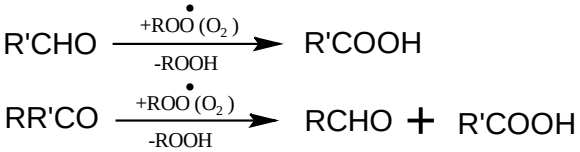

In the presence of antioxidants such as PANH, the radicals are scavenged and converted into stable compounds.

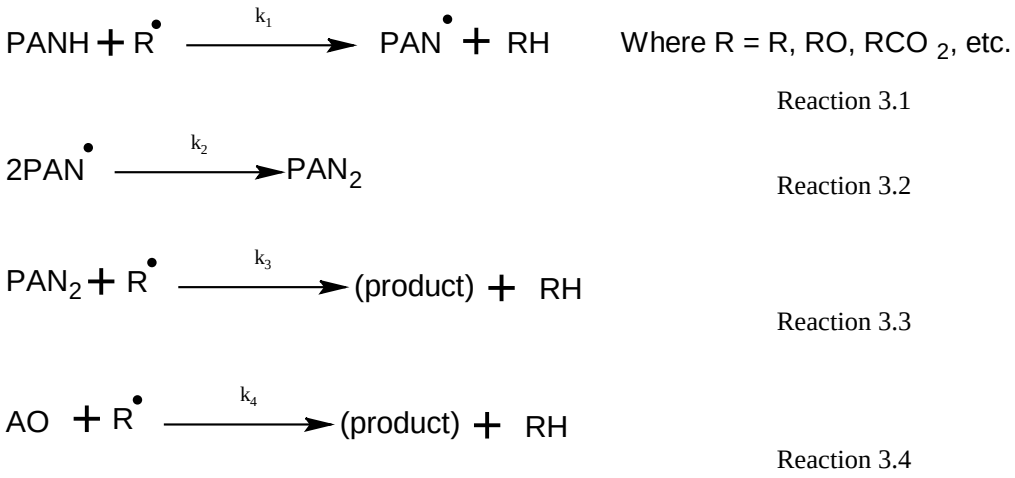

The concentration-time profiles of the fluorescent molecules PANH and PAN_2 as well as the antioxidant molecule AO are determined by the rate equations:

$$\frac{d[PANH]}{dt} = -k_1[PANH][R^{\bullet}] \quad (3.2)$$

$$\frac{d[PAN^{\bullet}]}{dt} = k_1[PANH][R^{\bullet}] - k_2[PAN^{\bullet}]^2 \quad (3.3)$$

$$\frac{d[PAN_2]}{dt} = k_2[PAN^{\bullet}]^2 - k_3[PAN_2][R^{\bullet}] \quad (3.4)$$

$$\frac{d[AO]}{dt} = -k_4[AO][R^{\bullet}] \quad (3.5)$$

One may make the following assumptions:

1. The consumption rate of the fluorescent antioxidant molecule(s) AO is slower than that of PANH: $k_4 < k_1$
2. The concentration of PAN-radicals is constant, while PANH is at large excess over the organic radicals [$R^{\bullet}$]. This allows setting $k_1[PANH][R^{\bullet}] = k_2[PAN^{\bullet}]^2$

3. The concentration of radicals is constant while PANH is at large excess over the organic radicals [$R^{\bullet}$]. This allows setting $k_1^{'} = k_1[R^{\bullet}], k_3^{'} = k_3[R^{\bullet}], k_4^{'} = k_4[R^{\bullet}]$

With these assumptions, we can rewrite Equation (3.4) as

$$\frac{d[PAN_2]}{dt} = k_1^{'}[PANH] - k_3^{'}[PAN_2] \tag{3.6}$$

Solving the differential equations gives

$$[PANH] = [PANH]_0 \exp\left(-k_1^{'}t\right) \tag{3.7}$$

$$[PAN_2](t) = \frac{k_1^{'}[PANH]_0}{k_3^{'} - k_1^{'}}\left\{\exp\left(-k_1^{'}t\right) - \exp\left(-k_3^{'}t\right)\right\} \tag{3.8}$$

$$[AO] = [AO]_0 \exp\left(-k_4^{'}t\right) \tag{3.9}$$

Equation (3.7) was derived from Equation (3.5) and (3.6).

$$\frac{d[PAN_2]}{dt} + k_3^{'}[PAN_2] = k_1^{'}[PANH] = k_1^{'}[PANH]_0 \exp\left(-k_1^{'}t\right) \tag{3.10}$$

Equation (3.10) is an inhomogeneous differential equation for [PAN_2]. The general solution is the sum of two terms, i.e. the solution to the homogeneous equation, with the RHS equal to zero, and the particular solution for the equation with the non-zero RHS. The homogeneous solution is:

$$[PAN_2](t) = A\exp\left(-k_3^{'}t\right) \tag{3.11}$$

while the particular solution is

$$[PAN_2](t) = -A\exp\left(-k_1^{'}t\right) \tag{3.12}$$

Requiring that $[PAN_2](t=0) = 0$ defines $A = -\frac{k_1^{'}[PANH]_0}{k_3^{'} - k_1^{'}}$, and the general solution is therefore given by Equation (3.8).

Despite the simplicity and crudeness of this model, the fluorescence time profiles can be described very well over an astonishing 3 temporal orders of magnitude, i.e. from about 10 min to 10,000 min. From a fit to Equations (3.7), (3.8) and (3.9) to the fluorescence-time profiles (Figure 3.9 and Figure 3.14) we were able to determine rate constants $k_1^{'}$, $k_3^{'}$ and $k_4^{'}$ as well as $[AO]_0$ and $[PANH]_0$. Of course, the three rate constants (Table 3.2) are composite rate constants that also depend linearly on the oxygen concentration and the presence of other oxidizers.

T /K	***423***	***468***	***488***	***E_a /kJmol^{-1}***
$[PANH]_0$	$2.28 \times 10^3/2.70 \times 10^3$	$2.22 \times 10^3/3.70 \times 10^3$	$4.10 \times 10^3/4.10 \times 10^3$	
$k_1^{'}$ *(min^{-1})*	3.30×10^{-3}	4.34×10^{-2}	1.1×10^{-1}	93±2
$k_3^{'}$	3.09×10^{-4}	4.68×10^{-3}	2.71×10^{-2}	114±15
$k_4^{'}$ *(min^{-1})*	1.21×10^{-4}	1.65×10^{-3}	1.25×10^{-2}	116±20

Table 3.2 Rate constants of the formation of PAN2 and the decay of PANH, PAN2 and AO in jet turbine oil.
The data obtained by fitting rate equations (3.7) - (3.9) to the data in Figure 3.9 and activation energies to the data of Figure 3.19. The two values of $[PANH]_0$ are obtained from two separate fits to equations (3.7) and (3.8).

Nevertheless, using fluorescence-time profiles at 150° C, 195° C, and 215° C and the associated rate constants, one can obtain activation energies and estimates for pre-exponential factors using simple Arrhenius graphs, shown in Figure 3.19.

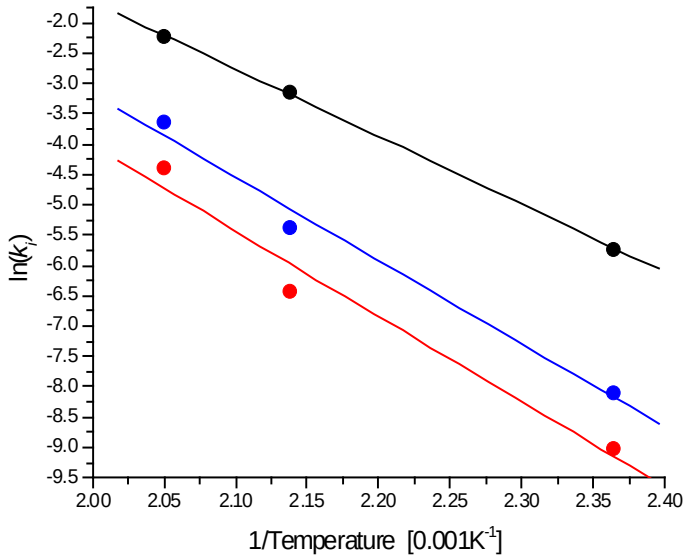

Figure 3.19 Arrhenius plots to determine the activation energies listed in Table 3.2.
The rate constants are composite rate constants that also depend on the concentration of organic radicals and oxygen (black: $k_1^{'}$; blue: $k_3^{'}$; and red: $k_4^{'}$).

It is insightful to compare the rate constants for reactions (Reaction 3.1 and Reaction 3.3) obtained by oxidizing jet turbine oil to those associated with oxidation of PANH mixtures in silicone oil. By comparing k'_1 in Table 3.3 and Table 3.3 one sees that PANH in silicone oil degrades about 6- to 10-times more slowly, compared to PANH in polyol ester oil. This may be due to reaction of PANH with small organic radicals that can form in polyol ester oil but not in silicone oil. While in the absence of antioxidants molecular oxygen may react directly with polyol ester oils and many other mineral and synthetic base stocks, such reactions are very slow in silicone oil. In both lubricants, the

direct reaction of oxygen with PANH is important, but in silicone oil, this is the only degradation reaction.

T /K	***468***
$[PANH]_0$	$3.58 \times 10^{3} / 8.76 \times 10^{3}$
K'_1 (min^{-1})	$5.21 \times 10^{-4} / 3.58 \times 10^{-4}$
K'_3	3.28×10^{-5}

Table 3.3 Rate constants of the formation of PAN_2 and the decay of PANH, and PAN_2 in PANH-silicone oil mixtures.

Data obtained by fitting rate equations (3.7) and (3.8) to the data in Figure 3.14. The two values of $[PANH]_0$ are obtained from two separate fits to equations (3.7) and (3.8).

The mass spectrum shows that PAN_2 is formed in silicone oil, and given the similarity of the EEM component 2 spectra (Figure 3.7), one may assume that PAN_2 is also the intermediate product in the oxidation reaction in jet turbine oil. In both oils, PAN_2 decays, but, again, the decomposition reaction in silicone oil is about 10-times slower than the respective reaction in polyol ester oil. As for PANH, the difference is likely due to the much higher concentration of organic radicals in the polyol ester oil.

The kinetic model relies on the steady state assumption for the organic radicals and involves effective reaction rates. As soon as PANH, PAN_2 and AO are all depleted, one expects that the model breaks down and the concentration in organic radicals rises. At this point, the slower reactions forming aldehydes, ketones and organic acids proceed and the base stock of the oil breaks down. It is therefore not surprising that the depletion of the antioxidants coincides with the sudden onset of the formation of volatile acids as can be seen in Figure 3.9.

In Figure 3.12, we correlated the breakdown number to the score of component 3, *i.e*. the fluorescence contribution of the antioxidant AO. Given the calculated activation energy (Table 3.2), we can now quantify the relative concentration of this component as a function of temperature and time. The half-life of AO can be calculated with the pre-exponential factor A = 3 × 10^{10} min^{-1} and activation energy E_a = 116 kJ/mol from the linear fit in Figure 3.19.

$$t_{1/2}(\text{min}) = \frac{\ln 2}{A\exp\left(-\frac{E_a}{RT}\right)} = 2.4\cdot 10^{-11}\exp\left(\frac{14,000K^{-1}}{T(K)}\right) \tag{3.13}$$

Finally, we can use the empirical correlation of the oil breakdown number (BDN) to the fluorescence PARAFAC score of the antioxidant AO to determine the breakdown number (Figure 3.12). For this particular oil, we found the relation to be:

$$BDN = 123\cdot score^{-0.3} \tag{3.14}$$

At half life, $t_{1/2}$, the PARAFAC score of AO is reduced to one-half and the BDN is then increased by a factor 1.23 = $0.5^{-0.3}$.

3.5 Conclusions

The fluorescence of the particular synthetic lubricant in this study (NYCO jet turbine oil) is dominated by the contributions of two antioxidants and can be easily and robustly quantified using a fiber optic probe – even at the elevated temperatures typical for a running engine. The antioxidant concentration is directly related to the oxidative stability of the lubricant and, as the antioxidants are depleted, the base stock of the lubricant rapidly degrades.

It may appear coincidental that the fluorescence of the lubricant happens to be so strongly correlated to the chemical constituents that are also responsible for the oxidative stability. On the other hand, antioxidant additives typically consist of conjugated aromatic systems. While the conjugation promotes donation of a hydrogen atom and helps stabilize the intermediate radical, it is also associated with strong fluorescence emission in the visible region of the spectrum. Other antioxidants such as dioctyldiphenylamine and even metal-ligand systems that are added to some lubricants may show very similar behaviour.

It is remarkable that most synthetic base stock is not fluorescent in the near-UV/Vis region such as the polyol ester stock and the silicone oil used in this study. Lubricants with low lying excited states and/or a high degree of unsaturation are likely susceptible to oxidation and even polymerization. We therefore speculate that the results of our study can be transferred to other lubricant systems with different base stock and antioxidant or anti wear additives.

Finally, one may even consider adding PANH to lubricant base stocks that either are depleted of PANH to enhance the longevity of the lubricant or to add it to other lubricants that do not already contain PANH, as a ”beacon” for oxidative stability.

4 Chapter 4. Modeling of Fiber Bundle Collection Efficiency in Strongly Absorbing Liquids*

4.1 Introduction

As shown in the preceding chapter, fluorescence spectroscopy has a great potential for real-time and online measurements of lubricant oil constituents, since it is non-intrusive and does not require the withdrawal of a sample. These capabilities are well known and the use of fiber-optic probes together with fluorescence spectroscopy has become a convenient method to realize the full potential of fluorescence detection[122]. Silica fiber probes and plastic waveguide probes have been used to transfer the excitation light to the sample and to collect the fluorescence light. Fiber-coupled fluorescence measurements have been used to study foodstuff[123], drinking water[124], human tissue[125], PAHs[22] and industrial fluids such as lubricant oils[120, 126]. Using compact and bright excitation sources and fiber probes together with scaled-down spectrometers have introduced portable and compact fluorescence detection systems[127]. Mazzinghi employed a red laser diode coupled to a fiber probe as an excitation source and a photodiode for the fluorescence detection to build a prototype fluorosensor for monitoring the chlorophyll II level in leaves[128]. To make miniature EEM fluorometers, a fiber-coupled multi-wavelength LED array also has been used together with a CCD camera to collect the

* [Munzke, D.; Saunders, J.; Omrani, H.; Reich, O.; Loock H.P., Modeling of fiber-optic fluorescence probes for strongly absorbing samples. *Applied Optics* **2012,** *51* (26), 6343-6351.]This paper was published in [*Applied Optics*] and is made available as an electronic reprint with the permission of OSA. The paper can be found at the following URL on the OSA website: [http://dx.doi.org/10.1364/AO.51.006343]. Systematic or multiple reproduction or distribution to multiple locations via electronic or other means is prohibited and is subject to penalties under law.

EEM spectrum of samples[129]. Earlier, the same research group, Hart and Renee, used similar setup without fiber probes[130]. They focused light from each LED in an array on a different spot of the sample, held in a quartz cuvette, using a lens. From each excited spot in the sample, the fluorescence light was guided to the CCD camera using mirrors and lenses. Obviously, coupling the fiber probe to each LED in the array made the process much easier[129]. Finally, large and complex fluorescence spectrometers have been redesigned into adaptable instruments for field measurements to conduct EEMS experiments[7, 22, 131].

In general, a fluorescing sample may strongly absorb light. The absorption of the excitation light and the re-absorption of the emitted fluorescence are therefore important considerations when designing fiber-optic probes, since they limit the volume of liquid that produces detectable fluorescence.

For applications in process monitoring, assessment of lubricant and fuel quality, environmental assessment, and food quality assurance, the samples need to be investigated in situ and undiluted. Strong fluorescence is then frequently accompanied by strong scattering and absorption. An ideal probe can be used to collect fluorescence EEM spectra following excitation of strong absorption bands with respective strong re-absorption of the fluorescence signal, but it can also be used to excite weakly absorbing spectral features and detect faint fluorescence emission. In samples such as industrial lubricants, the absorption coefficients and the corresponding fluorescence emission intensity spans 4 to 5 orders of magnitude in the UV-Vis-NIR spectrum, and only a probe with a large dynamic range is capable of capturing the information contained in all spectral features[7].

Recent work on optimization of fiber probes for medical samples has highlighted the need to collect the fluorescence (or Raman signal) before it is attenuated by the sample. Configurations include simple bifurcated fibers[132] and fiber bundles in which the fiber ends are angled toward each other[133], or bevelled to refract the fluorescence into the fiber[134]. The gaps between the collection fibers in a fiber bundle are avoided, and the collection efficiency is further increased, when a coaxial design is used. For example, the excitation fiber may be surrounded by a high-index capillary that is capable of collecting and guiding the fluorescence to the detector[131]. For the same purpose, a double-clad fiber has also been used previously[135].

Modeling has been used extensively to quantify the effect of this dead volume. For example, Ma et al.[132] derived an analytical expression that permits the calculation of the fluorescence intensity as a function of the core and cladding radius of the adjacent excitation and the collection fiber in a bifurcated fiber probe. Other studies examined the effect of the distance between a planar fluorescence emitter and the end of a bifurcated fiber probe[135] using Monte Carlo simulations. Almost all previous modeling studies have assumed that the fluorescence medium has negligible absorption[132] or that it is planar[136]. These studies were therefore not designed to quantify the effect of primary absorption of the excitation light and secondary absorption of the emitted fluorescence. The (re-) absorption of light may be neglected when the sample is very dilute or in the gas phase[137] but cannot be ignored in many undiluted liquid samples.

As was explained in chapter 3, a bifurcated fiber probe was designed and built to study the fluorescence history of materials with high optical density such as turbine lubricant oils. In such cases, the effect of primary and secondary absorption has to be

carefully considered. This chapter presents a theoretical investigation that was performed to optimize the fiber-optic detection system for collection of the fluorescence light. A more thorough study investigating a variety of irradiation and detection geometries was co-published by the author of this thesis[118] and below we only highlight those aspects of the study that are relevant to the thesis work.

4.2 Theoretical model

The fluorescence collection efficiency in absorbing samples was quantified using a coaxial-bifurcated probe design. The fluorescence intensity was calculated for detection through six fibers that surround the excitation fiber and that have the same numerical aperture (Case 4 in Figure 4.1).

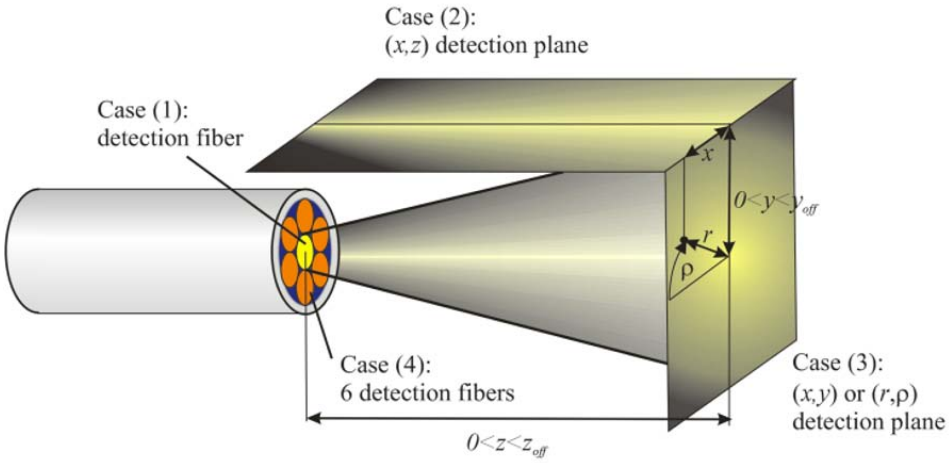

Figure 4.1 Sketch of the fluorescence detection configuration using bifurcated fiber probe

The excitation of the sample's fluorescence is characterized using the model described by He and Cuomo[138] for multimode-fiber emission. They proposed a theoretical function that described the emission cone from a multimode-fiber optic and determined the intensity distribution in front of the distal end of the bundle.

Figure 4.2 represents their assumptions for developing their theoretical model in detail. As shown in Figure 4.2, all incident beams with the angles $\theta \leq \theta_c$ will couple into the emitting fiber. Accordingly, the edge of the cone including exiting rays from distal end of the fiber is defined by θ_c. He and Cuomo assumed that all uniangular beams propagating through the fiber carry the same intensity, i.e. that the mode fill factor is uniform.

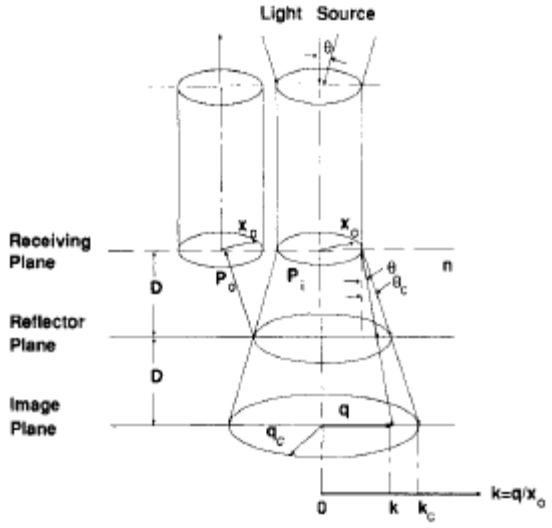

Figure 4.2 Coordinate of a two-fiber level. Right, emitting fiber. Left, collecting fiber.
From reference 138.

He and Cuomo described that the uniangular beam which exits the fiber in the θ direction will construct a ring on the image plane as it is shown in Figure 4.3.

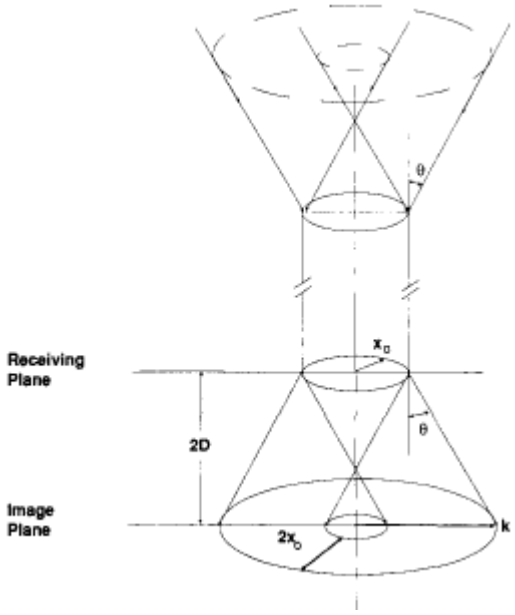

Figure 4.3 The ring produced on image plane by a light ray coupled to the fiber at an angle θ.
From reference 138.

The width of this ring is equal to the fiber core diameter and based on their assumptions the light intensity which was uniformly distributed on it could be calculated as

$$I_u = \frac{l}{2\left(k^2 - 2k + 2\right)} \qquad 1 \le k \le 2 \tag{4.1}$$

$$I_u = \frac{l}{2\left(4k - 4\right)} \qquad k \ge 2 \tag{4.2}$$

Where l is the intensity of an incident beam that leaves the fiber at an angle θ.

According to He and Cuomo[138], "An infinite number of equal power uniangular beams within $0 \le \theta \le \theta_c$, will produce an axial symmetric intensity distribution on the image plane. The integrated intensity for the point with coordinate k on the image plane can be calculated as":

$$I_{exc} = I_k = \int_k^{k'} I_u \frac{A}{1 + A^2 (k-1)^2} dk \quad \begin{matrix} k' = k + 2 \ for \ k + 2 \le k_c \\ k' = k_c \ for \ k + 2 > k_c \ (k_c \ge 1) \end{matrix} \tag{4.3}$$

where $A = x_0 / 2D$.

Note that He and Cuomo used a two-dimensional (2D) model to determine the function $I_{exc}(r, z)$, where z is the distance from the fiber front surface and r is the radial coordinate[138]. Here, to describe the light intensity in three-dimensional excitation cone, an Abel transform of the 2D model around the center axis was generated, $I_{exc}(r,\rho,z)$, (Equation (4.4)).

$$I(x, z) = 2 \int_x^{\infty} \int_0^{2\pi} I(r, \rho, z) \frac{r}{\sqrt{r^2 - x^2}} d\rho \, dr \tag{4.4}$$

For simplicity, to determine the fluorescence probability, all calculations were performed on the 2D cross section of the intensity distributions and then the Abel transform was applied as the final step. The excitation cone is further modified by the absorption of the sample, given here as the inverse $1/e$ absorption length α_{exc} (cm^{-1}). The intensity attenuated by absorption of the excitation beam (primary absorption) is approximated as

$$I_{prim}(r, z) = I_{exc}(r, z) \times \begin{cases} \exp(-\alpha_{exc} z) & if \ r < r_0 \\ \exp\left(-\alpha_{exc} \sqrt{z^2 + (r - r_0)^2}\right) & if \ r > r_0 \end{cases} \tag{4.5}$$

The fluorescence emission is assumed to be isotropic, and consequently we can simply determine the probability of detecting the fluorescence from any point in the emission cone by calculating the solid angle formed by the detector plane. In addition, we

need to consider the absorption of the fluorescence by the sample α_{em} (cm^{-1}) ("secondary absorption" or "re-absorption") and the respective absorption length.

For the proposed configuration the fluorescence intensity that falls into six fibers placed in a ring with outer radius $2r_{cl}$ and inner radius r_{cl} (Figure 4.4) can be calculated as in Equation (4.6).

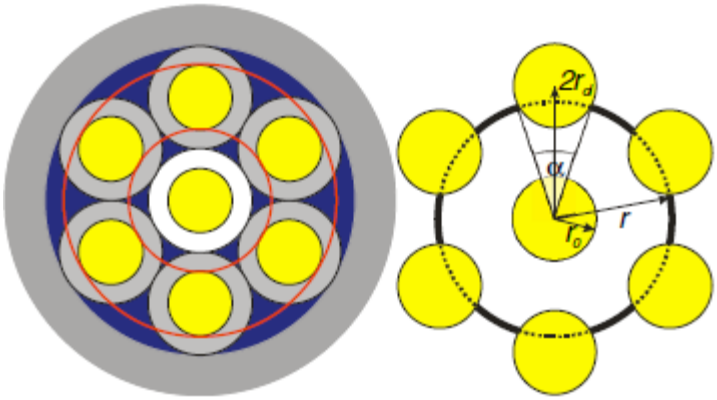

Figure 4.4 Geometry of the 50 ⁄125 μm fiber bundle.

$$I_{\det ect}(r,z)=\begin{cases} I_{prim}(r,z)\times CE_A(r,z)\times \exp\left(-\alpha_{em}\sqrt{z^2+(r-2r_{cl})^2}\right), & if\ r>2r_{cl}+r_0 \\ I_{prim}(r,z)\times CE_B(r,z)\times \exp\left(-\alpha_{em}\sqrt{z^2+(r_{cl}-r)^2}\right), & if\ r<2r_{cl}-r_0 \\ I_{prim}(r,z)\times CE_C(r,z)\times \exp(-\alpha_{em}z), & if\ 2r_{cl}-r_0<r<2r_{cl}+r_0 \end{cases} \quad (4.6)$$

The collection efficiency of six fibers with core radius r_0 and cladding radius r_{cl} can be calculated as

$$CE_A(r,z) = \Gamma(r,z) \times \left(\arctan\left(\frac{r - 2r_{cl} - r_0}{z} \right) - \arctan\left(\frac{r - 2r_{cl} + r_0}{z} \right) \right), \quad if\ r > 2r_{cl} + r_0$$

$$CE_B(r,z) = \Gamma(r,z) \times \left(\arctan\left(\frac{2r_{cl} - r_0 - r}{z} \right) - \arctan\left(\frac{2r_{cl} + r_0 - r}{z} \right) \right), \quad if\ r < 2r_{cl} - r_0$$

$$CE_C(r,z) = \Gamma(r,z) \times \left(\arctan\left(\frac{2r_{cl} + r_0 - r}{z} \right) + \arctan\left(\frac{r - 2r_{cl} + r_0}{z} \right) \right), \quad if\ 2r_{cl} - r_0 < r < 2r_{cl} + r_0 \tag{4.7}$$

The angles calculated from the arctan(-) functions are restricted to be smaller than the critical incidence angle, Θ_C. The term $\Gamma(r, z)$ takes into consideration that the collection area offered by six fibers placed inside a ring (indicated by two red circles in Figure 4.4) increases from zero at the inner rim of the ring to a maximum near the center of the rim. The function $\Gamma(r, z)$ is defined between the inner and outer rim of the ring and can be derived as

$$\Gamma(r,z) = \frac{6}{\pi} \arctan\left\{ \frac{\sqrt{16r_{cl}^2 r^2 - \left[4r_{cl}^2 - r_0^2(z) + r^2\right]^2}}{4r_{cl}^2 - r_0^2(z) + r^2} \right\} \tag{4.8}$$

The width of the ring increases with distance z from the fiber ends according to the numerical aperture and the refractive index of the sample. This is expressed by

$$r_0(z) = r_0(0)\left(1 + \frac{z}{\sqrt{n^2 / NA^2 - 1}} \right) \tag{4.9}$$

4.3 Results of Theoretical Model

To determine the dynamic intensity range for the proposed detecting configuration, a number of assumptions were made. First, it was assumed that at all wavelengths both the fluorescence quantum efficiency and the detector response are unity, and that optical loss at the fiber-sample interface is negligible. These assumptions only introduce constant factors into the equations. We have selected the absorption coefficients of the fluorescent dye Eosin Y in our models. At the excitation wavelength of 532 nm, the molar extinction coefficient of the sample based on the decadic logarithm, ε, is 86,400 l mol^{-1} cm^{-1} [139, 140], and at the fluorescence maximum of 543.5 nm, ε = 24,500 l mol^{-1} cm^{-1}.

Fluorescence collection probability of two fibers aligned parallel to the center emission fiber was calculated using the approached model. The simulated dye concentration is varied in 18 steps between 430 nM and 0.11 M, and the refractive index is set to that of ethanol (n = 1.362), whereas the numerical aperture of the 50 ⁄ 125 μm multimode fiber is set to NA = 0.2.

At all concentrations the 2D image, $I_{prim}(r, z)$, of the excitation light after primary absorption and the probability that a particular volume element contributes to detected fluorescence, $I_{detect}(r, z)$ were calculated (Figure 4.5).

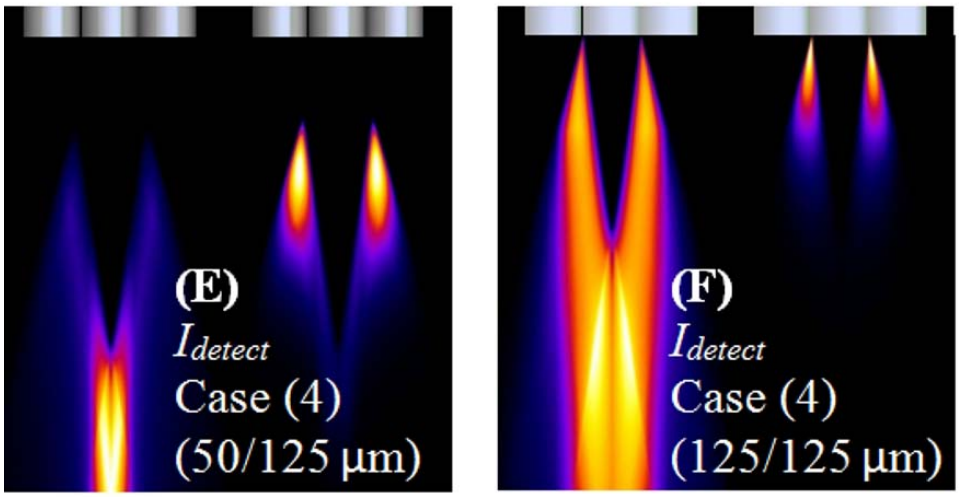

Figure 4.5 False-color 2D cross section of the spatial distribution of light following absorption and emission from a multimode fiber with a 50 μm core into Eosin Y dye solution in basic ethanol.
In both images, the left images assume an Eosin Y concentration of 3 μM, and the right images assume 440 μM. Intensities have been rescaled to cover the entire dynamic range of the image. Fluorescence collection probability of two fibers aligned parallel to the center emission fiber, where the emission and collection fibers have (E) a 50 μm core and 125 μm cladding diameter or (F) a 125 μm core and no cladding.

Since in a fiber bundle (or in a bifurcated fiber), the volume in front of the excitation fiber cannot contribute to the detected fluorescence (Figure 4.5 and Figure 4.6), the overall intensity then depends strongly on the mode overlap of the collection fiber(s) with the excitation fiber, i.e., on their distance, the thickness of the cladding, the numerical aperture, and the refractive index of the sample. As is illustrated in Figure 4.5 and Figure 4.6, changing the fiber from a 50/125 μm multimode fiber to a claddingless 125 μm fiber reduces the "dead volume" in front of the excitation fiber.

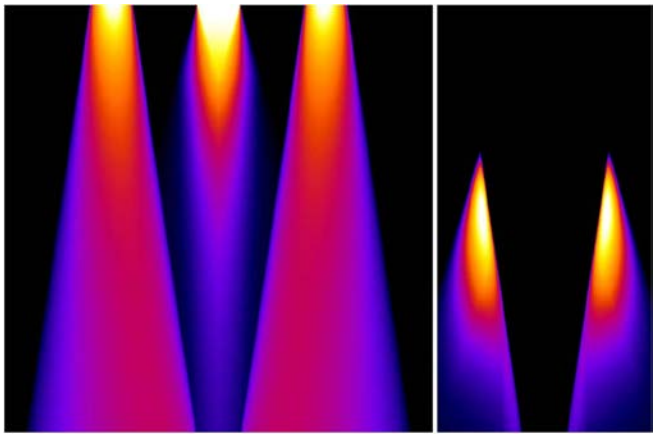

Figure 4.6 Left, collection efficiency of two fibers together with the fiber excitation cone (center); right, resulting fluorescence collection assuming a 440 μM concentration of Eosin Y.

This is important because almost the entire fluorescence excitation cone (Figure 4.6) falls into the "dead volume," and this effect is responsible for the sharp drop-off in detected fluorescence of strongly absorbing samples by fiber-bundle probes that is seen in Figure 4.7.

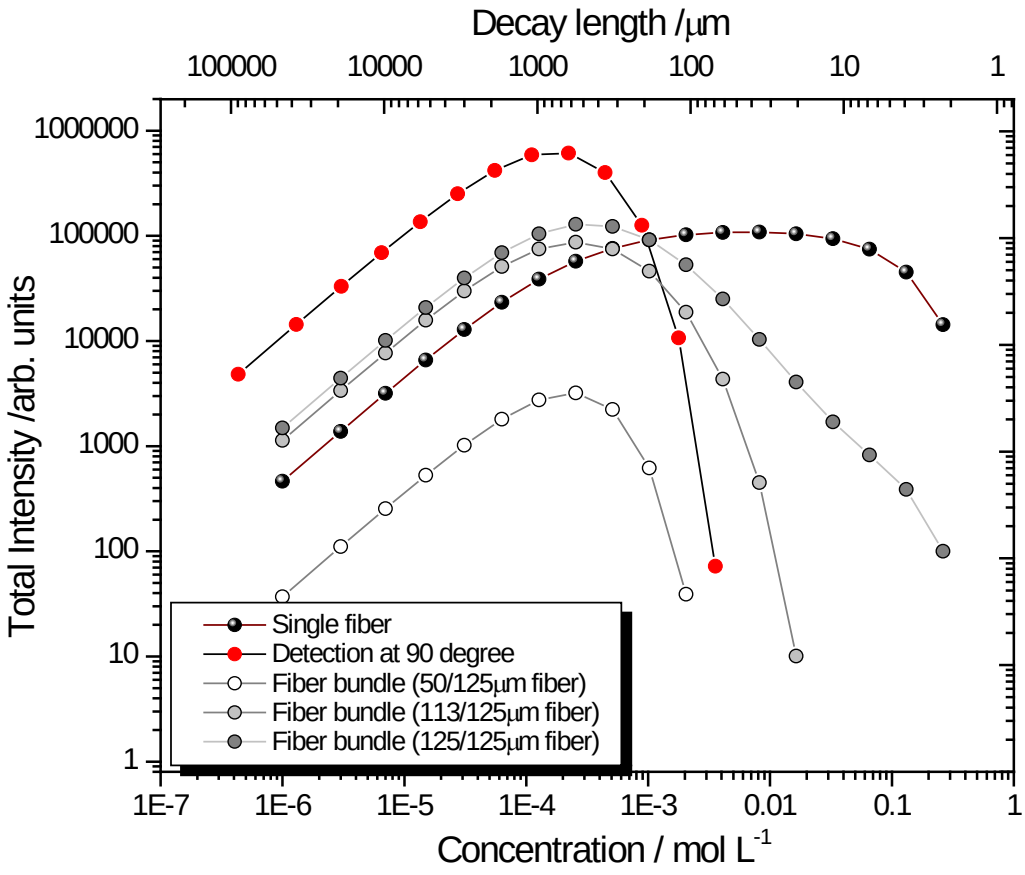

Figure 4.7 Calculated collected intensity for samples of different absorption length.
The simulation assumes NA = 0.20 and $n_{solution}$ = 1.362 and absorption coefficients of Eosin Y dye at the excitation wavelength of 532 nm (ε = 86400 L mol^{-1} cm^{-1}). A single fiber exciting and collecting the fluorescence works over the largest concentration range whereas fibers with no or a thin cladding outperform, both, fluorescence detection at a 90 degree configuration and a distance of 5 mm.

Figure 4.7 shows clearly that sampling in front of the excitation fiber is essential for measurements when primary and secondary absorption is high. This double logarithmic graph displays the total integrated intensity calculated from the Abel-transformed 2D intensity calculation results and is shown as a function of the Eosin Y concentration.

The largest concentration range is accessible when the same fiber is used for irradiation of the sample and for collecting fluorescence, whereas a fiber bundle is most efficient when the fibers have a very thin or no cladding. A counter propagating detection

setup with claddingless fibers shows favorable collection efficiency at short absorption decay lengths (with claddingless 125 μm fibers). A fiber bundle made with fibers of intermediate cladding diameter (113 / 125 μm) shows a lower range of detection, whereas a bundle made from 50 / 125 μm fibers has the lowest overall fluorescence collection. This is partly due to the reduced throughput through the smaller fiber core, but also due to the much larger dead volume.

The drop of collected fluorescence at low concentrations is partly due to an artifact of the modeling, since the integration volume is typically restricted to a cube of 500 μm length to reduce the computational time, except that it is 1 mm for fibers of 113 and 125 μm core diameter.

To overcome the effect of the dead volume one may use a transparent silica or quartz spacer in front of the bundle. In the spacer, the acceptance cones of the excitation and emission fibers overlap such that the fluorescence, which is generated in the sample and irradiates the front surface of the spacer, falls into the acceptance cones of the collection fibers. Ideally, such a spacer would have a radius of $2r_{cl} + r_0$ and a length of at least twice that of the dead volume.

4.4 Experiments and Results

4.4.1 Characterization of Fiber Probe

Figure 4.8 shows the picture of the home-built bifurcated fiber probe with a quartz window attached to its distal end. The required thickness for the quartz window, 1.95 mm, was calculated according to the value of the fiber numerical aperture (0.22), cladding thickness (40 μm) and the distal end diameter (2.2 mm).

Previously, in chapter 3, it was explained how using bifurcated coaxial fiber probe improved the fluorescence collection efficiency of jet turbine lubricant (Figure 3.2). Here the EEM signatures of crude oil were collected to characterize the effect of the attached spacer to the end of fiber probe.

Figure 4.8 Fiber probe ends with spacer attached to its distal end.

The EEM spectra of a crude oil sample supplied by Weatherford International were collected for either the neat sample or the sample dissolved in hexane (0.1%, 10000 ppm_v). As it is shown in Figure 4.9 the sample is quite dark, thick and strongly absorbing.

Figure 4.9 Crude oil sample supplied by Weatherford International

As is apparent in Figure 4.10, once the fiber bundle probe is equipped with a spacer the detection of fluorescence of the crude oil is readily possible. The EEM spectra were collected using the Varian spectrofluorometer (Cary Eclipse) as described in chapter 3. The voltage of the photomultiplier tube (PMT) detector was set to 850 V. All fluorescence emission spectra were recorded at excitation wavelengths from 225 to 600 nm with a 5 nm increment. The fluorescence was detected at 570 emission wavelengths from 230 to 800 nm with 1 nm increment. The bandwidths were 5 nm for both excitation and emission light.

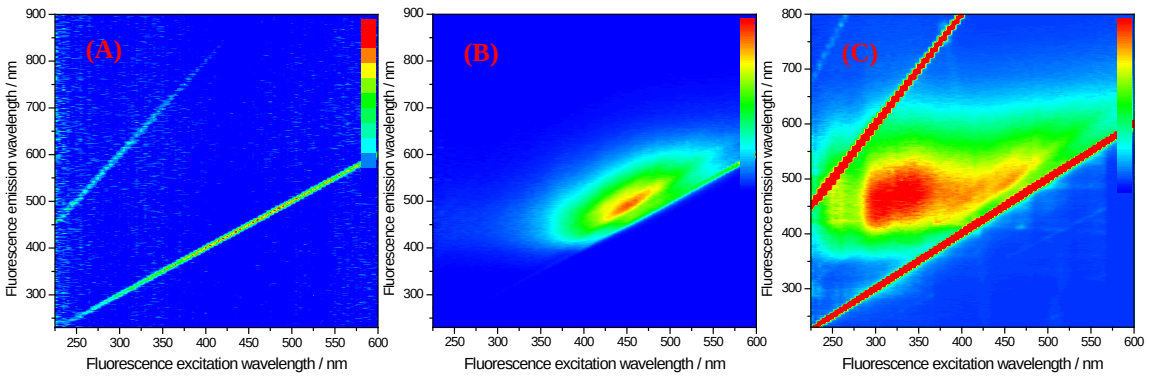

Figure 4.10 EEM spectrum of (A) neat crude oil collected with bifurcated fiber probe, (B) crude oil diluted in hexane collected with bifurcated fiber probe, (C) neat crude oil collected with quartz spacer-attached bifurcated fiber probe.

Because of the dead volume in front of the excitation fiber, the ability to record fluorescence from quite strongly absorbing samples such as crude oil is either limited or even impossible as in Figure 4.10 A. As may be expected, dilution in hexane did not improve capturing the fluorescence at short wavelengths, i.e. wavelength shorter than 500 nm and the only features may be attributed to Raman scattering (Figure 4.10 (B)). Finally, Figure 4.10 (C) shows how using fiber bundle with a quartz tip attached to the probe end improved the fluorescence collection efficiency even at shorter wavelengths.

4.5 Discussion

The calculation of fluorescence intensity according to the proposed model and the respective experiments led us to the following conclusions:

(i) Collecting fluorescence through fibers that surround the excitation fiber and have the same numerical aperture permits a large dynamic range of

concentration measurements and in a fluorescence EEM image is expected to yield the data array with the largest information content.

(ii) Because of the dead volume, the use of a fiber bundle to excite and collect fluorescence may limit the ability to record fluorescence from strongly absorbing samples.

(iii) The dead volume can be reduced by using claddingless fibers for fluorescence excitation and detection. It may be eliminated entirely by using a transparent spacer in front of the fiber bundle.

The effect of the dead volume in front of the excitation fiber was described in some detail before and gave rise to a number of improvements, including the use of double-clad fibers[135], beveling the fiber ends[125], using high-NA fiber[141], and the use of lenses[142, 143]. Indeed, the Monte Carlo simulation by Ozanyan et al.[141] generated collection efficiency data for a single-fiber configuration and a bifurcated fiber arrangement that are qualitatively and quantitatively very similar to the curves shown in Figure 4.7. In our study, we propose a simple solution in the form of a transparent silica or quartz spacer in front of the bundle. Attaching a tip to the distal end of the fiber probe strongly improves the overlapping of the excitation and emission fiber cones and, as a result, the detection efficiency increases.

5 Chapter 5. Contamination of Jet Fuel with Lubricant Oil*

5.1 Introduction

Aviation fuel specification, just as those of the jet turbine oil discussed above, have to meet very stringent requirements. Transfer and handling procedures are tightly controlled, not only to ensure the safety of the operators but also to assure the integrity of the fuel. In Canada and the USA, when jet fuel leaves the manufacture, it is certified according to ASTM D1655[144]. In addition, the fuel quality is checked also after arrival in the terminal. The guideline for monitoring fuel in the terminal and before fuelling is a set of ASTM test methods that examine the critical parameters of jet fuel, such as density[67, 145], distillation[146], flash point[147], freezing point[148], existence of gum[149] and finally contamination levels[13, 14, 95].

Any material that originally is not a part of the fuel composition is considered to be a contaminant. Contaminants such as water, antifreeze, other machinery fluids and gases are present at many points in the distribution chain and can find their way into aviation fuel during transfer and storage processes. Each time a transfer occurs, there is a large potential for contamination of the fuel to occur. As a result of contamination, engine and fuel system parts can be damaged. The cost can be considerable in terms of money,

* [Omrani, H.; Barnes, J. A.; Dudelzak, A. E.; Loock, H.-P.; Waechter, H., Fluorescence excitation-emission matrix (EEM) spectroscopy and cavity ring-down (CRD) absorption spectroscopy of oil-contaminated jet fuel using fiber-optic probes. *Analyst* 2012, *137*, 2782-2790.]-Reproduced by permission of The Royal Society of Chemistry.
http://pubs.rsc.org/en/Content/ArticleLanding/2012/AN/c2an35091b#!divAbstract

liabilities and engine down-time. In this chapter, we address the need to monitor jet fuel for contamination with engine lubricants.

5.2 Contamination

Contaminants in jet fuel can be divided in two main categories. Contamination that can be removed from fuel in the field consists of contaminants such as solid particulates and water that can be detected and partially separated from fuel using either a filter or a dedicated separation system. Other contamination cannot be easily removed and includes materials that are soluble in jet fuel such as other machinery fluids[1, 3]. The most common contaminants found in fuel are water, particulate matter, surfactants, microorganisms, coolants and other machinery fluids.

Water in jet fuel can occur in two forms; it may be dissolved and is then not of a great concern and it may be in the form of "free water", *i.e.* as part of an emulsion (which may even be stabilized by surfactant contaminants). There are a number of tests that may be carried out near the aircraft for the detection of water in fuel[11]. The other contaminants in the first category such as particulates can also be determined and removed with a set of robust standard tests[11].

Contamination of jet fuel with processed biofuels and with jet turbine lubricant oils is of great concern, since both contaminants can be dissolved in high concentrations and may affect the combustion properties as well as the fuel injection of the jet fuel. Bio

fuels are usually based on Fatty Acid Methyl Ester (FAME) stock, which has similar spectroscopic signatures as fuel and is difficult to distinguish from fuel.

Since jet fuel is often transported in multi-product pipelines and distribution systems, there is a high risk of cross-contamination of jet fuel with residual components from previously transferred fluids.

The soluble contaminants can also affect the freezing point of jet fuel and increase fuel waxing. At high concentrations FAME contamination can reduce the jet fuel's thermal stability and result in coke deposit in the fuel system. Moreover, some additives in lubricant oils may not be compatible with the fuel composition or the fuel system and may be harmful to the parts of the jet engine.

It is not possible to completely prevent fuel contamination during transport and storage, and on-site monitoring of jet fuel contamination is, consequently, a high priority for aviation safety. Detection and separation of machinery fluids, such as lubricant oils and biofuels, that are dissolved in jet fuel is much harder than the ones in the first category and, presently, they can only be quantified off-line[1, 3, 11].

In the current study, we focus on online monitoring of the contamination of fuel with lubricants and biofuels.

5.3 General Overview of the Experimental Work

As shown previously, absorption spectroscopy in combination with fluorescence and scattering measurements permits sensitive determination of lubricant quality metrics,

such as total acid number (TAN), phosphorus content, and the Joint Oil Analysis Program (JOAP) ‘‘anti-wear’’ index[120]. In this report, we demonstrate that fiber-based Cavity-Ring-Down (CRD) absorption spectroscopy together with fluorescence Excitation–Emission Matrix (EEM) spectroscopy can provide the information that is needed to detect and quantify contamination of jet fuel with lubricant oil. In chapter 1, the principles of both methods were explained in detail.

EEM spectra are typically generated by scanning the complete emission spectrum for each excitation wavelength over a specific range. The emission intensity as a function of both excitation and emission wavelengths can be presented in a contour plot or surface plot. The advantage of the EEM technique, combined with a multiway analysis method, is its ability to deconstruct the broad, overlapped bands characteristic for a single-line excited fluorescence spectrum into recognizable patterns, which can then be used as indicators for sample composition.

Cavity ring-down (CRD) absorption spectroscopy (CRDS) is a sensitive absorption technique for quantitative measurements of analytes in gas or condensed samples. CRD spectroscopy obtains its sensitivity from the enhancement of the optical loss measurement in a high finesse optical cavity and can be performed with either pulsed or continuous wave light sources. In CRDS not the absolute amount of absorbed light is measured, but the temporal decay of the intensity in the optical cavity is recorded. Fiber-Loop Cavity Ring-Down Spectroscopy (FLCRDS) is closely related to “regular” mirror-based CRDS, except that the optical cavity is build from a fiber waveguide loop. Equation (5.1) expresses the ring-down time as a function of the round trip time of the cavity, nL/c_0, and the transmission per round trip, T_{rt}.

$$\tau = \frac{nL}{c_0(-\ln T_{rt})} = \frac{nL}{c_0\left(-\ln T_{blank} + \sum_f \varepsilon_f C_f d_f\right)} \qquad (5.1)$$

Here, T_{blank} is the transmission per round-trip for a blank sample, n is the refractive index of the cavity medium, L is the roundtrip length, d is the length of the path through the sample with concentration C, and c_0 is the vacuum speed of light. The absorption coefficients of the analytes, ε, are given with respect to base e. In the experiments described below, the optical cavity consists of a loop made from multimode optical fiber and the interaction length with the sample, d, corresponds to the distance between the two fiber ends[63, 64]. In this case -ln T_{blank} = -ln T_{gap} + αL, where T_{gap} is the transmission across the gap in the absence of analyte and α is the absorption coefficient of the cavity medium.

5.4 Fuel Contamination with Turbine Oil

5.4.1 Experimental Set-up / Materials and Methods

5.4.1.1 Fluorescence Measurements

Fifty-two samples of JetA1 type fuel (Shell Corp.) mixed with jet turbine oil (NYCO, synthetic aviation turbine oil, MIL-PRF-23699 F Class STD) were included in this study. Samples were prepared at different concentration levels from 5 ppm_v to 1000

ppm_v. Neat jet fuel was used as a blank sample. The prepared samples were distributed between a calibration and a prediction set. Fluorescence measurements of all samples were completed with a spectrofluorometer (Varian, Cary Eclipse). The fluorescence excitation and emission were delivered using a bifurcated optical fiber bundle, which contains 6 multimode fibers for irradiation and 13 fibers for fluorescence collection (core/cladding diameters: 400/440 mm, CeramOptec). The end face of the fiber probe containing all 19 fiber ends is immersed in the sample material (Figure 3.1). The spectrofluorometer contains a pulsed xenon lamp and a red-sensitive photomultiplier tube as grating-coupled light source and detector, respectively. For each sample, the EEM spectrum was obtained in the emission wavelength range from 305 to 600 nm with a 1 nm increment, while the excitation wavelengths were stepped in the range of 300 to 363 nm in 3 nm increments. The bandwidth of both excitation and emission was 3 nm and PMT voltages and scan rate were set to 850 V and 21 nm s^{-1}, respectively.

5.4.1.2 Fiber-loop Cavity Ring-Down Measurements

Absorption measurements on 13 fuel samples with oil concentrations between 200 and 100,000 ppm_v were performed using a fiber-loop CRD setup as shown in Figure 5.1. The loop was formed from a multimode silica fiber (Fiber Optic Network Technology FONT, 440/400 μm) with a length of L = 11 m. A Nd:YAG laser at 355 nm (Spectra-Physics GCR-11, ~7 to 10 ns; power 20–50 mJ per pulse) and a photomultiplier tube (Hamamatsu R928) were used as light source and detector. To couple the light into the

loop, a fused fiber-fiber coupler (FONT) with a coupling ratio of 99 : 1 was used. The fiber-loop was closed using a micro-cross (Upchurch, P-729 PEEK cross) as an interface between the fiber optic cables and the capillary containing the liquid.

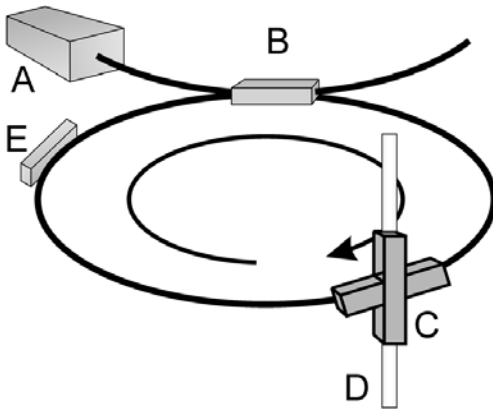

Figure 5.1 Schematic of the fiber-loop cavity ring-down setup.
355 nm light from the third harmonic of a Nd:YAG laser (A) is coupled into a 99 : 1 fiber-fiber coupler (B) and then circulates in the loop. With every roundtrip the pulse interacts with the liquid sample that is introduced into a microcross (C) using a capillary (D). Light scattered form the loop is detected with a photomultiplier tube (E).

The gap between the fiber ends (d = 200 mm) created a detection volume of 25 nL. The samples were delivered into the gap using a sample injector (Rheodyne 7725; injection volume: 20 μL). To detect the scattered light from the fiber, a small part of fiber was uncoated and placed on top of the PMT detector.

5.4.2 Experimental Results and Discussion

5.4.2.1 EEM Spectra and Analysis

Typical EEMs corresponding to pure fuel and to oil at a 1000 ppm_v concentration in fuel are shown in Figure 5.2 together with emission and excitation spectra, which were extracted from these matrices by integration over the entire excitation and emission wavelength range.

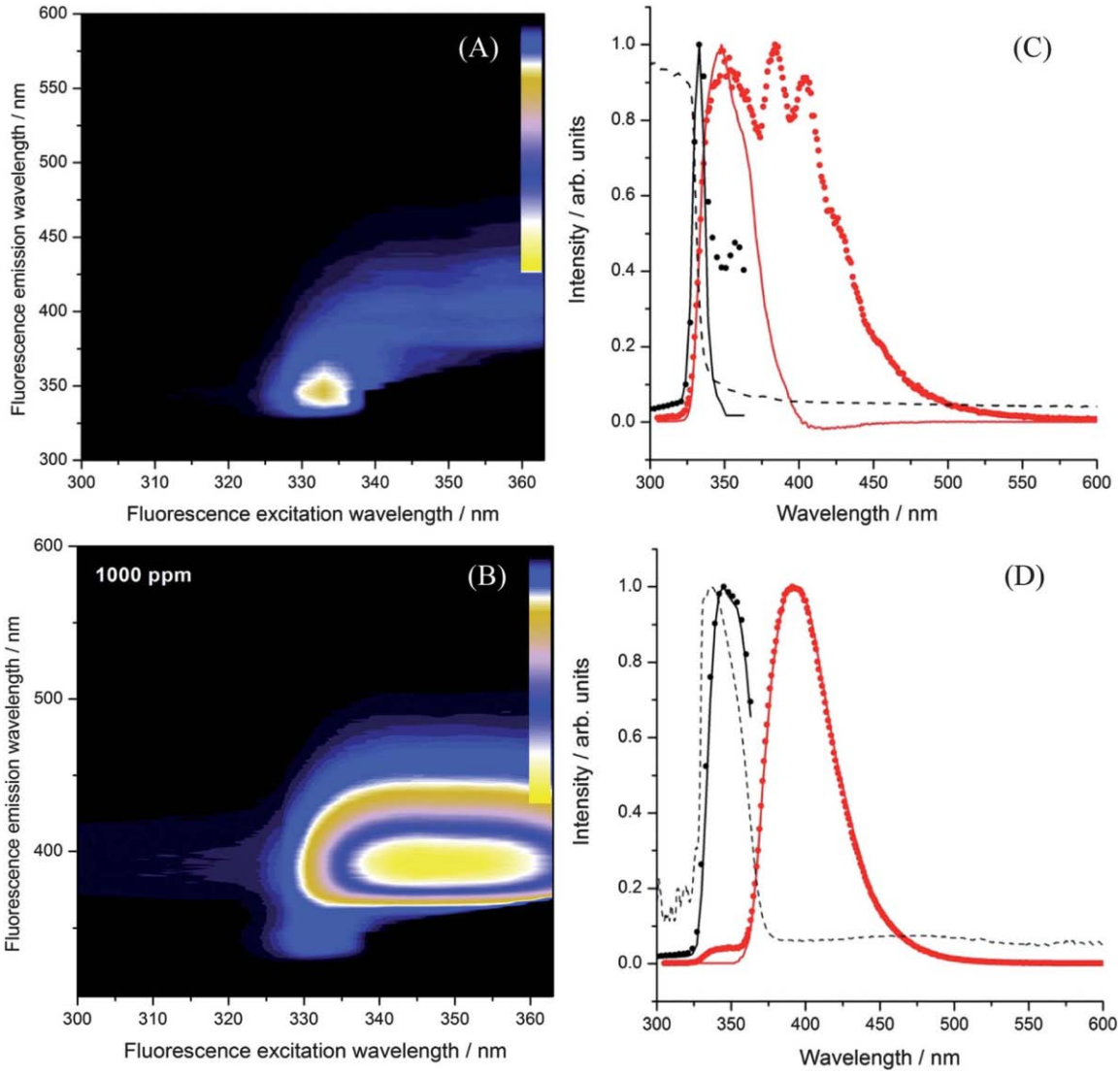

Figure 5.2 Excitation–Emission Matrix Spectra of (A) neat jet fuel and (B) jet fuel containing 1000 ppmv of jet turbine oil.
The colour bars on the right of each panel indicate the colours associated with low intensity (top) to high intensity (bottom). In the right panels the excitation spectra are obtained by integrating the experimental EEM spectra over all emission wavelengths (black dots) and the emission spectra by integrating over all excitation wavelengths (red dots). The respective solid lines are integrated spectra of component 1 (C) and component 2 (D) from the PARAFAC analysis. The dashed lines are absorption spectra recorded using a 1 cm cuvette.

Neat fuel fluoresces in the range from about 340 and 355 nm, when it is excited between 330 nm and 335 nm. A weaker emission feature is observed between 380 and 420 nm following excitation at 340 to 380 nm (Figure 5.2 (A)). Neat oil shows two broad

emission peaks centred at wavelengths of 410 nm and 550 nm. Fluorescence at 410 nm is caused by a tri-modal absorption spectrum with peaks at 250, 350 and 380 nm, whereas the fluorescence at longer wavelength is initiated by absorption at 410 nm. The EEM spectrum of oil diluted in fuel is much simpler and exhibits a dominant absorption feature at 340– 355 nm and a broad fluorescence band centred at 400 nm (Figure 5.2 (B)). EEM spectra of oil and fuel therefore overlap to some extent. It is not possible to scale the fluorescence EEM spectrum of neat oil to low concentrations, since quenching effects and re-absorption of fluorescence make a linear extrapolation impossible.

Figure 5.3 shows the EEM spectra of nine samples containing between 5 ppm_v and 650 ppm_v of jet turbine oil. It is apparent that even at the level of 10 ppm_v the EEM spectra show an enhancement of the long wavelength feature, and that quantitative concentration measurements at the low ppm level should be possible. The intensity scales for the EEM spectra in Figure 5.2 (A) and (B) and Figure 5.3 are identical and, by inspection, it is apparent that the EEM spectra may as a first approximation be understood as a linear combination of the two features corresponding to ‘‘oil’’ and ‘‘fuel’’, i.e. wavelength shifts, self-absorption or quenching do not appear to be strong. A more thorough analysis of the component contributions showing slightly non-linear behaviour at high concentrations is given in section 5.4.2.2 below.

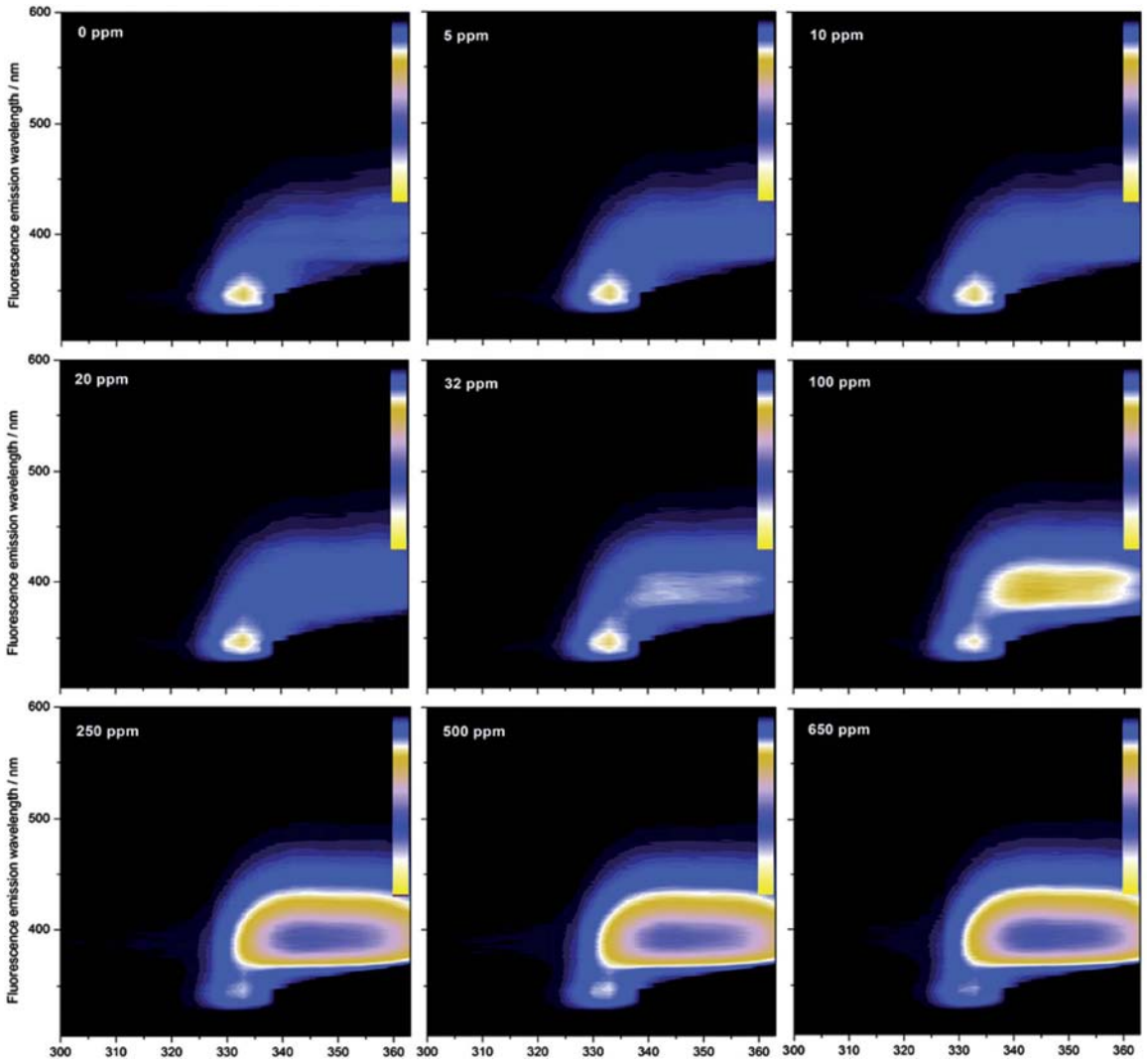

Figure 5.3 Selection of Excitation–Emission Matrix Spectra of jet fuel containing the indicated amount of jet turbine oil. In total 52 of these 2-dimensional spectra were recorded.

5.4.2.2 Parallel Factor (PARAFAC) Analysis

The excitation and emission profiles of the main components in the fuel/oil mixtures were extracted from 52 EEM spectra (20 spectra in the calibration set and 32 in the prediction set) by applying the PARAFAC analysis procedure. The PARAFAC model was implemented in Matlab ver 7.10.0 using the *n*-way toolbox provided by Andersson

and Bro[116]. The calculation of core consistency and residual indicated that a two-component model provides the best fit to our samples. The selection of the number of components and calculation of, both, the core consistency percentage and the residuals is done by the software and the decision was made by repeatedly applying the PARAFAC model using between 1 and 5 components. The stability of the model was tested using the validation dataset.

The PARAFAC model yields integrated emission and excitation spectra for both components. Comparison with the experimental integrated emission and excitation spectra for fuel (Figure 5.2 (C)) and 1000 ppm_v oil in fuel (Figure 5.2 (D)) indicates that the two PARAFAC components can indeed be correlated to the fuel and oil constituents. While the excitation and emission spectra for oil show excellent agreement with the PARAFAC component 2, there are noticeable differences between the experimental spectra for fuel and those predicted by the model for component 1. In both, excitation and emission spectra of neat fuel, the long-wavelength features are not well reproduced. We suspect that the PARAFAC procedure attributes those features to component 2 (oil), which indeed shows maxima at these longer wavelengths. From this observation, we expect that the model predicts a finite amount of component 2 even in pure fuel.

The scores of the two components were extracted separately for the calibration set and the prediction set and are shown in Figure 5.4. The two scores are inversely correlated and show the expected negative slope.

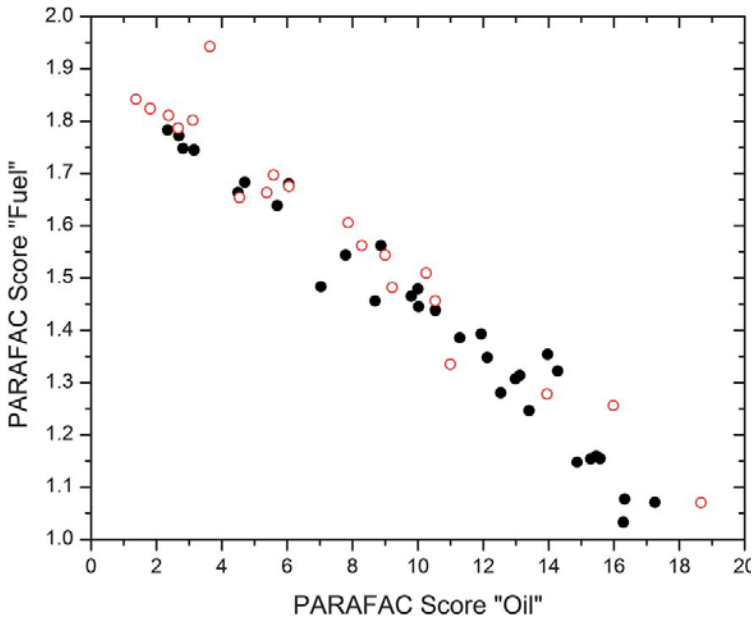

Figure 5.4 PARAFAC scores of the component 1 (fuel) and component 2 (oil).
The empty circles were extracted from the 20 samples in the calibration set and the solid points correspond to the 32 EEM spectra of the prediction set.

Scores for the calibration set and prediction set were also correlated to concentration (Figure 5.5). The scores are scattered and not well described by a linear correlation to concentration, possibly due to fluctuations in the excitation and emission intensity, but also due to fluorescence re-absorption.

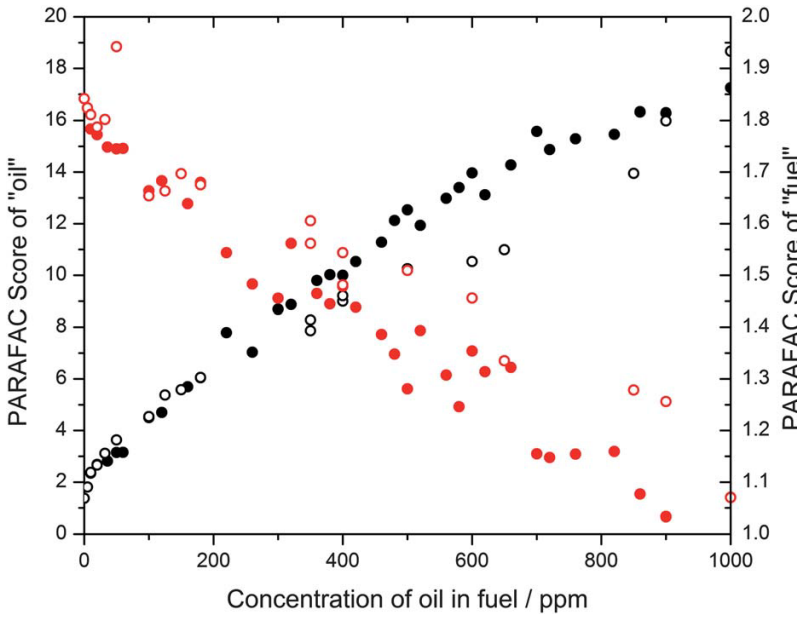

Figure 5.5 PARAFAC scores of components ‘‘oil’’ (black) and ‘‘fuel’’ (red) as in Figure 5.4, but as a function of concentration of oil in fuel.
The calibration set is indicated with open circles, whereas the prediction set is shown as solid circles.

On the other hand, the ratio of the scores (score of oil/score of fuel), which is independent of intensity, shows a strong linear correlation to concentration (R^2 = 0.95) and permits the construction of a linear calibration curve (Figure 5.6(A)). Even the contribution of fluorescence re-absorption, which is already reduced by collecting fluorescence at 180 degrees, should not affect the ratio of scores as long as the fluorescence intensity of both components is attenuated by the same fraction.

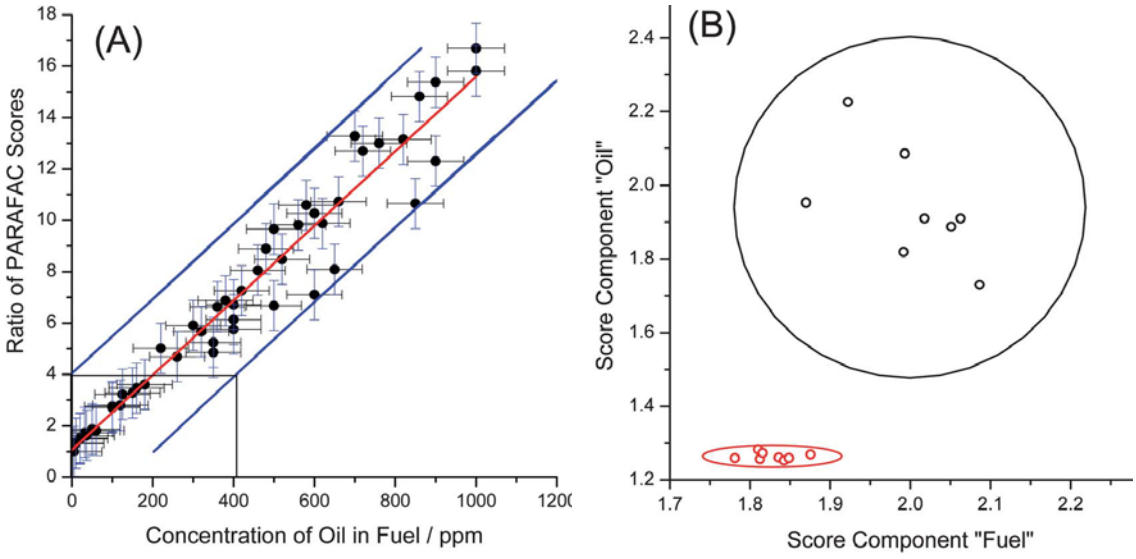

Figure 5.6 (A) Calibration curve from all 52 samples analysed by the PARAFAC model. (B) PARAFAC scores obtained from the EEM spectra of neat fuel (red circles) and 10 ppm_v oil in fuel (black circles). (A) The vertical error bars were assumed to be constant and obtained as in ref. 33. The red line is the result of a linear least squares fit, whereas the blue lines are the limits of the 99% confidence interval. (B) PARAFAC analysis of 8 samples at 10 ppm_v. The ovals indicate the 99% confidence limit and their lack of overlap shows that the samples can be readily distinguished.

Using the equations by Currie and Svehla[150] and the spreadsheet described by Wentzell and Loock[151] we determine that a measured score ratio of 4 corresponds to a concentration (410 ppm_v) that is with 99% confidence larger than that of the neat fuel. This value is not the true detection limit, however, since it is assumed that the uncertainty of the measured ratio is constant for all concentrations. This assumption of a constant error is incorrect as is shown by the reduced scatter of the measurements at low concentrations. Instead, the detection limit has to be determined by repeated measurements at low oil concentrations.

EEM measurements and PARAFAC analysis of 8 independently prepared samples at 10 ppm_v and of 8 neat fuel samples demonstrate that even this low level of contamination may be distinguished from neat jet fuel and be quantified (Figure 5.6(B)). The ratio of PARAFAC scores is 0.97(0.10) for the 10 ppm_v samples and 0.69 (0.01) for

neat fuel, where the values in brackets indicate one standard deviation. When setting the decision threshold at the 10 ppm_v level, the likelihood that an average of 8 measurements would result in a ‘‘false positive’’ measurement, is about one in one hundred.

From Figure 5.6, it is apparent that a simple fiber-coupled EEM sensor has the potential to identify and quantify the contamination of jet fuel with jet turbine oil at levels of 10 ppm_v and higher.

5.4.2.3 Principal Component Analysis and Regression

A related analysis model is presented by Principal Component Analysis (PCA) and Regression (PCR). Since the collected EEM data is arranged in a 3D-matrix, the first step consists of a process in which the data is reduced to a lower dimension[44,119]. The unfolding process can be understood as the re-arrangement of the 3D data cube into a product of mutually orthogonal 2D-data arrays. Here, the 3D-EEM spectra of all 20 calibration and 32 prediction samples were truncated, applying PCA, in a Matlab environment (ver. 7.10.0). As shown in Figure 5.7 scree plots for calibration and prediction sets indicate that 5 components are sufficient to describe the dataset (98% of variance is explained).

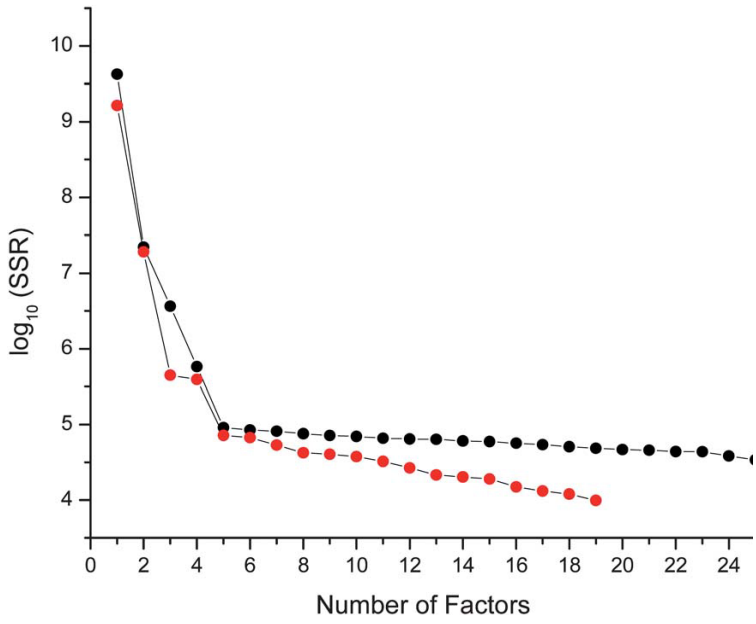

Figure 5.7 Scree plot showing the logarithm of the sum of squares of the residual, as a function of the number of factors for the calibration sample set (red) and the prediction set (black).

The calculated regression vectors from the calibration set were applied to the unfolded EEM data of, both, the calibration and the prediction sets to determine the concentration of oil in fuel. Figure 5.8 represents the result of the PCA/PCR process and shows as a linear fit the concentration that the model predicts. The slope for the combined set is 0.998 ± 0.02 with a squared correlation coefficient of $R^2 = 0.978$. Again, using the confidence intervals of the linear fit in Figure 5.8, the oil concentration, that falls with 99% certainty outside the confidence interval (272 ppm_v for the combined set) is higher than the actual detection limit (10 ppm_v) but consistent with the results of the PARAFAC analysis which was determined to be 410 ppm_v from the linear fit in Figure 5.6A.

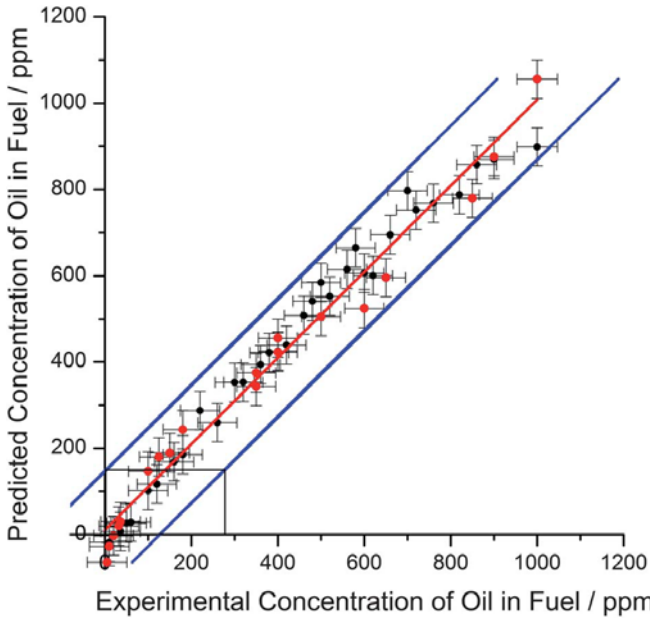

Figure 5.8 Result of the PCA/PCR analysis. 20 EEM spectra of the calibration set (red) and 32 EEM spectra of the prediction set.
The data were analysed using 5 factors and the regression obtained from the calibration set. The linear fits for both datasets agree well and fall on top of the linear least square fit for the combined EEM dataset (red line, $R^2 = 0.978$; slope 0.998 ± 0.02). A concentration of 272 ppm_v is with 99% confidence larger than that of a blank jet fuel sample (blue lines).

It appears that both analysis procedures, PARAFAC and PCA/PCR, are equally robust for the present dataset and give similar results. One may consider as an advantage of the PARAFAC analysis, that the ‘‘factors’’ or ‘‘components’’ have a physical meaning, *i.e*. the EEM spectra of the two components are closely related to those of the two constituents of our mixture. By comparison, the components in the PCA/PCR analysis are not related to the chemical components of the mixture.

5.4.2.4 Fiber-loop Cavity Ring-Down Spectroscopy

Samples at 13 different concentrations of jet turbine oil in jet fuel ranging from 200 ppm_v to 100 000 ppm_v (10%) were injected into the 25 nL gap between two ends in a multimode fiber-loop. The decay of a 7 ns laser pulse at 355 nm is measured. This wavelength was chosen because fuel is largely transparent at this wavelength, whereas oil absorbs strongly (see Figure 5.2). Figure 5.9 presents the waveform obtained when the gap is filled with a blank solution containing neat fuel.

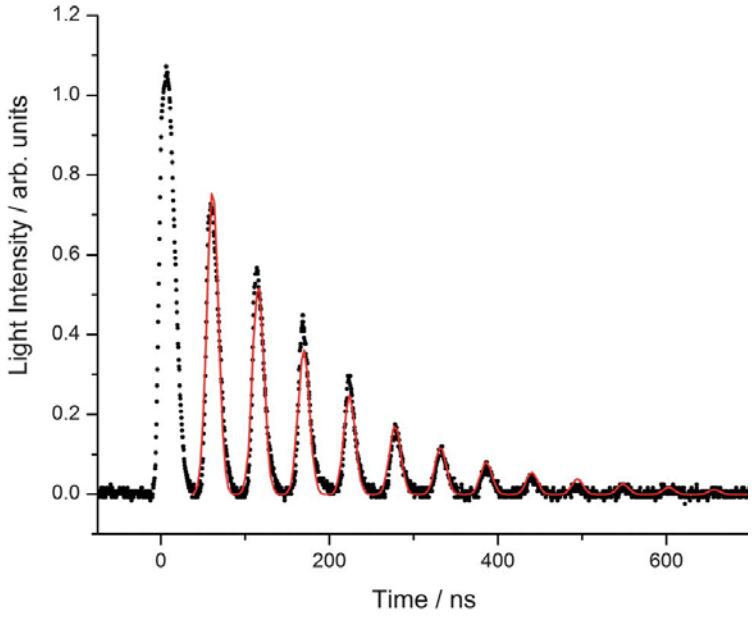

Figure 5.9 Ring-down of a ~7 ns laser pulse in a fiber-loop cavity (black circles). The data are fit with a pulse train of Gaussian functions with exponentially decreasing intensity (red line).

The intensities were fit using a single exponential decay and Gaussian functions with constant widths for each peak. Since the first peak contains a considerable amount of scattered light, it is very strong and saturates the PMT. It was therefore excluded from the fitting routine. Similar measurements have been completed for the 13 oil-contaminated fuel samples (Figure 5.10).

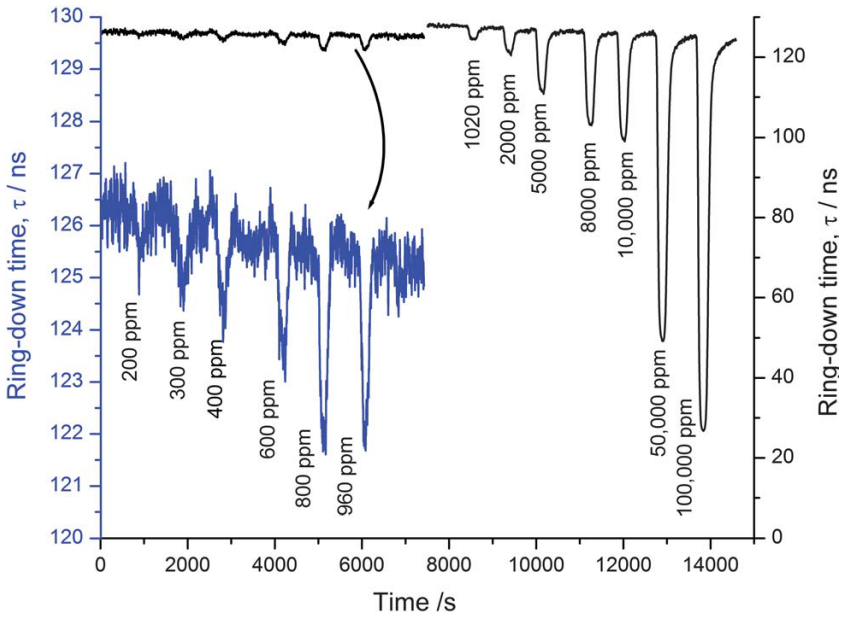

Figure 5.10 Ring-down times of the fiber-loop cavity as 20 µL samples with varying concentration of oil in fuel are injected. The enlarged portion of the curve is plotted against the left axis.

The samples were injected in 20 µL plugs and the detection limit (390 ppm_v) was obtained by measuring the concentration at which the ring-down time signal differs by more than three standard deviations from the baseline. The repeatability of the measurements was tested using 10 identical injections of 2000 ppm_v oil in fuel (not shown). At this concentration the ring-down time changed by 5.0 ± 0.2 ns compared to that of neat fuel.

After rearranging Equation 5.1 the inverse of the ring-down time can be expressed as a linear function of the oil concentration in fuel (Equation (5.2)).

$$\frac{1}{\tau_{sample}} = \frac{c_0}{nL}\varepsilon dC + \frac{1}{\tau_{blank}} \qquad (5.2)$$

Here, the length of the fiber-loop, L = 11 m, the width of the gap, d = 200 μm, and the speed of light in the fiber c_0/n = 2.07 × 10^8 m s^{-1}. From the slope of the calibration curve in Figure 5.11 (279 s^{-1} ppm_v^{-1}), we determine the absorption coefficient as ε = 7.44 ± 0.08 × 10^{-4} ppm_v^{-1} cm^{-1} to base e. An absorption spectrum of 1000 ppm_v of oil in fuel recorded using a conventional absorption spectrometer shows a decadic absorption coefficient of 3.37 × 10^{-4} ppm_v^{-1} cm^{-1}, corresponding to 7.75 × 10^{-4} ppm_v^{-1} cm^{-1} given with respect to base-e in good agreement with the values from fiber-loop CRD spectroscopy. The 4-5% difference is likely due to the uncertainty in the gap width, d.

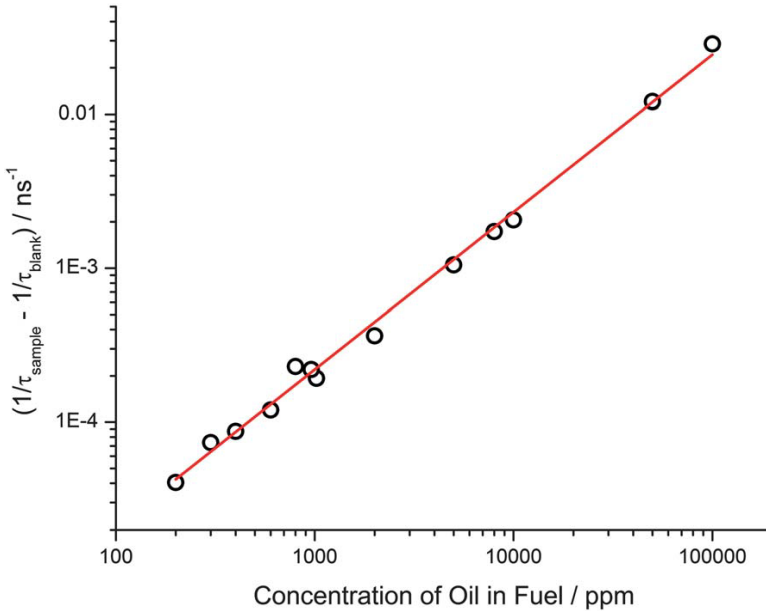

Figure 5.11 Calibration curve showing the inverse of the ring-down times obtained from the data of Figure 5.10.

5.4.3 Discussion and Conclusion

We used two different types of fiber optic probes to determine the concentration of oil in fuel. The fluorescence EEM spectra were analysed in two different ways, *i.e.* by PARAFAC and PCA / PCR giving calibration curves with very similar properties and a measurement range from about 10 ppm_v to 1000 ppm_v. The PARAFAC analysis technique demonstrated that the EEM spectra may be understood as arising from only two components (five components when using PCA/PCR) and that, up to 1000 ppm_v, their ratio is linearly correlated to the concentration. At higher concentrations, we expect that quenching and other nonlinear effects contribute and more components would be required.

The absorption measurements were performed on small sample volumes of 20 μL and with a detection volume of only 25 nL. Since the absorption measurements were conducted at only one wavelength, we were not able to identify the spectral signatures of the oil sample. The detection limit of the CRD method was about 390 ppm_v with a dynamic range that extended to 100 000 ppm_v (10%). When combining both fiber-coupled techniques, one should therefore be able to identify and quantify contaminants at low concentrations by fiber-coupled EEM spectroscopy while measuring their concentrations at selected wavelengths up to 10% concentrations using fiber-coupled absorption spectroscopy.

Aside from the simple optical configuration, the fiber-coupled EEM method furthermore permits *in situ* sampling of the fuel, *i.e.* identification of contaminants without removal of the sample. We note that this method may be useful when monitoring the contamination of any corrosive, inflammable or explosive liquid, including jet fuel, of course. The present methods should be readily extendable to mixtures of more than two

components. We then expect PARAFAC analysis to be particularly useful as it permits us to quantify and possibly identify the different components in the mixture. Fiber-coupled absorption measurements may have to be extended to multiple wavelengths.

5.5 Fuel Contamination with FAME

FAME, which is the main constituent in biodiesel, is produced through the chemical reaction transesterification of biologically derived triglycerides with methanol. Triglyceride molecules in vegetable oil or animal fat react with methanol to produced methyl ester of fatty acids. As mentioned above, FAME is considered to be a contaminant in jet fuel and the presence of FAME in the fuel system may cause serious problems.

5.5.1 Experimental Set-up / Materials and Methods

A biodiesel fuel, Canola Methyl Ester (CME), containing 99% FAME (provided by Environment Canada) is mixed with jet A1 fuel to make solutions with concentration varying from 400 ppm_v to 100,000 ppm_v of biodiesel in fuel. The same fiber-coupled EEM set up as in the 5.4.1.1 was used to collect data.

In addition, fluorescence spectra (produced at a single excitation wavelength) of the jet fuel samples contaminated with CME were collected. The CME concentrations varied from 100 ppm_v to 2000 ppm_v. To excite the samples, a laser diode (Nichia

Corporation NDHV310APC, CW, maximum power 60 mW) emitting at 405 nm was used. The bifurcated fiber probe was coupled to the laser diode and an Ocean Optics spectrometer that was used to collect the fluorescence spectrum in the range from 620 nm to 800 nm.

Also, the EEM spectra of three more biodiesel fuels - Soy Methyl Ester (SME), Fish Methyl Ester (FME), and Beef Methyl Ester (TME) all provided by Environment Canada - were collected.

5.5.2 Experimental Results and Discussion

The EEM signatures of both neat fuel and CME were collected in order to find a spectral window, within which the fuel would not have any pronounced absorption or excitation/emission features, and where FAME would have a strong absorption followed by intense fluorescence. According to Figure 5.12, FAME fluoresces around 675 nm when excited in a narrow window from 350 nm to 425 nm. Pure fuel shows weak fluorescence bands in this absorption window that peak at 400-500 nm (see section 5.4.2.1 and Figure 5.12); thus, FAME can be distinguished from jet fuel.

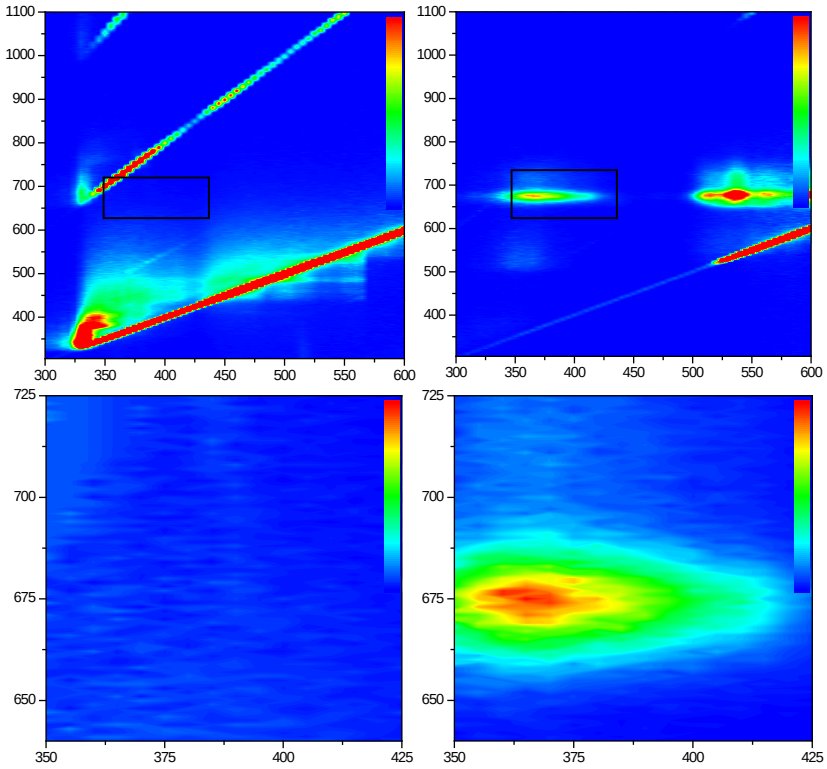

Figure 5.12 Comparison of EEMs of neat fuel (left) and neat FAME (right). Collected EEM of the highlighted rectangular area (Bottom).

Figure 5.13 illustrates the EEMS capability of detecting FAME contamination of jet fuel down to concentrations of about 400 ppm_v.

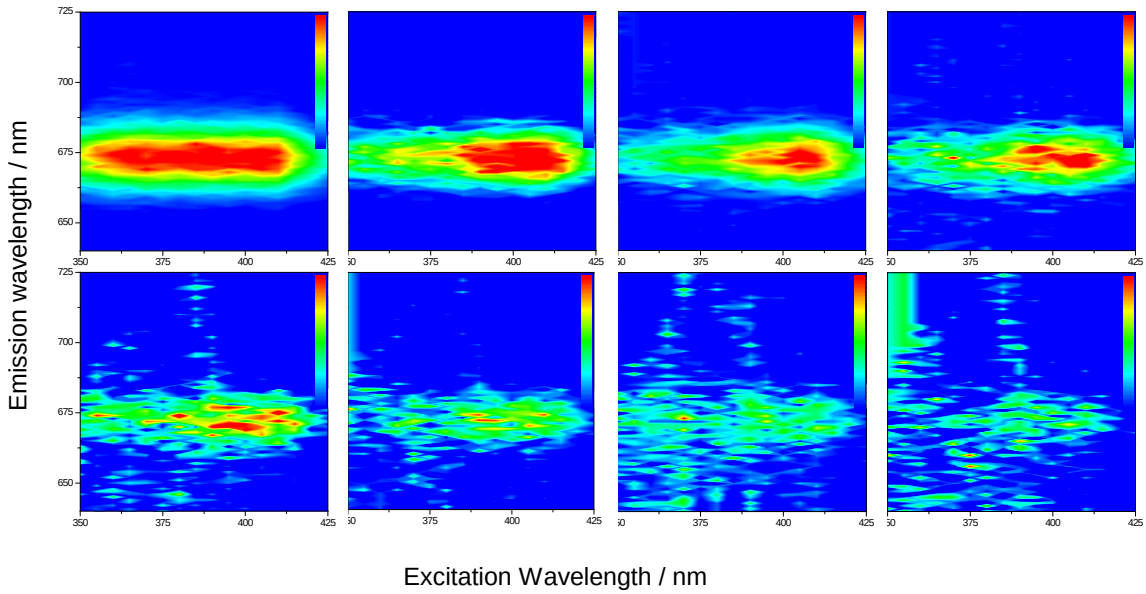

Figure 5.13 EEM signatures of fuel/FAME samples with different concentrations, from left to right (First row: 100,000, 10000, 5000 and 2000 ppm_v. Second row: 1000, 800, 600 and 400 ppm_v.

As it is obvious in Figure 5.13, the maximum fluorescence is shifted to the longer excitation wavelengths as the concentration of FAME in fuel decreases. Since fuel absorbs strongly at wavelengths shorter than 380 nm, we observe this red shift of excitation signal in dilute FAME mixtures. The aim in the aviation industry applications is to detect and analyze FAME contamination down to the 5 ppm concentrations while the decision-making threshold is 100 ppm. Analytical methods such as Gas Chromatography- Mass Spectrometry (GC-MS) and Fourier transform infrared spectroscopy (FTIR)[152] currently are used as industry-accepted methods for FAME detection. However, these methods are difficult and expensive whereas fluorescence measurements are easy to make and suitable for online/inline monitoring.

To decrease the limit of detection toward the lower concentrations, one may use a single-line intense and powerful light source in the region with least signal interference.

Figure 5.14 shows the correlation between the related fluorescence intensity at 675 nm corresponding to the excitation wavelength at 405 nm and the concentration of FAME in each sample.

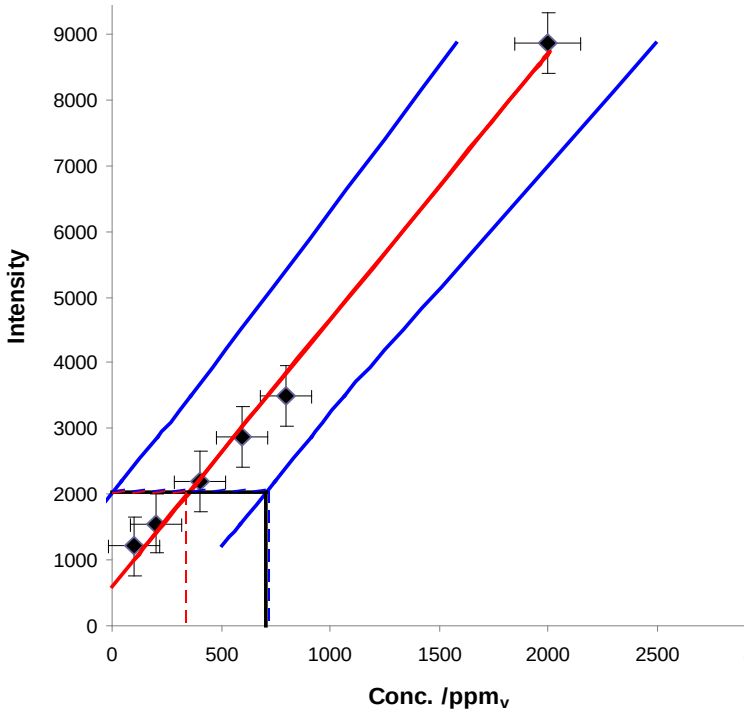

Figure 5.14 The linear fit for determination of FAME in jet fuel. (R^2 = 0.994)
The red line is a linear fit to the data and the blue lines are 99% confidence intervals. The analysis was performed as described in reference 151.

The fluorescence peaks with a maximum at 675 nm (excitation ranges: 325 nm – 425 nm and 500 nm – 600 nm) was suspected to be the result of chlorophyll that is present in biodiesel fuel[153] (Figure 5.12). Extracting chlorophyll is a major issue in biofuel supply; rarely is it possible to remove all chlorophyll. If all biofuel products fluoresce in the same range, chlorophyll could be the key emission signal in all biofuel spectra. To check upon that, FAME samples of animal-fat origin were examined using

EEMS, as well as another vegetable source. Figure 5.15 represents EEM signatures of two different animal fat-based biofuel samples:

- beef methyl ester (TME), and fish methyl ester (FME);

as well as and two vegetable fat-based samples:

- canola methyl ester (CME), and soy methyl ester (SME).

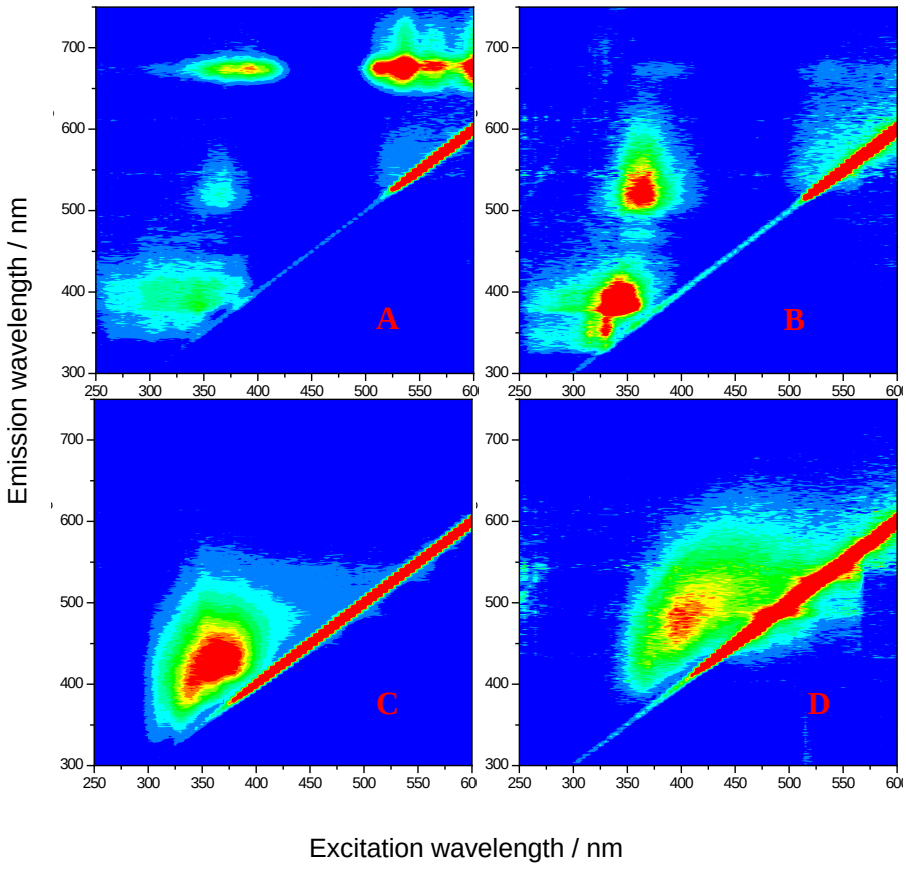

Figure 5.15 EEM signature of (A) canola methyl ester, (B) soy methyl ester, (C) beef methyl ester and (D) fish methyl ester.

This study has demonstrated that the EEM signatures of FAME vary depending on the biofuel origin, i.e. the source of fat from which the biofuel was produced. The fluorescence feature around 375 nm, which is observed in the EEM signatures of CME, SME, TME and - very weakly - in FME, is partially overlapped with the fluorescence

EEM signature of jet fuel. The additives added to the biofuels' base stock, e.g. antioxidants with aromatic structure, are suspected to be responsible for the observed emission signal. In practice, fuel is typically contaminated with FAME traces of different origins, which are simultaneously present in the same tested sample. While the EEM technology allows identifying quite confidently the fact of the jet fuel contamination with FAME, quantitative contamination analysis is impeded by the fact that concentrations of FAME contaminants of different origins in the fuel system also vary randomly. Developing a confident calibration model may require involving a combination of measurement techniques in a possible study continuation.

With the technique we used, it was possible, in principle, to achieve a limit of detection that is below the required ≈100 ppm level. However, we did not continue with the study because the aviation industry had meanwhile found a different way of controlling the FAME contamination. To the best of our knowledge a new method is now used to eliminate the FAME contamination threat altogether.

6 Chapter 6. Summary and Future Work

6.1 Conclusion

Real-time monitoring of lubricant conditions addresses a large need in the aviation and energy industry. Lubricants quickly oxidize as soon as their antioxidant additives are consumed, yet oxidation stability is typically measured off-line in a process that is prone to producing false positives. As was demonstrated in Chapter 3, we were able to identify spectroscopic signatures that allowed us to determine antioxidant concentrations. It was shown that excitation emission matrix fluorescence spectroscopy is capable of monitoring the amount of antioxidants in jet turbine oil. Briefly, this project resulted in finding spectral features that can be used to examine lubricants to determine their oxidative stability. While Total Acid Number (TAN) and breakdown-numbers appear not to be reliable parameters that can be a single-meaning, online, real-time indicator for the lubricant's condition, our fluorescence method was much more robust. Using multivariate analysis of fluorescence EEM spectra that were taken at regular time intervals, we have characterized fluorescence spectra of fresh and aged oil, found spectral markers indicative of the antioxidant levels and were able to correlate the fluorescence from these markers to the oxidation stability of the oil. All lubricant base stocks, saturated or ester type, have high-lying excited states and therefore are non-fluorescent in the 250-450 nm region. Conversely, all anti-oxidants should exhibit some degree of fluorescence in that region, because of their aromatic structure and conjugated systems (or metal centers) that

are required for their function as radical scavengers. Antioxidant fluorescence is therefore a good quantitative indicator for oxidative stability.

In order to reduce the effects of fluorescence re-absorption by the high optical density of the lubricants, the detection geometry is limited to front face detection. To decrease fluorescence re-absorption and also to reduce stray-light background, we collected the fluorescence emission anti-parallel to the irradiation. Furthermore, a fiber optic probe was developed that can be submersed in the oil sump of a running engine to produce online measurements of antioxidant concentrations. The fiber optic probe was designed, built, and fully characterized[118]. It was shown conclusively, through simulations and experiments, that fluorescence measurements in strongly absorbing samples is best conducted using co-axial excitation and fluorescence detection, i.e. by detecting fluorescence in a front-face geometry. When using fiber bundles one needs to fully overlap the excitation and emission volumes, which is done easiest by inserting a transparent spacer between the fiber end faces and the sample liquid.

It was also demonstrated how fluorescence EEM spectroscopy together with fiber-loop CRD measurements and complemented by multivariate data analysis, were innovatively used to identify the contamination of jet fuel with turbine oil[7]. Calibration curves were generated using two different chemometrics analysis methods. They showed that, with fluorescence detection, it is possible to determine the concentration of lubricant oil contamination in jet fuel from about 10 ppm_v to 1000 ppm_v. The CRD measurements conducted at UV wavelength resulted in a calibration curve from the detection limit of 390 ppm_v with a dynamic range extended to 100,000 ppm_v. Using the combination of two optical techniques provided a detection range from 10 to 100,000 ppm_v.

In its entirety, this thesis opens the opportunity to design on-line sensors for the continuous assessment of the machinery fluids. Data acquisition can be performed by means of compact fiber-coupled optical instruments and multivariate signal processing can be conducted with a suitably programmed laptop computer.

6.2 Future Work

In addition and beyond the immediate demands of machinery fluid quality control, there is potential for a new set of products to be designed and manufactured. These products are anticipated to be compact and real-time spectroscopic sensors. In order to perform online determination of machinery fluids contamination and degradation, advanced fiber-coupled EEMS and CRD technologies would be very useful.

6.2.1 Multiline Fluorescence EEM Spectroscopy

Typical commercial EEM fluorimeters are inefficient, large and expensive. They are also very wasteful of photons. The EEMS technique can be extended into a fast real-time method for the rapid analysis of oil lubricants. It is possible to make fluorescence EEM spectroscopy much faster and reduce the data acquisition time to a much shorter period, which is then much more convenient for real-time, kinetic measurements.

In an attempt to minimize the size of EEM fluorimeters together with fast collection of EEM spectrum, the following design is suggested. A set of small light sources with about 10-12 different wavelengths (LEDs and/or lasers) that are modulated individually will replace the white light source. The output of each light source should be coupled into a fiber bundle. Fluorescence will be detected using the same fiber bundle and guided to a compact monolithic array spectrometer (Ocean Optics or Avantes). A typical set of input wavelengths includes: LEDs 260, 280, 300, 330, 350, 380, 400, 420 nm; lasers 405, 445, 532, 630 nm). Additional wavelengths at 1370, 1480 and 1550 nm could serve to identify water contamination through absorption at its overtone wavelength of 1480 nm. The resulting EEM has a resolution that is high enough to follow the changing antioxidant concentrations and similar processes. Also the lubricant absorption can be readily measured and quantified, as it will affect each wavelength differently.

6.2.2 Fiber Probe Submersion in a Circulating Oil Apparatus and a Running Engine

In the present work thesis, the lubricant oil was aged in a round bottom flask that was heated to 150-220° C while bubbling air through the oil. The oil oxidized very quickly and at high temperatures the antioxidants were depleted after only a few hours. Large changes to the antioxidant concentrations at 195° C happened within the first 100 mins. While this process proved the validity of our method to determine oxidative

stability of oil, it would not let us examine the influence of catalytic surfaces, friction or exposure to combustion by products on the lubricant quality. We will therefore build an apparatus in which oil is circulated through a heated section and can be exposed to catalytic surfaces. The fiber optic probe will then be permanently submersed in the oil reservoir and measure EEM spectra every few seconds. It can be tested whether addition of antioxidants near the end of the normal lifetime can extend the oxidative stability of the lubricant. All these measurements will help to optimize the performance of the fluorescence sensor and will also give insights on the chemical kinetics of additives in lubricants. These kinetic measurements are currently performed in industrial research labs developing oil additives, but that expertise is not transferred to the public. By conducting these experiments in an academic lab, we can provide a better fundamental understanding of lubricant chemistry to aid future design of lubricity sensors.

6.2.3 Fiber Probe CRD Spectrometer to Define the Machinery Fluid Contamination

According to FTIR absorption spectra in the 2-3 μm region, for water detection in oil[2,71], one may also expect that CRD has potential as a method for analysis of oil samples in the mid-IR spectral region. In chapter 2, it was briefly explained that FTIR measurements are used to detect different type of contaminants in either oil or fuel (Figure 2.2- Figure 2.6). The FTIR spectra of diesel oil and fuel were also collected to find the potential wavelengths for detection of water as contamination (Figure 6.1).

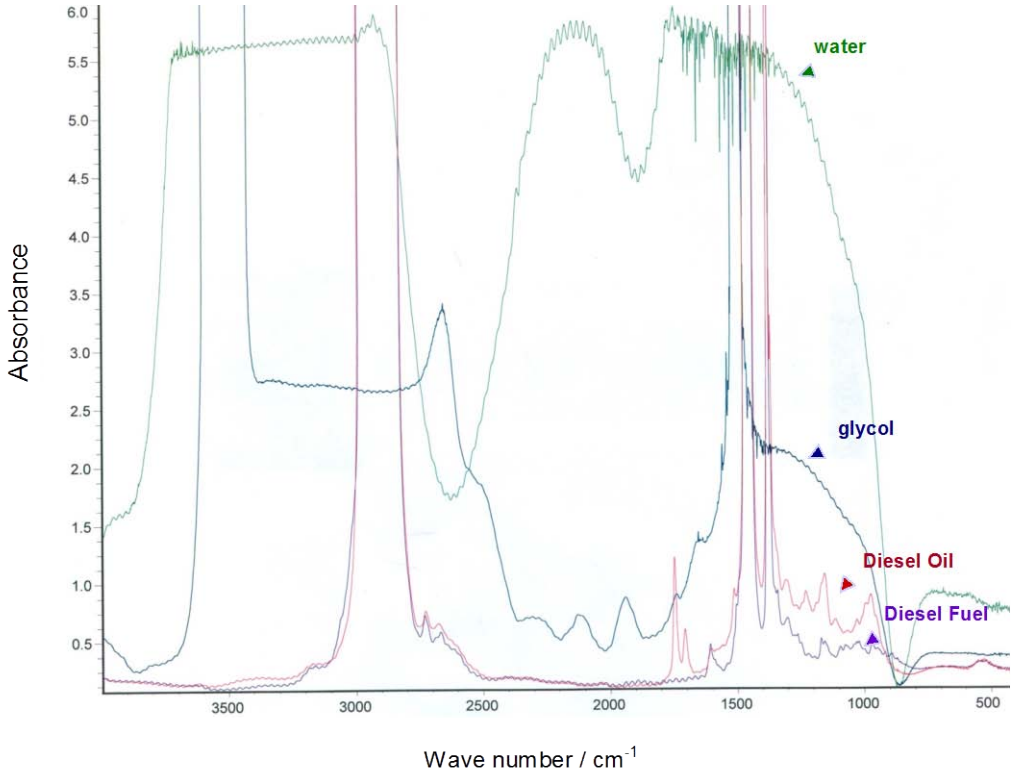

Figure 6.1 FTIR spectra of diesel oil, diesel fuel, water and glycol.

Fiber-coupled CRD absorption measurements may be extended to multiple wavelengths to quantify different contaminants in machinery fluids. According to previous FTIR studies[71], in order to build a prototype absorption sensor, a set of light sources is needed to cover a wide wavelength range, i.e. 3700-800 cm^{-1} (2.7-12.5 μm). To reduce complexity and cost, a large number of inexpensive light sources, each emitting light in a narrow, fixed wavelength range can be implemented.

References

1. Totten, G. E., *Fuels and Lubricants Handbook: Technology, Properties, Performance, and Testing*. ASTM International: 2003.

2. Toms, L. A.; Toms, A. M., *Machinery Oil Analysis: Methods, Automation & Benefits*. 3rd ed.; Society of Tribologists & Lubrication engineers: IL, USA, 2008.

3. Coordinating Research Council, *Handbook of Aviation Fuel Properties*. 3rd ed.; Society of Automotive Engineers: PA, USA, 2004.

4. Mortier, R. M.; Fox, M. F.; Orszulik, S. T., *Chemistry and Technology of Lubricants*. Third ed.; Springer: 2010.

5. Rudnick, L. R., *Synthetics, Mineral Oils, and Bio-Based Lubricants Chemistry and Technology*. Second edition ed.; CRC Press, Taylor & Francis Group: , 2013; p 992.

6. Rudnick, L. R., *Lubricant Additives Chemistry and Applications*. Second edition ed.; CRC Press, Taylor & Francis Group: , 2009; p 777.

7. Omrani, H.; Barnes, J. A.; Dudelzak, A. E.; Loock, H.-P.; Waechter, H., Flourescence excitation-emission matrix (EEM) spectroscopy and cavity ring-down (CRD) absorption spectroscopy of oil-contaminated jet fuel using fiber-optic probes. *Analyst* **2012,** *137*, 2782-2790.

8. Omrani, H.; Dudelzak, A. E.; Hollebone, B. P.; Loock, H.-P., Assessment of the oxidative stability of lubricant oil using fiber-coupled fluorescence excitation–emission matrix spectroscopy. *Analytica Chimica Acta* **2014,** *811*, 1-12.

9. Speight, J. G., *Handbook of Petroleum Product Analysis*. A JOHN WILEY & SONS, INC., PUBLICATION: Hoboken, New Jersey, 2002.

10. Omrani, H. *Fuel Contamination Research Summary*; GasTOPS Ltd.: Ottawa, January 2007.

11. Waite, R., *Aviation fuel quality control procedures*. second ed.; ASTM: Philadelphia, PA 1995.

12. ASTM, Standard test method for particulate contaminant in aviation fuel by line sampling. ASTM International: West Conshohocken, Vol. D2276.

13. ASTM, Standard test method for particulate contaminant in aviation fuel by laboratory filtration. ASTM International: West Conshohocken, Vol. D5452.

14. ASTM, Standard test method for undissolved water in aviation turbine fuels. ASTM International: West Conshohocken, Vol. D3240.

15. ASTM, Standard test method for sulfur in petroleum products by wavelength dispersive X-ray fluorescence. ASTM International: West Conshohocken, Vol. D2622.

16. Harris, D. C., *Quantitative Chemical Analysis*. 6th ed.; W. H. Freeman and Company: New York, 2003.

17. Rho, J. H.; Stuart, J. L., Automated three-dimensional plotter for fluorescence measurements. *Anal. Chem.* **1978,** *50* (4), 620-625.

18. Schachter, M. M.; Haenni, E. O., Automatic triparametric recording in fluorometry of polynuclear hydrocarbons. *Anal. Chem.* **1964,** *36* (10), 2045-2047.

19. Duarte, R. M. B. O.; Pio, C. A.; Duarte, A. C., Synchronous scan and excitation-emission matrix fluorescence spectroscopy of water-soluble organic compounds in atmospheric aerosols. *Journal of Atmospheric Chemistry* **2004,** *48*, 157-171.

20. Miller, T. C.; Faulkner, L. R., Computer assisted structural interpretation of fluorescence. *Anal. Chem.* **1976,** *48* (14), 2083-2088.

21. Johnson, D. W.; Callis, J. B.; Christian, G. D., Rapid scanning fluorescence spectroscopy. *Anal. Chem.* **1977,** *49* (8), 747A-757A.

22. Nahorniak, M. L.; Booksh, K. S., Excitation-emission matrix fluorescence spectroscopy in conjunction with multiway analysis for PAH detection in complex matrices. *Analyst* **2006,** *131*, 1308-1315.

23. Nahorniak, M. L.; Booksh, K. S., Optimizing the implementation of the PARAFAC method for near-real time calibration of excitation–emission fluorescence analysis. *Journal of Chemometrics* **2003,** *17*, 608-617.

24. Yan, Y.; LI, H.; Myrick, M. L., Fluorescence fingerprint of waters: excitation-emission matrix spectroscopy as a tracking tool. *Applied Spectroscopy* **2000,** *54* (10), 1539-1542.

25. Chen, W.; Westerhoff, P.; Leenheer, J. A.; Booksh, K., Fluorescence excitation-emission matrix regional integration to quantify spectra for dissolved organic matter. *Environmental Science & Technology* **2003,** *37* (24), 5701-5710.

26. Jiang, F.; Leea, F. S.-C.; Wanga, X.; Dai, D., The application of excitation/emission matrix spectroscopy combined with multivariate analysis for the characterization and source identification of dissolved organic matter in seawater of Bohai Sea, China. *Marine Chemistry* **2008,** *110*, 109-119.

27. Zhou, Z.; Guo, L.; Shiller, A. M.; Lohrenz, S. E.; Asper, V. L.; Osburn, C. L., Characterization of oil components from the Deepwater Horizon oil spill in the Gulf of Mexico using fluorescence EEM and PARAFAC techniques. *Marine Chemistry* **2013,** *148*, 10-21.

28. DaCosta, R. S.; Andersson, H.; Wilson, B. C., Molecular fluorescence excitation-emission matrices relevant to tissue spectroscopy. *Photochemistry and Photobiology* **2003,** *78* (4), 384-392.

29. Seetohul, L. N.; Islam, M.; O'Hare, W. T.; Ali, Z., Discrimination of teas based on total luminescence spectroscopy and pattern recognition. *Journal of the Science of Food and Agriculture* **2006,** *86* (13), 2092-2098.

30. Tóthová, J.; Žiak, Ľ.; Sádecká, J., Characterization and classification of distilled drinks using total luminescence and synchoronous fluorescence spectroscopy. *Acta Chimica Slovaca* **2008,** *1* (1), 265-275.

31. Tóthová, J.; Sádecká, J.; Májek, P., Total luminescence spectroscopy for differentiating between brandies and wine distillates. *Czech J. Food Sci.* **2009,** *27* (6), 425-432.

32. Airado-Rodriguez, D.; Galeano-Diaz, T.; Duran-Meras, I.; Wold, J. P., Usefulness of fluorescence excitation-emission matrices in combination with PARAFAC, as fingerprints of red wines. *J. Agric. Food Chem.* **2009,** *57*, 9.

33. Han, Q.; Wu, H.; Nie, J.; Xia, A.; Zhu, S.; Yu, R., Direct determination of reserpine in urine using excitation-emission fluorescence combined with three-way chemometric calibration methodology. *Front. Chem. China* **2008,** *3* (2), 224-228.

34. Ortiz, M. C.; Sarabia, L. A.; Sanchez, M. S.; Gimenez, D., Identification and quantification of ciprofloxacin in urine through excitation emission fluorescence and three-way PARAFAC calibration. *Analytica Chimica Acta* **2009,** *642*, 193-205.

35. Patra, D.; Mishra, A. K., Study of diesel fuel contamination by excitation emission matrix spectral subtraction fluorescence. *Analytica Chimica Acta* **2002,** *454*, 209-215.

36. Divya, O.; Mishra, A. K., Multivariate methods on the excitation emission matrix fluorescence spectroscopic data of diesel-kerosene mixtures: A comparative study. *Analytica Chimica Acta* **2007,** *592*, 82-90.

37. Sikorska, E.; Romaniuk, A.; Khmelinskii, I. V.; Herance, R.; Bourdelande, J. L.; Sokorski, M.; Koziol, J., Characterization of edible oils using total luminescence spectroscopy. *Journal of Fluorescence* **2004,** *14* (1), 25-35.

38. Deepa, S.; Sarathi, R.; Mishra, A. K., Synchoronous fluorescence and excitation emission characteristic of transformer oil ageing. *Talanta* **2006,** *70*, 811-817.

39. Christensen, J. H.; Hansen, A. B.; Mortensen, J.; Andersen, O., Characterization and matching of oil samples using fluorescence spectroscopy and parallel factor analysis. *Anal. Chem.* **2005,** *77* (7), 2210-2217.

40. Booksh, K. S.; Muroski, A. R., Theory of analytical chemistry. *Anal. Chem.* **1994,** *66* (15), 782A-791A.

41. Wentzell, P. D., Chemometrics: Introduction and applications. Course Notes ed.; Dalhousie University: Halifax, 2010.

42. Mark, H.; Workman, J., *Chemometrics in Spectroscopy*. Elsevier: New York, 2007.

43. Bro, R., Three- and multi-way analysis. Copenhagen University: Copenhagen, 2010.

44. Bro, R., PARAFAC. tutorial and applications. *Chemometrics and Intelligent Laboratory Systems* **1997,** *38*, 22.

45. Andersen, C. M.; Bro, R., Practical aspects of PARAFAC modeling of fluorescence excitation-emission data. *Journal of Chemometrics* **2003,** *17*, 200-215.

46. Gemperline, P., *Practicaa Guide to Chemometrics*. 2nd ed.; CRC Press Taylor & Francis Group: Boca Raton, 2006.

47. Kroonenberg, P. M.; Harshman, R. A.; Murakami, T., Analysing three-way profile data using the PARAFAC and tuker3 models illutrated with views on parenting. *Applied Multivariate Research* **2009,** *13* (1), 5-41.

48. JiJi, R. D.; Andersson, G. G.; Booksh, K. S., Application of PARAFAC for calibration with exitation-emission matrix fluorescence spectra of three classes of enviromental pollutants. *Journal of Chemometrics* **2000,** *14*, 171-185.

49. Booksh, K. S.; Muroski, A. R.; Myrick, M. L., Single-measurement excitation/emission matrix spectrofluorometer for determination of hydrocarbons in ocean water. 2. calibration and quantitation of naphthalene and styrene. *Anal. Chem.* **1996,** *68* (20), 3539-3544.

50. Bro, R.; Kiers, H. A. L., A new efficient method for determing the number of components in PARAFAC models. *Journal of Chemometrics* **2003,** *17*, 274-276.

51. White, J. U., Long optical paths of large aperture. *Journal of the Optical Society of America* **1942,** *32* (5), 285-288.

52. Herriott, D.; Kompfner, R.; H, K., Off-axis paths in spherical mirror interferometers *Applied Optics* **1964,** *3* (4), 523-526.

53. McManus, J. B.; Kebabian, P. L.; Zahniser, W. S., Astigmatic mirror multipass absorption cells for long-path-length spectroscopy. *Applied Optics* **1995,** *34*, 3336-3348.

54. Paldus, B. A.; Kachanov, A. A., An historical overview of cavity-enhanced methods. *Canadian Journal of Physics* **2005,** *83*, 975-999.

55. O'Keefe, A.; A.G.Deacon, D., Cavity ring-down optical spectrometer for absorption measurements using plused laser sources. *Rev. Sci. Instrum.* **1988,** *59*, 11.

56. Waechter, H.; Litman, J.; Cheung, A. H.; Barnes, J. A.; Loock, H.-P., Chemical sensing using fiber cavity ring-down spectroscopy. *Sensors* **2010,** *10*, 1716-1749.

57. Loock, H.-P., *Cavity Ring-Down Spectroscopy: Techniques and Applications*. 1st ed.; Wiley-Blackwell: Hoboken: NJ, USA, 2009.

58. Lerber, T. v.; Sigrist, M. W., Cavity-ring-down principle for fiber-optic resonators: experimental realization of bending loss and evanescent-field sensing. *Applied Optics* **2002,** *41*, 3567-3575.

59. Gupta, M.; Jiao, H.; O'keefe, A., Cavity-enhanced spectroscopy in optical fibers. *Optics Letters* **2002,** *27* (21), 1878-1880.

60. Hallok, A. J.; Berman, E. S. F.; Zare, R. N., Direct monitoring of absorption in solution by cavity ring-down spectroscopy. *Anal. Chem.* **2002,** *74*, 1741-1743.

61. Snyder, K. L.; Zare, R. N., Cavity ring-down spectroscopy as a detector for liquid chromatography. *Analytical Chemistry* **2003,** *75*, 3086-3091.

62. Bechtel, K. L.; Zare, R. N.; Kachanov, A. A.; Sanders, S. S.; Paldus, B. A., Moving beyond traditional UV-Visible absorption detection: cavity ring-down spectroscopy for HPLC. *Anal. Chem.* **2005,** *73*, 5597-5600.

63. Brown, R. S.; Kozin, I.; Tong, Z.; Oleschuk, R. D.; Look, H.-P., Fiber-loop ring-down spectroscopy. *Journal of chemical Physics* **2002,** *117* (23), 10444-10447.

64. Tong, Z.; Jakubinek, M.; Wright, A.; Gillies, A.; Look, H.-P., Fiber-loop ring-down spectroscopy: a sensetive absorption technique for small liquid samples. *Review of Scientific Instrument* **2003,** *74* (11), 4818-4826.

65. ASTM, Standard test method for rust-preventing characteristics of steam turbine oil in the presence of water (horizontal disk method). ASTM International: West Conshohocken, Vol. D3603-07.

66. ASTM, Standard test method for corrosiveness to copper from petroleum products by copper strip test. ASTM International: West Conshohocken, Vol. D130-04e1.

67. ASTM, Standard test method for density, relative density (specific gravity), or API gravity of crude petroleum and liquid petroleum products by hydrometer method. ASTM International: West Conshohocken, Vol. D1298-12b.

68. ASTM, Standard test method for measuring viscosity of new and used engine oils at high shear rate and Hhigh temperature by tapered bearing simulator viscometer at 150 °C. ASTM International: West Conshohocken, Vol. D4683-10

69. ASTM, Standard test method for acid and base number by color-indicator titration. ASTM International: West Conshohocken, Vol. D974-06.

70. ASTM, Standard test method for acid number of petroleum products by potentiometric titration. ASTM International: West Conshohocken, Vol. D664-11a.

71. ASTM, Standard practice for condition monitoring of used lubricants by trend analysis using fourier transform infrared (FT-IR) spectrometry. ASTM International: West Conshohocken, Vol. E2412-04.

72. Stadtmiller, W. H.; Smith, A. N., *Aspects of Lubricant Oxidation*. ASTM International: West Conshohocken, PA, 1986.

73. Lazar, M.; Rychly, J.; Klimo, V.; Pelikan, P.; Valko, L., *Free radicals in chemistry and biology*. CRC Press Inc. Taylor & Francis Group: Boca Raton, Florida, 1989; p 312.

74. Dale E., V. S., Oxidation of 2,4,6-Trimethylheptane. *The Journal of Organic Chemistry* **1972,** *37* (5), 755-760.

75. Denis, J.; Briant, J.; Hipeaux, J.-C., *Lubricant Properties Analysis and Testing*. Second edition ed.; Edition TECHNIP: Paris France, 1997; p 413.

76. Stark, M. S.; Wilkinson, J. J.; Smith, J. R. L.; Alfadhl, A.; Pochopien, B. A., Autoxidation of branched alkanes in the liquid phase. *Ind. Eng. Chem. Res.* **2011,** *50* (2), 817-823.

77. Blaine, S.; Savage, P. E., Reaction pathways in lubricant degradation. 3. reaction model for n -hexadecane autoxidation. *Ind. Eng. Chem. Res.* **1992,** *31* (1), 7.

78. Karis, T. E.; Miller, J. L.; Hunziker, H. E.; Vries, M. S. d.; Hopper, D. A.; Nagaraj, H. S., Oxidation chemistry of a pentaerythritol tetraester oil. *Tribology Transactions* **1999,** *42* (3), 431-442.

79. MacFaul, P. A.; Ingold, K. U.; Lusztyk, J., Kinetic solvent effects on hydrogen atom abstraction from phenol, aniline, and diphenylamine. The importance of hydrogen bonding on their radical-trapping (antioxidant) activities. *J. Org. Chem.* **1996,** *61*, 1316-1321.

80. Zweifel, H.; Maier, R. D.; Schiller, M., *Plastics Additives Handbook*. 6th ed.; Carl Hanser Verlag: Munich, 2009; p 777.

81. Kozlova, E. K.; Kottova, G. G.; Fucks, G. I.; Eminov, E. A., Mechanism of synergistic action of “paired antioxidants”. *Chemistry and Technology of Fuels and Oils* **1982,** *16* (4), 85-87.

82. Pospisil, J.; Nespurek, S., Chain-breaking stabilizers in polymers: the current status. *Polymer Degradation and Stability* **1995,** *49* (1), 11.

83. Wisman, M.; Ah-Sue, A., Monitorin oil degradation using FTIR analysis. *Lubrication Engineering* **1992,** *48* (3), 236-241.

84. ASTM, Standard test method for determination of additive elements, wear metals, and contaminants in used lubricating oils and determination of selected elements in base oils by inductively coupled plasma atomic emission spectrometry (ICP-AES). ASTM International: West Conshohocken, Vol. D5185-09.

85. ASTM, Standard test method for determination of wear metals and contaminants in used lubricating oils or used hydraulic fluids by rotating disc electrode atomic emission spectrometry. ASTM International: West Conshohocken, Vol. D6595-00.

86. Toms, A. M.; Jordan, E.; Humphrey, G. R. In *The success of filter debris analysis for J52 engine condition based maintenance*, The American Institute of Aeronautics and Astronautics (AIAA), Tuscon, AZ, Jul; Proceedings of the 41st AIAA: Tuscon, AZ, 2005.

87. ASTM, Standard test method for the determination of the kinematic viscosity of lubricants by measuring the time for a volume of liquid to flow under gravity through a calibrated glass capillary viscometer. ASTM International: West Conshohocken, Vol. D445-06.

88. ASTM, Standard test method for malculating viscosity index from kinematic viscosity at 40 and 100°C. ASTM International: West Conshohocken, Vol. D2270-10e1.

89. ASTM, Standard test method for low-temperature viscosity of lubricants measured by brookfield viscometer. ASTM International: West Conshohocken, Vol. D2983.

90. ASTM, Standard test method for measuring viscosity of new and used engine oils at high shear rate and high temperature by tapered bearing simulator viscometer at 150 °C. ASTM International: West Conshohocken, Vol. D4683.

91. ASTM, Standard test method for measuring viscosity at high shear rate by tapered bearing simulator viscometer At 100°C. ASTM International: West Conshohocken, Vol. D6616-01a.

92. ASTM, Standard test method for diesel fuel diluent in used diesel engine oils by gas chromatography. ASTM International: West Conshohocken, Vol. D3524.

93. ASTM, Standard test method for trace ethylene glycol in used engine oil by gas chromatography. ASTM International: West Conshohocken, Vol. D4291.

94. ASTM, Standard test method for detecting glycol-base antifreeze in used lubricating oils. ASTM International: West Conshohocken, Vol. D2982.

95. ASTM, Standard test method for determination of water in petroleum products, lubricating oils, and additives by coulometric Karl Fischer titration. ASTM International: West Conshohocken, Vol. D6304.

96. ASTM, Standard test method for measurement of hindered phenolic antioxidant content in non-zinc turbine oils by RULER (voltametric method). ASTM International: West Conshohocken, Vol. D6810.

97. ASTM, Standard test method for measurement of hindered phenolic and aromatic amine antioxidant content in non-zinc turbine oils by linear sweep voltammetry by RULER instrument. ASTM International: West Conshohocken, Vol. D6971.

98. BS EN, Fat and oil derivatives — fatty acid methyl esters (FAME) — determination of oxidation stability (accelerated oxidation test). British Standards Institution West Conshohocken, 2003; Vol. EN 14112.

99. Yang, Z.; Hollebone, B. P.; Wang, Z.; Yang, C.; Landriault, M., Factors affecting oxidation stability of commercially available biodiesel products. *Fuel Processing Technology* **2012,** *106*, 366–375.

100. Ostgaard, K.; Jensen, A., Evaluation of direct fluorescence spectroscopy for monitoring aqueous petroleum solutions. *International Journal of Environmental Analytical Chemistry* **1983,** *14* (1), 55-72.

101. Dudelzak, A. E.; Sergey M. Babichenko; Poryvikna, l. V.; Saar, K. J., Total luminescent spectroscopy for remote laser diagnostics of natural water conditions. *Applied Optics* **1991,** *30* (4), 453-458.

102. Christensen, J. H.; Tomasi, G., Practical aspects of chemometrics for oil spill fingerprinting *Journal of Chromatography A* **2007,** *1169* (1-2), 1-22.

103. Bentz, A. P., Oil spill identification. *Analytical Chemistry* **1976,** *48* (6), 454A-472A.

104. Patra, D., Applications and new developments in fluorescence spectroscopic Techniques for the analysis of polycyclic aromatic hydrocarbons. *Applied Spectroscopy Reviews* **2003,** *38* (2), 155-185.

105. Liu, Y.; He, J.; Song, C.; Li, Y.; Wang, S.; Han, Y.; Wang, H., Oil fingerprinting by three-dimensional (3D) fluorescence spectroscopy and gas chromatography–mass spectrometry (GC–MS). *Environmental Forensics* **2009,** *10*, 324–330.

106. Muroski, A. R.; Booksh, K. S.; Myrick, M. L., Single-measurement excitation/emission matrix spectrofluorometer for determination of hydrocarbons in ocean water. 1. Instrumentation and background correction. *Anal. Chem.* **1996,** *68* (20), 3534-3538.

107. Bugden, J. B. C.; Yeung, C. W.; Kepkay, P. E.; Lee, K., Application of ultraviolet fluorometry and excitation-emission matrix spectroscopy (EEMS) to fingerprint oil and chemically dispersed oil in seawater. *Marine Pollution Bulletin* **2008,** *56* (4), 677-685.

108. JiJi, R. D.; Cooper, G. A.; Booksh, K. S., Excitation-emission matrix fluorescence based determination of carbamate pesticides and polycyclic aromatic hydrocarbons. *Analytical chimica Acta* **1999,** *397*, 61-72.

109. Alostaz, M. d.; Biggar, K.; Donahue, R.; Hall, G., Petroleum contamination characterization and quantification using fluorescence emissionexcitation matrices (EEMs) and parallel factor analysis (PARAFAC). *J. Environ. Eng. Sci.* **2008,** *7*, 183-197.

110. Zhou, Z.; Liu, Z.; Guo, L., Chemical evolution of Mocondo crude oil during laboratory degradation as characterized by fluorescence EEMs and hydrocarbon composition. *Marine Pollution Bulletin* **2013,** *66*, 164-175.

111. Ofunne, G. C.; Maduako, A. U.; Ojinnaks, C. M., Studies on the ageing characteristics of automotive crankcase oils. *Tribology International* **1989,** *22* (6), 401-404.

112. Ofunne, G. C.; Maduako, A. U.; Ojinnaks, C. M., High temperture oxidation stability of automotive crankcase oils and their base oils. *Tribology International* **1990,** *23* (6), 407-412.

113. Livingstone, G. J.; Thompson, B. T.; Okazaki, M. E., Physical, performance and chemical changes in turbine oils from oxidation. *Journal of ASTM International* **2006,** *4* (1), 1-18.

114. Stedmon, C. A.; Bro, R., Charactrization dissolved organic matter fluorescence with parallel factor analysis: a tutorial. *Limnology and Oceanography: Methods* **2008,** *6*, 572-579.

115. Bro, R., Review on multiway analysis in chemistry 2000–2005. *Critical Reviews in Analytical Chemistry* **2006,** *36*, 279-293.

116. Andersson, C. A.; Bro, R., The N-way toolbox for MATLAB. *Chemometrics and Intelligent Laboratory Systems* **2000,** *52*, 1-5.

117. Stedmon, C. A.; Bro, R., Characterizing dissolved organic matter fluorescence with parallel factor analysis: a tutorial. *LIMNOLOGY and OCEANOGRAPHY: METHODS* **2008,** *6*, 572-579.

118. Munzke, D.; Saunders, J.; Omrani, H.; Reich, O., Modeling of fiber-optic fluorescence probes for strongly absorbing samples. *Applied Optics* **2012,** *51* (26), 6343-6351.

119. Guimet, F.; Ferré, J.; Boqué, R.; Rius, F. X., Application of unfold principal component analysis and parallel factor analysis to the exploratory analysis of olive oils by means of excitation–emission matrix fluorescence spectroscopy. *Analytica Chimica Acta* **2004,** *515*, 75-85.

120. Mignani, A. G.; Ciaccheri, L.; D´ıaz-Herrera, N.; Mencaglia, A. A.; Ottevaere, H.; Thienpont, H.; Francalanci, S.; Paccagnini, A.; Pavone, a. F. S., Optical fiber spectroscopy for measuring quality indicators of lubricant oils. *Meas. Sci. Technol.* **2009,** *20*, 1-7.

121. Liu, N.-Y.; He, P.; Dong, S.-L., Binding properties of pheromone-binding protein 1 from the common cutworm Spodoptera litura. *Comparative Biochemistry and Physiology, Part B* **2012,** *161*, 295-302.

122. Ramanujaml, N.; Mitchell, M. F.; Mahadevandansen, A.; Thomsen, S. L.; Staerke, G.; Malpica, A.; Wright, T.; Atkinson, N.; Richards-Kortum, R., Cervical precancer detection using a multivariate statistical algorithm based on laser-induced fluorescence spectra at multiple excitation wavelengths. *Photochemistry and Photobiology* **1996,** *64* (4), 720-735.

123. Mignani, A. G.; Ciaccheri, L.; Cucci, C.; Mencaglia, A. A.; Cimato, A.; Attilio, C.; Ottevaere, H.; Thienpont, H.; Paolesse, R.; Mastroianni, M.; Monti, D.; Gerevini, M.; Buonocore, G.; Nobile, M. A. D.; Mentana, A.; Grimaldi, M. F.; Dall'Asta, C.; Faccini, A.; Galaverna, G.; Dossena, A., Eat-by-Light: fiber-optic and micro-optic devices for food quality and safety assessment. *IEEE Sensors Journal* **2008,** *8* (7), 1342-1354.

124. Brown, S.; Duckinson, C. E.; Douma, M. D.; Zhou, J.; Aston, W. P.; Marcotte, E. P.; Miron, M.; Radcliffe, T.; Gallant, P. J.; Wilton, D., A fibre-optic coupled fluorescence multiwavelength sensor for automated monitoring of bacteria culture from drinking water. In *Applied Industrial Optics: Spectroscopy, Imaging and Metrology*, OSA's Optics InfoBase: Arlington, Virginia United States, 2013.

125. Trujillo, E. V.; Sandison, D. R.; Utzinger, U.; Ramanujam, N.; Follen Mitchell, M.; Richards-Kortum, R., Method to determine tissue fluorescence efficiency in vivo and predict signal-to-noise ratio for spectrometers. *Applied Spectroscopy* **1998,** *52* (7), 943-951.

126. Liang, T. K.; Friedrich, M.; Lala, D.; Ozanyan, K. B., Portable fluorescence sensor for on-line monitoring of lubricant oils. In *IEEE Sensors Conference*, Vienna, AUSTRIA 2004.

127. Buah-Bassuah, P. K.; Bergmann, H. M. v.; Tatchie, E. T.; Steenkamp, C. M., A portable fibre-probe ultraviolet light emitting diode (LED)-induced fluorescence detection system. *Meas. Sci. Technol.* **2008,** *19*, 1-8.

128. Mazzingh, P., A laser diode fluorometer for field measurements of the F685/F730 chlorophyll fluorescence ratio. *IEEE Sensors Journal* **1996,** *67* (10), 3737-3744.

129. Hart, S. J. Light emitting diod (LED) array for excitation emission matrix (EEM) fluorescence spectroscopy. US6691798-B1, February 17, 2006.

130. Hart, S. J.; JiJi, R. D., Light emitting diode (LED) array for excitation emission matrix (EEM) fluorescence spectroscopy. *The Royal Society of Chemistry* **2002,** *127*, 1693-1699.

131. Kim, Y.-C.; Jordan, J. A.; Chávez, D.; Booksh, K. S., Coaxial fiber-optic chemical-sensing excitation–emission matrix fluorometer. *Optics Letters* **2011,** *36* (3), 355-357.

132. Ma, J.; Chiniforooshan, Y.; Hao, W.; Bock, W. J.; Wang, Z. Y., Easily fabricated, robust fiber-optic probe for weak fluorescence detection: modeling and initial experimental evaluation. *Optics Express* **2012,** *20* (4), 4805-4811.

133. Plaza, P.; Dao, N. Q.; Jouan, M.; Fevrier, H.; Saisse, H., Simulation and optimization of adjacent optical fiber sensors. *Applied Optics* **1986,** *25*, 3448-3454.

134. Blanco, A.; Chomski, E.; Grabtchak, S.; Ibisate, M.; John, S.; Leonard, S. W.; Lopez, C.; Meseguer, F.; Miguez, H.; Mondia, J. P.; Ozin, G. A.; Toader, O.; Driel, H. M. v., Large-scale synthesis of a silicon photonic crystal with a complete three-dimensional bandgap near 1.5 micrometres. *Nature* **2000,** *405*, 437-440.

135. Wang, L.; Choi, H. Y.; Jung, Y.; Lee, B. H.; Kim, K.-T., Optical probe based on double-clad optical fiber for fluorescence spectroscopy. *Optics Express* **2007,** *15* (26), 17681-17689.

136. Bhowmick, G. K.; Gautam, N.; Gantayet, L. M., Design optimization of fiber optic probes for remote fluorescence spectroscopy. *Optics Communications* **2009,** *282*, 2676-2684.

137. Kulatilaka, W. D.; Hsu, P. S.; Gord, J. R.; Roy, S., Point and planar ultraviolet excitation/detection of hydroxyl-radical laser-induced fluorescence through long optical fibers. *Optics Letters* **2011,** *36* (10), 1818-1820.

138. He, G.; Cuomo, F. W., A light intensity function suitable for multimode fiber-optic sensors. *Journal of Lightwave Technology* **1991,** *9* (4), 545-551.

139. Dixon, J. M.; Taniguchi, M.; Lindsey, J. S., PhotochemCAD 2: A refined program with accompanying spectral databases for photochemical calculations. *Photochemistry and Photobiology* **2005,** *81*, 212-213.

140. Du, H.; Fuh, R. C. A.; Li, J.; Corkan, L. A.; Lindsey, J. S., PhotochemCAD: A computer-aided design and research tool in photochemistry. *Photochemistry and Photobiology* **1998,** *68* (2), 141-142.

141. Ozanyan, K. B.; Yeo, T. L.; Hindle, F. P.; Poolton, N. R. J.; McCann, H.; Tan, K. L., Fiber-based UV laser-diode fluorescence sensor for commercial gasolines. *IEEE Sensors Journal* **2004,** *4*, 681-690.

142. Cooney, T. F.; Skinner, H. T.; Angel, S. M., Comparative study of some fiber-optic remote Raman probe designs. Part I: model for liquids and transparent solids. *Applied Spectroscopy* **1996,** *50*, 836-848.

143. Cooney, T. F.; Skinner, H. T.; Angel, S. M., Comparative study of some fiber-optic remote Raman probe designs. Part II: tests of single-fiber, lensed, and flat- and bevel-tip multifiber probes. *Applied Spectroscopy* **1996,** *50*, 849-860.

144. ASTM, Standard specification for aviation turbine fuels. ASTM International: West Conshohocken, Vol. D1655-13.

145. ASTM, Standard test method for density, relative density, and API gravity of liquids by digital density meter. ASTM International: West Conshohocken, Vol. D4052.

146. ASTM, Standard test method for distillation of petroleum products at atmospheric pressure. ASTM International: West Conshohocken, Vol. D86-12.

147. ASTM, Standard test methods for flash point by small scale closed cup tester. ASTM International: West Conshohocken, Vol. D3828-12a.

148. ASTM, Standard test method for freezing point of aviation fuels. ASTM International: West Conshohocken, Vol. D2386-06.

149. ASTM, Standard test method for gum content in fuels by jet evaporation. ASTM International: West Conshohocken, Vol. D381-12.

150. Currie, L. A.; Svehla, G., Direct monitoring of absorption in solution by cavity ring-down spectroscopy. *Pure & Appl. Chem.* **1994,** *66* (3), 595-608.

151. Loock, H.-P.; Wentzell, P. D., Detection limits of chemical sensors: Applications and misapplications. *Sensors and Actuators B* **2012,** *173*, 157-163.

152. ASTM, Test method for determination of the fatty acid methyl esters content of aviation turbine fuel using flow analysis by fourier transform infrared spectroscopy – rapid screening method. ASTM International: Vol. D7797-12

153. Suggett, D. J.; Prasil, O.; Borowitzka, M. A., *Chlorophyll a fluorescence in aquatic sciences: Methods and applications*. Springer Science + Business Media: 2011.